Faculty of Aerospace Engineering

Monocular Optical Flow based Attitude Estimation in Micro Aerial Vehicles

A Bio-Inspired Approach

Abhishek Chatterjee

August 16, 2019

TU Delft Delft University of Technology

Challenge the future

Monocular Optical Flow based Attitude Estimation in Micro Aerial Vehicles

A Bio-Inspired Approach

Master of Science Thesis

For obtaining the degree of Master of Science in Aerospace Engineering
at Delft University of Technology

Abhishek Chatterjee

August 16, 2019

Faculty of Aerospace Engineering · Delft University of Technology

Delft University of Technology

Delft University of Technology
Faculty of Aerospace Engineering
Department of Control and Simulation

The undersigned hereby certify that they have read and recommend to the Faculty of Aerospace Engineering for acceptance of a thesis titled **"Monocular Optical Flow based Attitude Estimation in Micro Aerial Vehicles"** by **Abhishek Chatterjee** in partial fullfillment of the requirements for the degree of **Master of Science**.

Dated: August 30, 2019

Readers:

Dr. Ir. G. C. H. E. de Croon

Dr. Ir. J. F. L. Goosen

Ir. C. de Wagter

M.Sc. D. A. Olejnik

Acknowledgements

Pursuing Master of Science in Aerospace Engineering at TU Delft has been an incredible journey that is finally coming to an end with the conclusion of my thesis. I would like to express my gratitude to everyone who has accompanied me in this wonderful adventure.

First and foremost, I would like to thank my supervisors Guido de Croon and Diana Olejnik for their guidance and support throughout the course of this thesis. Guido, working with you has been a very exciting and enriching experience. Thank you for providing me with the opportunity of working on this project and helping me produce a thesis that I am proud of. Diana, you have not just been a supervisor but also an amazing friend. I am grateful for all the support and encouragement that you have provided me over the past years.

I would like to offer my sincere appreciation to Matěj Karásek, Christophe de Wagter and all the members of MAVLab for their valuable assistance and advice during various parts of the project.

I feel blessed to have such great friends in my life who have always believed in me and inspired me to keep working towards my goals. A word of appreciation goes out to them.

Finally, I would like to thank the most important people in my life, my mother Swapna, my father Devdas and my brother Animesh, for their love and blessings. With the reader's permission, I would like to dedicate the following lines to them in Bengali.

> মা, বাবা, ভাই, তোমাদের ভালোবাসা আর আশীর্বাদ এর জননই আজ এই প্রজেক্ট পুরো করতে পেরেছি | আমার এই কাজ তোমাদের অর্পণ করলাম |

I hope the reader will enjoy reading my thesis as much as I have enjoyed working on it.

Abhishek Chatterjee
Delft, 16 August 2019

Abstract

The exceptional flight capabilities of insects have long amazed and inspired researchers and roboticists striving to make Micro Aerial Vehicles (MAVs) smaller and more agile. It is well known that optical flow plays a prominent role in insect flight control and navigation, and hence it is being increasingly investigated for applications in flying robots as well. However, optical flow based strategies for estimation and stabilization of orientation remain obscure in literature. In this report, we introduce a novel state estimation algorithm based on optical flow measurements and the knowledge of efference copies. The proposed technique estimates the following states of a flying robot (constrained to move with three degrees of freedom): roll angle, rate of change of roll angle, horizontal and vertical components of velocity and height. The estimator only utilizes the knowledge of control inputs and optical flow measurements obtained from a downward looking monocular camera. Through non-linear observability analysis, we theoretically prove the feasibility of estimating the attitude of a MAV using ventral flow and divergence measurements. Based on the findings of the observability analysis, an extended Kalman filter state estimator is designed and its performance is verified in simulations. To test the applicability of the estimator in flight control and stabilization, we used the filter to implement a closed loop attitude and altitude controller in simulation. The performance of the controller shows that despite the limited frame rate, of most available cameras, the state estimates computed by the estimator can be used to stabilize and control the flight of an inherently unstable MAV. We conclude the article by verifying the performance of the estimator on flight data recorded on a real flying robot. To the best of our knowledge, the introduced strategy is the first attitude estimation technique that utilizes monocular optical flow as the only sensory information.

Besides the investigation on optical flow based attitude estimation technique, this thesis presents a comprehensive literature survey on the main topics relevant to the work.

Contents

List of Figures

List of Tables

List of Symbols

Greek Symbols

α, β	Gradients of observed surface
δ	Sensor bias
ζ	Damping ratio of spring mass system
κ	Condition number
κ_i	Thrust coefficient of the ith rotor of a MAV
$\boldsymbol{\nu}$	Measurement noise vector
σ	Standard deviation of a series
$\sigma_{min}, \sigma_{max}$	Minimum and maximum singular values of a matrix
$\sum$	Non linear system
τ	Time duration of a manoeuvre
ϕ, θ, ψ	Euler angles representing MAV's/observer's attitude
ω	Angular velocity
ω_{ie}	Earth's angular velocity
ω_s	Oscillation frequency
ω_{sn}	Natural frequency of spring mass system
$\hat{\omega}_x, \hat{\omega}_y$	Ventral flow components
$\hat{\omega}_z$	Half flow divergence: relative vertical velocity
Ω	MAV rotor speed

Roman Symbols

a	Acceleration
A, B, C	Observer's rotational velocity components
$\boldsymbol{A}$	System process matrix
$\boldsymbol{B}$	System input matrix
c	Spring damping constant for accelerometer model
$\hat{d}$	Flow divergence
DO	Degree of observability
e	Sensor noise
f^b	Specific force in body frame
$\boldsymbol{f}$	System state derivative vector function
g	Acceleration due to gravity
$\boldsymbol{h}$	System observation vector function
$\boldsymbol{H}$	System observation matrix
I	Image intensity function
$I_{x_\mathcal{B}}, I_{y_\mathcal{B}}, I_{z_\mathcal{B}}$	Moments of inertia about MAV's body axes
k	Spring constant in accelerometer model
$\mathcal{L}$	Lie derivative operator
m	Magnetic field
$M_{x_\mathcal{B}}, M_{y_\mathcal{B}}, M_{z_\mathcal{B}}$	Moments about MAV's body axes
$\mathbb{N}$	Set of all natural numbers
$\mathcal{O}$	Observability matrix

p, q, r	MAV's angular velocity components: roll rate, pitch rate and yaw rate
$\hat{\boldsymbol{p}}$	Image pixel coordinate vector in spherical camera model
$\hat{\boldsymbol{p}}_{\boldsymbol{u}}$, $\hat{\boldsymbol{p}}_{\boldsymbol{u}}$	Parameters of linear optical flow model
$\boldsymbol{P}$	Observed world point's position in Spherical coordinate system
r_s	Relative displacement between vehicle and accelerometer proof mass
R_s	Steady state relative displacement amplitude
$\mathbb{R}$	Set of all real numbers
t	Time
T	Thrust
u, v, w	MAV's translational velocity components
$\hat{u}$, $\hat{v}$	Optical flow components
$\hat{u}^R$, $\hat{v}^R$	Rotational optical flow components
$\hat{u}^T$, $\hat{v}^T$	Translational optical flow components
U, V, W	Observer's translational velocity components
$\boldsymbol{w}$	Process noise
$\hat{x}$, $\hat{y}$	Pixel coordinates on a pixel array
x_s	Accelerometer proof mass displacement
$\boldsymbol{x}$	State vector
$\hat{\boldsymbol{x}}$	State estimate
X, Y, Z	Metric position components in Cartesian coordinates
y_s	Vehicle Displacement
$\boldsymbol{y}$, $\boldsymbol{z}$	Measurement Vector
Y_s	Oscillation amplitude of accelerometer proof mass

Subscripts

$\mathcal{B}$, b	Body reference frame
$\mathcal{I}$, i	Inertial reference frame
n	Navigation reference frame

List of Acronyms

ARMSE	Average Root Mean Square Error
CoG	Centre of Gravity
CoP	Centre of Pressure
CURVACE	Curved Artificial Compound Eye
DoF	Degrees of Freedom
DLR	Dorsal Light Response
DVS	Dynamic Vision Sensor
EKF	Extended Kalman Filter
EMD	Elementary Motion Detector
FAST	Features from Accelerated Segment Test
FoV	Field of View
FWMAV	Flapping Wing Micro Aerial Vehicle
GPS	Global Positioning System
HKF	Hybrid Kalman Filter
IEKF	Iterated Extended Kalman Filter
IMU	Inertial Measurement Unit
KF	Kalman Filter
LORA	Lateral Optic Flow Regulation Autopilot
MAV	Micro Aerial Vehicle
MEMS	Micro Electro Mechanical System
OCTAVE	Optical Flow based Control System for Aerial Vehicles
RMSE	Root Mean Square Error
SSD	Sum of Squared Differences
TODFC	Translational Optic Flow Direction Constraint
UAV	Unmanned Aerial Vehicle
UKF	Unscented Kalman Filter
VTOL	Vertical Take-off and Landing

1

Introduction

Millions of years of evolution have shaped the nature around us to demonstrate amazing variety, adaptability and sophistication. Ever since the beginning, nature has been the prime inspiration that has shaped human innovation. Velcro [1], honeycomb composite structures [2] and biocomputing [3] are just a few examples of the thousands of technological feats that we humans have achieved by deriving ideas from the nature. Though for the author, who is an Aerospace Engineering student, perhaps the most relevant examples of bio-mimicry are the aerial vehicles.

The extraordinary aerial feats of the natural flyers has inspired humankind's timeless fascination with the ability to fly. Some of the early attempts at engineering flying machines focused on mimicking the flapping wings that the insects and birds demonstrate [4, 5]. However, these attempts were unsuccessful and often resulted in fatal crashes. It was only in the early nineteen hundreds that humans achieved successful flight in a powered heavier-than-air aircraft [6]. Consequently the twentieth century witnessed immense advances in the field of aviation. Mankind, now, has finally gained the wings it had always aspired for. Although, despite the years of fascination with flapping wing flight, the modern aircraft are fixed wing, rotary wing or lighter-than-air blimps. It is the recent surge in the popularity of the Unmanned Aerial Vehicles (UAVs) and the conquest of their miniaturization into Micro Aerial Vehicles (MAVs), that has brought back the bio-inspired flapping wing flight into research spotlight.

As a result of small size and low flight speeds (similar to insects), MAVs encounter low Reynolds number flow conditions which is the regime where flapping wing flight is more efficient than the rotary wing or fixed wing flight [7]. In the recent years, several flight capable Flapping Wing Micro Aerial Vehicles (FWMAVs) have been developed, like the Robobee [8], Nano Hummingbird [9], and DelFly [10, 11]. Some of these FWMAVs have tails that provide passive stability to these platforms. While the others, more closely resembling insects, are tailless and hence inherently unstable. Despite the passive stability, the tailed FWMAVs as well are no longer stable near hover, since the airflow component due to forward velocity of the vehicle is absent [12]. Consequently, most FWMAVs require active attitude stabilization to maintain flight stability.

Attitude stabilization of any platform requires accurate attitude estimation, which is achieved by ego-motion sensors and state estimation algorithms. Most MAVs (and FWMAVs) depend on the Inertial Measurement Units (IMUs), comprising of accelerometers, gyroscopes and sometimes magnetometers, for attitude estimation. Micro Electro Mechanical System (MEMS) IMUs are the most widely used on-board ego-motion sensing devices in MAVs, owing to their small size and light weight. However, as the size of these MEMS sensors reduces, their sensitivity decreases and noise increases. Integrating the signals from these sensors to estimate orientation, velocity or position of the robot results in a quickly diverging solution. As a result, these IMUs require the integration of

augmentation sensors, like Global Positioning System (GPS), to correct for these diverging estimates [13]. The fact that most MAVs find applications in GPS-denied environments, demands the integration of other navigation sensors. This is where nature, once again, can come to the mankind's rescue.

Flying insects can, by far, out manoeuvre any human made flying machine while negotiating cluttered indoor environments. Drawing inspirations from the ego-motion sensing and control strategies used by the insects can help the researchers to significantly improve MAV stabilization and navigation approaches. Insects use rich sensory feedback for flight stabilization and control, drawing ego-motion information from sensory organs like halteres, ocelli and compound eyes [14]. Visual sensing plays a prominent role in the insect's ego-motion inference. Most insects possess a sophisticated imaging system known as the compound eyes. Apart from enabling panoramic imagery, the visual information from the compound eyes also provides the insects, a sense of motion and direction, in the form of optical flow fields [7]. While moving through a stationary environment, insects experience apparent motion of the surrounding objects in the form of retinal image shifts, formally known as optical flow [15]. Optical flow measures the ratio of movement of the observer to the distance of surrounding objects in the environment [16, 17]. Though this coupled relationship, between velocity and distance, makes the estimation of absolute values of the states challenging, analysing the optical flow fields allows the insects to assess their motion and use this information for navigation and flight control. Optical flow information has been found to be critical to various insect flight behaviours like obstacle avoidance [18], flight speed regulation [19, 20], altitude control [21], and performing smooth landings [22].

Drawing inspirations from insects, optical flow has been used for navigation and control of MAVs. Researchers have investigated the applications of optical flow based navigation strategies for landing [23–25], obstacle avoidance [23, 26] and velocity control [27, 28] of MAVs. However, orientation perception strategies used by the insects are yet to be properly understood [29]. Consequently, optical flow based attitude estimation and stabilization strategies for MAVs remain largely unexplored.

1.1. Research Motivation and Objective

The sensory organs involved in attitude stabilization of insects can be categorized as: inertial mechanosensors like the halteres, antennae, tactile hair and gravity sensitive pendulous hair on the cerci, and visual sensors like the ocelli and compound eyes [7]. There are evidences that indicate that vision plays a more prominent role than inertial sensing, in flight stabilization and control of many insects. This can be attributed to the fact that the forces perceived by any inertial sensor are proportional to the size of the proof mass whose inertia reacts to the applied accelerations. Size of the proof mass becomes a limiting factor in creatures as small as the insects. Barring a few exceptions, like the dragonflies, most insects have not been found to possess organs sensitive to accelerations [14]. Dipteran insects, like house flies, have inertial motion sensing organs called halteres that are known to sense rotational rates [30]. However, halteres are not found in many insects like the honeybees [22]. Some insects, like cockroaches, are equipped with gravity sensitive organs, but many other insects lack any such organs [14]. Unlike the inconsistent presence of inertial motion sensing organs in insects, visual sensors, like ocelli and compound eyes, are ubiquitously found in almost all insects [7]. Goulard et al. [29] reported that crash avoidance behaviour in hoverflies, subjected to free fall, depends mainly on vision rather than gravity perception or inertial sensing. These findings establish the hypothesis that insects might mainly depend upon vision (and hence optical flow) for ego-motion estimation and flight stabilization. However, the techniques used by the insects to estimate their orientation using optical flow remain obscure in literature.

Regarding applications to MAV attitude estimation and stabilization, researchers have attempted to use optical flow to complement inertial sensors in estimating MAV orientation [31, 32]. Some

researchers have also studied reactive visuo-motor control schemes, where the perceived optical flow is directly used in a feedback loop, without estimating the absolute values of the MAV's states [33, 34]. Even though the visuo-motor control strategies are backed by some behavioural studies on insect flight [22], there are evidences suggesting that the insects can estimate the absolute values of their states. For instance, fruit flies extend their legs at a specific distance from the landing surface and thus might be capable of estimating their distance from the surface [35]. Goulard et al. [36] modelled the crash avoidance dynamics of insects and concluded that a closed loop pitch control system based only on optical flow does not suffice to maintain a stable flight. To achieve stability, the authors augmented the model with a closed loop pitch rate controller based on absolute pitch angle estimates, suggesting that estimation of absolute orientation might be necessary for the insects to stabilize their flight.

It has been shown in literature that it is indeed possible to estimate absolute distances and velocities, utilizing optical flow measurements, if a robot has access to its control inputs (efference copies) [35, 37, 38]. However, to the best knowledge of the author, feasibility of estimating MAV attitude using optical flow measurements as the only sensory information has not been proven in literature yet. Motivated by the described deficiency in literature, this thesis intends to pursue the following main research objective.

Feasibility investigation and development of an optical flow based approach for attitude estimation of a flying robot.

The attitude estimation approach being researched is motivated by its potential application in attitude stabilization of inherently unstable MAV platforms. Thus, the research presented is also intended to answer the following question:

- **How feasible is the use of the developed optical flow based attitude estimation approach in flight stabilization of inherently unstable MAV platforms?**

Further, the applicability of optical flow based methods is highly dependent on the characteristics of the optical sensor used [39]. Therefore, the answer to the above sub-question would also depend on the assumption of specific sensor characteristics, which leads to the following sub question:

- **What should be the favourable characteristics of an optical flow sensor, like temporal resolution and noise, to be effectively used for attitude estimation and stabilization of a flying robot ?**

1.2. Report Structure

The main contributions of this thesis and the work carried out to answer the research questions are presented in the scientific article in Part **I** of the report. The presented paper can be read as a standalone document and is structured as follows: The article starts with a concise introduction to the relevant concepts and previous contributions in literature. In the second part, non-linear observability analysis has been utilized to analytically prove the feasibility of using an optical flow based approach for attitude estimation in a flying robot. In the third part, based on the findings of the observability analysis, an attitude estimation algorithm has been developed and its performance has been verified in simulation. And in the fourth part of the article, results obtained by testing the developed attitude estimator on flight data of a real flying robot have been presented. At the end, the article has been supplemented with appendices that describe the mathematical derivations of observability analysis for various scenarios considered in the study.

Part **II** of the report is intended to present a detailed review of the literature relevant to the topic of optical flow based attitude estimation in MAVs. In Chapter 2, inertial sensors and the conventional techniques used for attitude estimation in MAVs are discussed and the limitations of these approaches have been highlighted. In Chapter 3, motion perception and navigation strategies in insects have been reviewed. This chapter highlights the importance of optical flow in insect flight navigation and draws inspirations for flight stabilization and control of MAVs. Chapter 4 presents an in-depth discussion of optical flow, its mathematical formulation and the commonly used optical flow estimation techniques. Further, the chapter discusses various optical flow sensors that have been used in literature and reviews various optical flow based MAV navigation approaches available in the literature. Chapter 5 is devoted to FWMAVs and discusses various state of the art FWMAVs. Further the chapter introduces the DelFly Nimble, which in future studies will be used as a platform for application of the approach developed in this study. Finally, Chapter 6 concludes the survey by summarizing the findings of the literature study.

Part I
SCIENTIFIC ARTICLE

Monocular Optical Flow based Attitude Estimation in Micro Aerial Vehicles

A. Chatterjee*‡, D.A. Olejnik†‡, G.C.H.E. de Croon†‡
*M.Sc. student, †Supervisor
‡Control & Simulation, Control & Operations Department
Faculty of Aerospace Engineering, Delft University of Technology

***Abstract*—The exceptional flight capabilities of insects have long amazed and inspired researchers and roboticists striving to make micro aerial vehicles (MAVs) smaller and more agile. It is known that optical flow plays a prominent role in insect flight control and navigation, and hence it is being increasingly investigated for applications in flying robots as well. However, optical flow based strategies for estimation and stabilization of orientation remain obscure in literature. In this article, we propose a novel state estimation algorithm based on optical flow measurements and the knowledge of efference copies. The proposed technique estimates the following states of a MAV (constrained to move with three degrees of freedom): roll angle, rate of change of roll angle, horizontal and vertical components of velocity and height. The estimator only utilizes the knowledge of control inputs and optical flow measurements obtained from a downward looking monocular camera. Through non-linear observability analysis, we theoretically prove the feasibility of estimating the attitude of a flying robot using ventral flow and divergence measurements. Based on the findings of the observability analysis, an extended Kalman filter state estimator is designed and its performance is verified in simulations. To test the applicability of the estimator in flight control and stabilization, we simulated a closed loop controller to command the attitude and height of an aerial vehicle. The performance of the controller shows that despite the limited frame rate, of most available cameras, the state estimates computed by the estimator can be used to stabilize and control the flight of an inherently unstable MAV. We conclude the article by demonstrating the performance of the estimator on flight data recorded on a real flying robot. To the best of our knowledge, the introduced strategy is the first attitude estimation technique that utilizes monocular optical flow as the only sensory information.**

***Index Terms*—Bio-inspiration, insect flight, optical flow, attitude estimation, Micro Aerial Vehicles**

I. Introduction

THE recent surge in the popularity of Micro Aerial Vehicles (MAVs) has brought about an increasing interest of the research community in making these aerial robots smaller and more agile. Decreasing sizes and increasing manoeuvrability often translates into the development of inherently unstable MAVs, like the tailless Flapping Wing MAV (FWMAV), DelFly Nimble [1]. Due to the lack of inherent stability, these MAVs require active ego-motion estimation and flight stabilization. Micro Electro Mechanical System Inertial Measurements Units (MEMS IMUs) are the most widely used on-board ego-motion sensing devices in MAVs, owing to their small size and light weight. However, as the size of these sensors decreases, their noise increases and sensitivity diminishes. This necessitates the incorporation of complimentary sensors and more robust state estimation techniques [2]. By contrast, some insects are believed to lack sensory organs that perceive inertial forces and rates, and yet their exceptional flight capabilities have long amazed and inspired roboticists.

Insects use rich sensory feedback for flight stabilization and control, drawing ego-motion information from various sensory organs: inertial mechanosensors that sense inertial forces and rotational rates like halteres, antennae and hair, and visual sensors such as ocelli and compound eyes [3]. However, in some insects, like honey-bees and other flying hymenopterans, inertial mechanosensory organs have not been identified yet [4]. As such, vision is believed to play a prominent role in flight stabilization and control of these natural flyers [5]. Insects derive a sense of motion and direction from the visual information captured by the compound eyes in the form of optical flow fields [3][5]. Optical flow has been found to be critical to various flight behaviours such as obstacle avoidance [6], flight speed regulation [7][8][9], altitude control [10][11] and landing [12][13]. However, the strategies used by insects to estimate and stabilize their orientation are yet to be completely understood [3]. Goulard *et al.*[14] studied how insects cope with weightlessness and stabilize their flight by subjecting hoverflies to free-fall. The authors concluded that for crash avoidance and flight stabilization, the insects utilize a multisensory control system depending mainly on vision rather than gravity perception or inertial sensing. These studies, establishing the importance of visual sensing in flight stabilization and control, coupled with the apparent lack of inertial sensing in some insects, indicate that insects might be capable of deriving information about their orientation using only the perceived optical flow fields.

Optical flow conveys information about the ratio of an observer's velocity to distance from the observed world point [15], but neither of those parameters independently. To disentangle these quantities and estimate the absolute values of the observer's states, additional information is necessary. This 'scaling' of the optical flow measurements, can be performed by additional sensor packages like accelerometers, airspeed sensors, sonar or stereo camera setup [16][17][18]. Inspired by the absence of scaling sensors in some insects, several researchers have studied approaches of using optical flow directly in a control loop without estimating the absolute values of the MAV's states. These visuo-motor control strategies have been designed to perform various flight tasks such as landing [19], obstacle avoidance [20], velocity control [21], terrain

following [22] and stabilization [23] in MAVs.

Even though the visuo-motor control strategies are backed by some behavioural studies on insect flight [4], there are evidences suggesting that insects can estimate the absolute values of their states, including the static states such as distances and attitude angles. For instance, fruit flies extend their legs at a specific distance from the landing surface and thus must be capable of estimating the distance [24]. Based on their observations about the behaviour of hoverflies subjected to free fall [14], Goulard *et al*.[25] modelled the crash avoidance dynamics of the insects and concluded that a closed loop pitch control system based only on optical flow regulation does not suffice to maintain a stable flight. To achieve stability, the authors augmented the model with a closed loop pitch rate controller based on absolute pitch angle estimates, indicating that estimation of absolute orientation might be necessary for the insects to stabilize their flight.

It has been shown that it is indeed possible to estimate absolute distances from optical flow measurements, if a robot has access to its control inputs (also referred to as 'efference copies'). Several strategies for the same have been proposed in literature. van Breugel *et al*.[24] showed that during a constant divergence landing manoeuvre, the distance remains proportional to the control input (thrust) and follows an exponentially decreasing function over time. Thus, thrust values can be used to estimate distances during the manoeuvre. In [26], de Croon proposed a distance estimation approach based on the detection of self induced oscillations during fixed gain constant divergence control. The author proved that there exists a proportional relationship between the controller gain and the height at which the instability occurs. Therefore, by detecting the oscillations, the robot's height can be estimated. The strategy has been leveraged in [27] to perform smooth landings of a MAV by adapting the control gains during landing. Ho *et al*.[28] presented a distance and velocity estimation algorithm that utilizes efference copies in combination with the flow divergence measurements. The efference copies are used to predict changes in a MAV's states and these predictions are corrected through the observed flow divergences. Optical flow measurements, however, are also affected by the orientation of the robot and hence must also encode information about attitude. But, to the best of our knowledge, the feasibility of estimating attitude using only optical flow measurements has not been proven in literature yet. In this study we show that, following an approach similar to [28], the orientation of a MAV can be derived in addition to its height and velocities.

The main contribution of this article is the proposition of a novel attitude estimation algorithm based on optical flow measurements and the knowledge of efference copies. The proposed technique estimates various MAV states: attitude, rate of change of attitude, horizontal and vertical components of velocity and height; utilizing only the knowledge of control inputs and optical flow measurements obtained from a downward looking monocular camera. The performance of the estimator has been verified in simulations and on flight data obtained from a real flying robot.

The paper has been structured as follows. In section II, we utilize non-linear observability analysis [29] to prove that it is possible to estimate the attitude of a MAV, among other states, using optical flow observables. In section III, based on the findings of the observability analysis, an extended Kalman filter state estimator has been designed and the performance of the filter has been verified through simulations. Finally in section IV, the performance of the estimator has been validated through flight data recorded on a Parrot Bebop quadcopter.

II. Attitude Observability using Optical Flow Measurements

Since we intend to design a purely optical-flow based attitude estimator, the first step is to derive a system model in which the states, including attitude, are observable using optical flow measurements. Here, observability means that any distinct states are distinguishable by observing the output trajectories of the system on application of a bounded measurable input. In this section, we use the non-linear observability analysis [29] to analyse various system models and formulate a model in which the states are observable using optical flow measurements and the knowledge of efference copies/control inputs.

A. Mathematical Formulation of Optical Flow

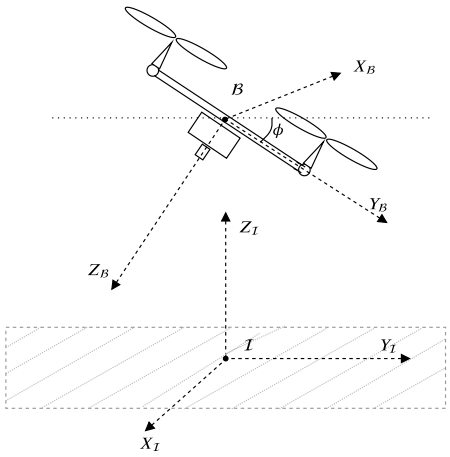

Fig. 1: MAV equipped with a downward looking camera, moving through a stationary environment. Representation of various reference frames considered in this study. $\mathcal{B}$: body reference frame, $\mathcal{I}$: inertial reference frame

In this study, the Longuet-Higgins and Prazdny mathematical model of optical flow [15] has been employed. The model relates ego-motion of an observer (camera) moving through a stationary environment to the perceived optical flow. Consider the scenario described in figure 1, where a quadcopter equipped with a downward looking camera, arbitrarily moves over a planar surface. $\mathcal{B}$ denotes the body reference frame of the quadcopter, centred at point $\mathcal{B}$ where the camera's aperture is also defined. It is also assumed that $\mathcal{B}$ converges with the MAV's centre of gravity (CoG). Now, let $X_\mathcal{B}Y_\mathcal{B}Z_\mathcal{B}$ be a right

handed Cartesian coordinate system, centred and fixed at $\mathcal{B}$, with the $Z_{\mathcal{B}}$-axis aligned along the camera's optical axis. The inertial frame of reference is denoted by $\mathcal{I}$. The quadcopter is moving with transnational velocities $u_{\mathcal{B}}$, $v_{\mathcal{B}}$, and $w_{\mathcal{B}}$, and rotational velocities p, q and r, defined in $\mathcal{B}$. To relate the quadcopter's motion to optical flow, the model utilizes the pinhole camera projection method [15]. In this formulation, world points $(x_{\mathcal{B}}, y_{\mathcal{B}}, z_{\mathcal{B}})$ in the camera's field of view are projected onto the image pixel coordinates $(\hat{x}, \hat{y})$ on the camera's image plane. Due to relative motion between the quadcopter and the environment, these projections undergo a translational motion, i.e. the optical flow, whose components, $\hat{u}$ and $\hat{v}$ in pixels per second, are obtained as described by equations 1a and 1b.

$$\hat{u} = -\frac{u_{\mathcal{B}}}{z_{\mathcal{B}}} - q + r\hat{y} - \hat{x}(-\frac{w_{\mathcal{B}}}{z_{\mathcal{B}}} - p\hat{y} + q\hat{x}) \tag{1a}$$

$$\hat{v} = -\frac{v_{\mathcal{B}}}{z_{\mathcal{B}}} + p - r\hat{x} - \hat{y}(-\frac{w_{\mathcal{B}}}{z_{\mathcal{B}}} - p\hat{y} + q\hat{x}) \tag{1b}$$

Once the relationship between the MAV's states and the optical flow components has been established, the next step is to use this knowledge to retrieve information about the MAV's motion and the environment structure. This information is contained in visual observables that can be derived from equation 1.

Commonly used visual observables, in the literature concerning optical flow based navigation, are ventral flows ($\hat{\omega}_x = -u_{\mathcal{B}}/z_{\mathcal{B}_0}$, $\hat{\omega}_y = -v_{\mathcal{B}}/z_{\mathcal{B}_0}$) that encode the information about MAV's horizontal motion and divergence ($\hat{d} = 2w_{\mathcal{B}}/z_{\mathcal{B}_0}$) that encodes information about MAV's vertical motion. The ventral flows can be described as the 'de-rotated' optical flow components observed at the origin of the image plane ($(\hat{x}, \hat{y}) = (0, 0)$, the point where the optical axis intersects the image plane). Accordingly, $z_{\mathcal{B}_0}$ represents the $Z_{\mathcal{B}}$ coordinate of the world point where the optical axis intersects the observed plane. De-rotation refers to the procedure of eliminating the effects of observer's rotations, from the flow vectors, using angular rate measurements from external sensors (eg. gyroscopes). However, since we intend to estimate the MAV motion states using optical flow as the only sensory information, we use ventral flow components without de-rotation, described by equations 2a and 2b, as key observables. Further, we also use half divergence or relative vertical velocity $\hat{\omega}_z$, described by equation 2c, as another observation. Henceforth in this article, unless stated otherwise, the term ventral flows will be used to refer to flows that have not been de-rotated and the term divergence will be used to refer to relative vertical velocity $\hat{\omega}_z$.

$$\hat{\omega}_x = -\frac{u_{\mathcal{B}}}{z_{\mathcal{B}_0}} - q \tag{2a}$$

$$\hat{\omega}_y = -\frac{v_{\mathcal{B}}}{z_{\mathcal{B}_0}} + p \tag{2b}$$

$$\hat{\omega}_z = \frac{\hat{d}}{2} = \frac{w_{\mathcal{B}}}{z_{\mathcal{B}_0}} \tag{2c}$$

B. Non-Linear Observability Analysis Preliminaries

A non-linear system is deemed observable if the mapping from initial condition to output trajectory is one to one. A standard tool to check the (local-weak) observability of a non-linear system is the observability rank condition, introduced by Herman and Krener [29]. In this sub-section, we briefly introduce the observability test using the notation style adopted in this paper.

Consider the non-linear system $\sum$, described by equation 3.

$$\dot{\boldsymbol{x}}(t) = \boldsymbol{f}(\boldsymbol{x}, \boldsymbol{u}, t) \tag{3a}$$

$$\boldsymbol{y}(t) = \boldsymbol{h}(\boldsymbol{x}, t) \tag{3b}$$

Here, $\boldsymbol{x}(t) \in \mathbb{R}^n$ is the system state vector, $\boldsymbol{u}(t) \in \mathbb{R}^p$ is the input vector and $\boldsymbol{y}(t) \in \mathbb{R}^m$ is the output vector. System vector function $\boldsymbol{f}(\boldsymbol{x}, \boldsymbol{u}, t) \in \mathbb{R}^n \times \mathbb{R}^p \times \mathbb{R}^+ \rightarrow \mathbb{R}^n$ defines the state derivatives and the observation vector function $\boldsymbol{h}(\boldsymbol{x}, t) \in \mathbb{R}^n \times \mathbb{R}^+ \rightarrow \mathbb{R}^m$ defines the measurement functions of the system.

Unlike linear systems, where the observability can be determined as a global property and holds for the entire domain $\mathbb{R}^n$ of $\boldsymbol{x}$ [30], in non-linear systems observability is state dependent and is determined locally about a given state. Let us denote the solution to the differential equation 3a by $\boldsymbol{x}(t, \boldsymbol{u}(t), \boldsymbol{x}_o)$ for input $\boldsymbol{u}(t)$ and initial condition $\boldsymbol{x}_o = \boldsymbol{x}(0)$. Let U be an open subset of $\mathbb{R}^n$. A pair of points, $\boldsymbol{x}_o$, $\boldsymbol{x}_1 \in U$, are called U-indistinguishable, if for all bounded measurable inputs $\boldsymbol{u}(t)$ defined in the interval $t \in [0, T]$, for which the solutions $\boldsymbol{x}(t, \boldsymbol{u}(t), \boldsymbol{x}_o)$ and $\boldsymbol{x}(t, \boldsymbol{u}(t), \boldsymbol{x}_1)$ are entirely contained in U, the output trajectories follow the relationship $\boldsymbol{h}(\boldsymbol{x}(t, \boldsymbol{u}(t), \boldsymbol{x}_o), t) = \boldsymbol{h}(\boldsymbol{x}(t, \boldsymbol{u}(t), \boldsymbol{x}_1), t)$. $I_U(\boldsymbol{x}_0)$ represents the set of all points $\boldsymbol{x}_1 \in U$ that are U-indistinguishable form $\boldsymbol{x}_0 \in U$. The system $\sum$ is defined to be locally weakly observable at a state $\boldsymbol{x}_o$, if there exists an open neighbourhood V of $\boldsymbol{x}_o$, such that for every open neighbourhood U of $\boldsymbol{x}_o$, contained in V, $I_U(\boldsymbol{x}_0) = \{\boldsymbol{x}_0\}$.

At any state $\boldsymbol{x}_o$, a non-linear system can be analytically tested for local weak observability by checking the rank of the observability matrix formed by computing the Jacobian of Lie derivatives of the observation equations ($\boldsymbol{h}(\boldsymbol{x}, t)$). A full rank observability matrix (rank = n) means that the system is locally weakly observable at $\boldsymbol{x}_o$. Equation 4 describes the Lie derivatives of the observation equations of $\sum$ and equation 5 describes the observability matrix constructed using the Jacobians of the Lie derivatives as its row vectors. Here, the symbol ∇ represents the gradient operator, defined as $\nabla = [\frac{\partial}{\partial x_1}, \frac{\partial}{\partial x_2}, \frac{\partial}{\partial x_3}, ..., \frac{\partial}{\partial x_n}]$, and the symbol $\otimes$ represents the Kronecker product.

$$\begin{aligned} \mathcal{L}_{\mathrm{f}}^0 \mathbf{h} &= \mathbf{h} \\ \mathcal{L}_{\mathrm{f}}^1 \mathbf{h} &= (\nabla \otimes \mathcal{L}_{\mathrm{f}}^0 \mathbf{h}) \cdot \mathbf{f} \\ &\vdots \\ \mathcal{L}_{\mathrm{f}}^i \mathbf{h} &= (\nabla \otimes \mathcal{L}_{\mathrm{f}}^{i-1} \mathbf{h}) \cdot \mathbf{f} \end{aligned} \tag{4}$$

$$\mathcal{O} = \begin{bmatrix} \nabla \otimes \mathcal{L}_{\mathrm{f}}^{0}\mathbf{h} \\ \nabla \otimes \mathcal{L}_{\mathrm{f}}^{1}\mathbf{h} \\ \vdots \\ \nabla \otimes \mathcal{L}_{\mathrm{f}}^{i}\mathbf{h} \end{bmatrix}, i \in \mathbb{N} \tag{5}$$

Note that this analysis provides a yes or no answer about a system being locally weakly observable at any state, but it does not indicate how well posed the system is to observe [31]. Thus, to check the extent of local observability of a system, we use a measure of observability, known as the degree of observability, as described in section II-H.

C. Case 1: Constant Attitude - Constant Altitude Manoeuvre

We consider a simple model of a MAV manoeuvring with a constant roll angle (ϕ), while keeping its height above ground ($z_{\mathcal{I}}$) constant. It is assumed that the pitch (θ) and yaw (ψ) angles remain zero and so there is no motion in the $X_{\mathcal{I}}$ direction. Further, to keep the altitude constant, it is assumed that the MAV regulates its thrust, T, according to equation 6. Equation 7a describes the motion model for the scenario with state vector $\boldsymbol{x} = [v_{\mathcal{I}}, \phi, z_{\mathcal{I}}]^T$. Equation 7b describes the ventral flow observation equation. We analyse whether the states can be observed in the described scenario through just ventral flow ($\hat{\omega}_y$) observations.

$$\begin{aligned} Tcos\phi - mg &= 0 \\ T &= mgsec\phi \end{aligned} \tag{6}$$

$$\boldsymbol{f}(\boldsymbol{x}, t) = \frac{d}{dt}\begin{bmatrix} v_{\mathcal{I}} \\ \phi \\ z_{\mathcal{I}} \end{bmatrix} = \begin{bmatrix} gtan\phi \\ 0 \\ 0 \end{bmatrix} \tag{7a}$$

$$y_{\hat{\omega}_y} = \frac{-v_{\mathcal{I}} cos^2\phi}{z_{\mathcal{I}}} \tag{7b}$$

Since, the model has three states, to be observable, the observability matrix needs to have rank 3, i.e. at least 3 linearly independent rows. And as the model has only 1 observation, we need at least up to the second order Lie derivative of the observation to construct the observability matrix. Equation 8 describes the Lie derivatives of $y_{\hat{\omega}_y}$. Though the zeroth and first order Lie derivatives (equations 8a and 8b) are linearly independent, the second order Lie derivative (equation 8c) becomes zero and hence all the higher order Lie derivatives are zeros as well. So, calculating Jacobian of the Lie Derivatives would result in an observability matrix with all rows, except the first two rows as zero rows (since gradient of 0 is a null vector). Thus, the observability matrix can at most have rank 2.

$$\mathcal{L}_f^0 y_{\hat{\omega}_y} = \frac{-v_{\mathcal{I}} cos^2\phi}{z_{\mathcal{I}}} \tag{8a}$$

$$\mathcal{L}_f^1 y_{\hat{\omega}_y} = \frac{-gsin2\phi}{2z_{\mathcal{I}}} \tag{8b}$$

$$\mathcal{L}_f^2 y_{\hat{\omega}_y} = 0 \tag{8c}$$

This result shows that by observing just the ventral flow measurements, it is not possible to estimate the absolute values of all the three states. However, if the knowledge about one of those states is provided, the other two can be uniquely observed (except at those state values where the rank of $\mathcal{O}$ is less than 2). The application of this result can be seen in various works [17][18], where the researchers have used a separate sensor setup, like sonar or stereo camera, to measure a MAV's height and used this information to decouple the velocity and height in the ventral flow measurements, thus estimating the absolute value of MAV's velocity. The result presented here also suggests that the height measurements can be used to not only estimate absolute velocities, but attitude as well, which, to our best knowledge, has not been utilized in literature yet.

The model presented in this case is based on two important assumptions: the MAV maintains constant roll attitude and constant height. In the subsequent two cases, we relax each of these assumptions and analyse the effect this has on system observability. Further, the case presented here considers the ventral flow values as the only observation. In section II-F we include the divergence values as another measurement and analyse its influence on the system observability.

D. Case 2: Varying Attitude - Constant Altitude Manoeuvre

In this scenario, we consider the motion model (equation 9a) of a MAV manoeuvring at a constant $z_{\mathcal{I}}$ but with varying ϕ. To vary ϕ (and roll rate p), roll moment ($M_{x_{\mathcal{B}}}$) is considered as an input to the system. The rationale behind considering the moment as the system input is that an estimate of the the moment applied on the MAV can be obtained from the rotor velocities or the roll moment commands sent from the flight controller to the rotors. This aspect of the model has been further discussed in section IV-B. $I_{x_{\mathcal{B}}}$ represents the moment of inertia of the MAV around its $X_{\mathcal{B}}$ axis. Equation 9b describes the ventral flow observation equation.

$$\boldsymbol{f}(\boldsymbol{x}, t) = \frac{d}{dt}\begin{bmatrix} v_{\mathcal{I}} \\ \phi \\ p \\ z_{\mathcal{I}} \end{bmatrix} = \begin{bmatrix} gtan\phi \\ p \\ M_{x_{\mathcal{B}}}/I_{x_{\mathcal{B}}} \\ 0 \end{bmatrix} \tag{9a}$$

$$y_{\hat{\omega}_y} = \frac{-v_{\mathcal{I}} cos^2\phi}{z_{\mathcal{I}}} + p \tag{9b}$$

The observability rank condition renders the described system locally weakly observable. For brevity, the observability analysis of this model is not being included in the article, but can be referred to, in appendix A. For the reader's understanding, observability analysis of a simplified system model (equation 10), which in terms of observability is analogous to the system in equation 9, is being presented here. The model is simplified by assuming roll rate p as an input to the system instead of the moment $M_{x_{\mathcal{B}}}$. Thus, through this simplification, we reduce the four state model ($\boldsymbol{x} = [v_{\mathcal{I}}, \phi, p, z_{\mathcal{I}}]^T$) into a three state model ($\boldsymbol{x} = [v_{\mathcal{I}}, \phi, z_{\mathcal{I}}]^T$).

$$\boldsymbol{f}(\boldsymbol{x},t) = \frac{d}{dt}\begin{bmatrix} v_{\mathcal{I}} \\ \phi \\ z_{\mathcal{I}} \end{bmatrix} = \begin{bmatrix} gtan\phi \\ p \\ 0 \end{bmatrix} \tag{10a}$$

$$y_{\hat{\omega}_y} = \frac{-v_{\mathcal{I}} cos^2\phi}{z_{\mathcal{I}}} + p \tag{10b}$$

Equation 11 lists the Lie derivatives, up to the second order, of the observation considered in this model. The lie derivatives are linearly independent and calculating their Jacobians to construct the observability matrix leads to a matrix with linearly independent rows, thus a full rank observability matrix (equation 12).

$$\mathcal{L}_f^0 y_{\hat{\omega}_y} = \frac{-v_{\mathcal{I}} cos^2\phi}{z_{\mathcal{I}}} + p \tag{11a}$$

$$\mathcal{L}_f^1 y_{\hat{\omega}_y} = -\frac{sin2\phi(g - 2pv_{\mathcal{I}})}{2z_{\mathcal{I}}} \tag{11b}$$

$$\mathcal{L}_f^2 y_{\hat{\omega}_y} = \frac{p(g - 2gcos2\phi + 2pv_{\mathcal{I}} cos2\phi)}{z_{\mathcal{I}}} \tag{11c}$$

$$\mathcal{O} = \begin{bmatrix} \frac{-cos^2\phi}{z_{\mathcal{I}}} & \frac{v_{\mathcal{I}} sin2\phi}{z_{\mathcal{I}}} & \frac{v_{\mathcal{I}} cos^2\phi}{z_{\mathcal{I}}^2} \\ \frac{psin2\phi}{z_{\mathcal{I}}} & \frac{-cos2\phi(g - 2pv_{\mathcal{I}})}{z_{\mathcal{I}}} & \frac{sin2\phi(g - 2pv_{\mathcal{I}})}{2z_{\mathcal{I}}^2} \\ \frac{2p^2 cos2\phi}{z_{\mathcal{I}}} & \frac{psin2\phi(4g - 4pv_{\mathcal{I}})}{z_{\mathcal{I}}} & \frac{-p(g - 2gcos2\phi + 2pv_{\mathcal{I}} cos2\phi)}{z_{\mathcal{I}}^2} \end{bmatrix} \tag{12}$$

Note that the only difference between this model and the model considered in the previous sub-section (equation 7) is that ϕ is no longer constant and it is assumed that we know the value of its time derivative (p as input). Further, the model in equation 9, where it is considered that the second derivative of ϕ is known ($M_{x_\mathcal{B}}$ as input), also results in a full rank observability matrix. Analysing the observability matrices, it can be intuitively concluded that if information about a time derivative, of any order, of ϕ is actuated and is known, the system states can be estimated by measuring just the ventral flow. This result mathematically proves that the attitude of a MAV can be estimated through optical flow information and moment efference copies, which is a key contribution of this article.

Even though we claim the observability matrix in equation 12 to be full rank, there might be state-input values that render the matrix singular. As such, the system is not observable at those states. For example, the matrix rank drops to 2 if the value of input p is set to zero. Similarly, the system represented by equation 9 becomes unobservable, when the input M and state p simultaneously have the value zero. However, there may exist many other state-input value combinations where these models become unobservable, and deriving all those conditions is difficult. Hence, we define a measure of observability, called the degree of observability, in section II-H to analyse the observability of the systems as values of the states and inputs vary.

E. Case 3: Constant Attitude - Varying Altitude Manoeuvre

In this section, the assumption of constant attitude manoeuvre is re-established, but now we investigate what happens when the height of the MAV varies. Since the altitude no longer remains constant, thrust T cannot be regulated according to the equation 6. So, T is assumed to be an input to the system. The motion model of the system is described by equation 13a, where m represents the mass of the MAV. As has been done in the previous cases, we test the observability of the system when only the ventral flow is observed, as described by equation 13b.

$$\boldsymbol{f}(\boldsymbol{x},t) = \frac{d}{dt}\begin{bmatrix} v_{\mathcal{I}} \\ \phi \\ z_{\mathcal{I}} \\ w_{\mathcal{I}} \end{bmatrix} = \begin{bmatrix} Tsin\phi/m \\ 0 \\ w_{\mathcal{I}} \\ Tcos\phi/m - g \end{bmatrix} \tag{13a}$$

$$y_{\hat{\omega}_y} = \frac{-v_{\mathcal{I}} cos^2\phi}{z_{\mathcal{I}}} + \frac{w_{\mathcal{I}} sin2\phi}{2z_{\mathcal{I}}} \tag{13b}$$

The observability test (refer appendix B) for the system described, results in a full rank matrix. Here the knowledge of thrust input (vertical acceleration) along with the ventral flow measurements renders the system observable. Through further inspection of the terms in the observability matrix it can be concluded that if the time derivative of height, of any order, is actuated and is known, then the states of the system can be observed by measuring the ventral flow. This result is an extension of the result obtained by the authors in [28], where they use flow divergence and thrust efference copies to estimate the height and vertical velocity of a MAV. The result obtained by our analysis proves that the same approach can be used to estimate attitude and lateral velocity of the MAV as well.

F. Case 4: Constant Attitude - Constant Altitude Manoeuvre: Measuring Ventral Flow and Divergence

Now that we have derived that the MAV attitude is observable through ventral flow measurements, if the height and/or the attitude vary and the control efference copies (thrust and/or moment) are known, we go back to our initial case of constant attitude-constant altitude manoeuvre and review the system observability when divergence is also used as an observation along with ventral flow. Equation 14a describes the motion model and equation 14b describes the ventral flow and the divergence measurements.

$$\boldsymbol{f}(\boldsymbol{x},t) = \frac{d}{dt}\begin{bmatrix} v_{\mathcal{I}} \\ \phi \\ z_{\mathcal{I}} \end{bmatrix} = \begin{bmatrix} gtan\phi \\ 0 \\ 0 \end{bmatrix} \tag{14a}$$

$$\boldsymbol{y} = \begin{bmatrix} y_{\hat{\omega}_y} \\ y_{\hat{\omega}_z} \end{bmatrix} = \begin{bmatrix} \frac{-v_{\mathcal{I}} cos^2\phi}{z_{\mathcal{I}}} \\ \frac{-v_{\mathcal{I}} sin2\phi}{2z_{\mathcal{I}}} \end{bmatrix} \tag{14b}$$

Equation 15 lists the Lie derivatives of the observation equation up to the first order. For the system to be locally

weakly observable, the observability matrix needs to have 3 linearly independent rows. The first two rows are formed by the Jacobian of the zeroth order Lie derivative of the observation vector. The third row is obtained by the first order lie derivative of $y_{\hat{\omega}_y}$. This leads to a full rank observability matrix as in equation 16.

$$\mathcal{L}_f^0 \boldsymbol{y} = \begin{bmatrix} \frac{-v_{\mathcal{I}} cos^2\phi}{z_{\mathcal{I}}} \\ \frac{-v_{\mathcal{I}} sin2\phi}{2z_{\mathcal{I}}} \end{bmatrix} \tag{15a}$$

$$\mathcal{L}_f^1 \boldsymbol{y} = \begin{bmatrix} \frac{-gsin2\phi}{2z_{\mathcal{I}}} \\ \frac{-gsin^2\phi}{z_{\mathcal{I}}} \end{bmatrix} \tag{15b}$$

$$\mathcal{O} = \begin{bmatrix} \nabla \otimes \mathcal{L}_f^0 \boldsymbol{y} \\ \nabla \otimes \mathcal{L}_f^1 y_{\hat{\omega}_y} \end{bmatrix} = \begin{bmatrix} \frac{-cos^2\phi}{z_{\mathcal{I}}} & \frac{v_{\mathcal{I}} sin2\phi}{z_{\mathcal{I}}} & \frac{v_{\mathcal{I}} cos^2\phi}{z_{\mathcal{I}}^2} \\ \frac{-sin2\phi}{2z_{\mathcal{I}}} & \frac{-v_{\mathcal{I}} cos2\phi}{z_{\mathcal{I}}} & \frac{v_{\mathcal{I}} sin2\phi}{2z_{\mathcal{I}}^2} \\ 0 & \frac{-gcos2\phi}{z_{\mathcal{I}}} & \frac{gsin2\phi}{2z_{\mathcal{I}}^2} \end{bmatrix} \tag{16}$$

Thus, though the system is unobservable when only the ventral flow measurements are used (section II-C), the states can be estimated if the divergence information is also utilized. Further, we can intuitively deduce that including the divergence measurements in the models presented in cases 2 and 3 (sections II-D and II-E) would improve the system observability, since it will reduce the order of Lie derivatives of the observations required to obtain a full rank observability matrix. Gathering the conclusions of the analysis presented in sections II-C - II-F, a complete model of optical flow based roll attitude estimation of a MAV is formulated in the next section.

G. Complete Model

In this section, we consider the motion model of a MAV free to manoeuvre in the $\mathcal{Y}_{\mathcal{I}}$-$\mathcal{Z}_{\mathcal{I}}$ plane, i.e. though it is no longer assumed that the MAV maintains constant roll angle and height, we still assume that the MAV maintains zero pitch and yaw angles and hence there is no motion along the $X_{\mathcal{I}}$ axis. Consequently the motion model has two inputs: moment $M_{x_{\mathcal{I}}}$ and thrust T control efference copies. The system also has two observations: ventral flow $\hat{\omega}_y$ and divergence $\hat{\omega}_z$. The equations describing the system, represented by $\sum_1$, are stated as:

$$\boldsymbol{f}(\boldsymbol{x}, t) = \frac{d}{dt} \begin{bmatrix} v_{\mathcal{I}} \\ \phi \\ p \\ z_{\mathcal{I}} \\ w_{\mathcal{I}} \end{bmatrix} = \begin{bmatrix} Tsin\phi/m \\ p \\ M_{x_{\mathcal{B}}}/I_{x_{\mathcal{B}}} \\ w_{\mathcal{I}} \\ Tcos\phi/m - g \end{bmatrix} \tag{17a}$$

$$\boldsymbol{y} = \begin{bmatrix} y_{\hat{\omega}_y} \\ y_{\hat{\omega}_z} \end{bmatrix} = \begin{bmatrix} \frac{-v_{\mathcal{I}} cos^2\phi}{z_{\mathcal{I}}} + \frac{w_{\mathcal{I}} sin2\phi}{2z_{\mathcal{I}}} + p \\ \frac{-v_{\mathcal{I}} sin2\phi}{2z_{\mathcal{I}}} - \frac{w_{\mathcal{I}} cos^2\phi}{z_{\mathcal{I}}} \end{bmatrix} \tag{17b}$$

From the inferences drawn in the previous sections, it can be deduced that $\sum_1$ is locally weakly observable. The observability analysis for the system has been described in appendix C for reference. In the subsequent sections of the article, the model of system $\sum_1$ has been considered to design a state estimator and the performance of the estimator has been verified through simulations and experiments. In the following subsection, a measure of system observability has been defined to monitor how observable a system is at various state-input values.

H. Degree of Observability

So far, we have used the local weak observability analysis to examine the system's observability for various motion models. However, the observability matrix rank condition only returns a yes or no answer about a system's observability and does not provide any insight about how feasible it is to observe the system [31]. Thus, establishing a measure of observability is crucial for the analysis of the system at various state-input values.

Krener and Ide [31] introduced the local estimation condition number (κ) to measure the local observability of a non linear system and the well-posedness of the estimation problem. The local estimation condition number is the ratio of the largest singular value of the local observability matrix to the smallest:

$$\kappa(\mathcal{O}) = \frac{\sigma_{max}(\mathcal{O})}{\sigma_{min}(\mathcal{O})} \tag{18}$$

$$DO(\mathcal{O}) = \frac{1}{\log(\kappa(\mathcal{O}))} \tag{19}$$

Where, $\sigma_{max}(\mathcal{O})$ and $\sigma_{min}(\mathcal{O})$ represent the maximum and minimum local singular values of matrix $\mathcal{O}$. High value of κ suggests that the observability matrix is ill-conditioned, with κ of a singular matrix being infinity, and low values of κ suggest that the matrix is well-posed, with κ of an identity matrix being 1. The condition number has been adopted as a measure of observability in several studies [32][33]. In this article, we have adopted the reciprocal of the $\log$ of κ as the degree of observability, DO, of the system, as described in equation 19. This has been done to have the values of DO vary between 0 and 1, with higher values of DO signifying higher observability of the system. In the following subsection, we use DO to analyse how excitation of various motion states and inputs affect the observability of system $\sum_1$ and compare the observability of $\sum_1$ with a system where de-rotated ventral flow values are measured.

I. Effect of Optical Flow De-Rotation on Observability

De-rotation of optical flow field is a common practice in vision based navigation applications [18][21]. De-rotation is

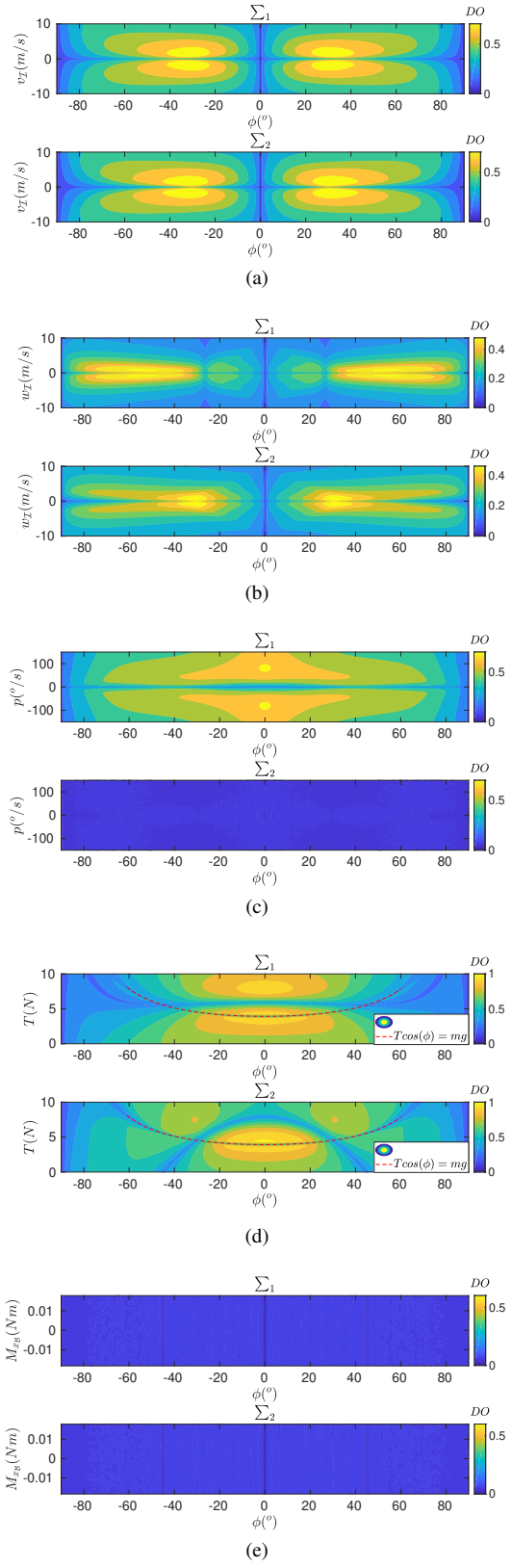

Fig. 2: Degree of observability contour maps for variation in values of motion states and inputs against values of roll angle ϕ, for the systems: $\sum_1$ that observes the full ventral flow component and $\sum_2$ that observes the de-rotated ventral flow components. (a) $v_{\mathcal{I}}$ variation, (b) $w_{\mathcal{I}}$ variation, (c) p variation, (d) T variation, (e) $M_{x_{\mathcal{B}}}$ variation.

only possible when sensors measuring the rotational rates are available. Since in this study we intend to use optical flow vectors as the only sensory information, de-rotation of the flow field is not feasible. However, it is interesting to analyse the effect of de-rotation on the system observability. In this sub-section we analyse how the excitation of various motion states and inputs affect the observability of system $\sum_1$ (equation 17) and compare $\sum_1$ with a system where de-rotated ventral flow measurements are used. Let us denote this second system by $\sum_2$. System $\sum_2$ is the same as $\sum_1$ except that instead of observing the full ventral flow component (equation 17b), $\sum_2$ observes the de-rotated ventral flow components, as described by equation 20.

$$y_{\hat{\omega}_{y_{\sum_2}}} = \frac{-v_{\mathcal{I}} cos^2\phi}{z_{\mathcal{I}}} + \frac{w_{\mathcal{I}} sin2\phi}{2z_{\mathcal{I}}} \tag{20}$$

Since the focus of our investigation is on attitude estimation, we analyse the observability of the systems through figure 2 that depicts the DO contour maps for values of the motion states ($v_{\mathcal{I}}$, $w_{\mathcal{I}}$, p) and inputs (T, $M_{x_{\mathcal{B}}}$) against values of roll angle (ϕ). During the excitation of a particular motion state/input the other states and inputs are kept at their neutral values. The neutral values of the states and inputs are defined as: $v_{\mathcal{I}_0} = 0m/s$, $w_{\mathcal{I}_0} = 0m/s$, $p_0 = 0^o/s$, $T_0 = mgsec\phi$, $M_0 = 0Nm$. T_0 is defined such that the $Z_{\mathcal{I}}$ component of the thrust balances the weight (mg) of the MAV, hence maintaining the vertical acceleration of the MAV at $0m/s^2$. The height of the MAV is set at $z_{\mathcal{I}} = 1m$ and the values of mass and moment of inertia are kept similar to a Parrot Bebop quadcopter ($m = 0.4kg$ and $I_{x_{\mathcal{B}}} = 0.0018244kgm^2$), since the same has been used for experimental verification of the proposed estimator in section IV.

It can be observed from figure 2 that both the systems need motion to be observable, i.e. both the systems remain unobservable when all the motion states and inputs are maintained at their neutral values. This is an expected phenomenon since optical flow measurements are being used that require motion to be non-zero. The observability variation with $v_{\mathcal{I}}$ excitation (figure 2a) remains similar for both the systems. System $\sum_1$ registers higher values of DO for a broader range of ϕ, than $\sum_2$, when $w_{\mathcal{I}}$ is excited (figure 2b). However, at smaller values of angle ϕ, excitation in either $v_{\mathcal{I}}$ or $w_{\mathcal{I}}$, does not augment the system observability and both the systems remain unobservable. The only motion state whose non-zero value renders the system observable at small values of angle ϕ, while other states and inputs remain neutral, is p (figure 2c). However, $\sum_2$ remains unobservable, irrespective of the value of p, when other motion states and inputs are kept at their neutral values. This demonstrates that by de-rotation of optical flow field valuable information is lost, which otherwise, can be leveraged to estimate the MAV motion. Thus, we will use the model of $\sum_1$ to design our state estimator, as will be discussed in section III-B.

Figure 2 also highlights several other interesting details about the variation of the system observability with the variation in state and input values. The observability of the system increases with the initial increase in the absolute values of the motion states. However, for fast manoeuvres (with

$|p| > 150^o/s$ and $|u|, |v| > 5m/s$) the observability of the system deteriorates. Further, along with p, excitation of T about its neutral values also renders the systems observable at small values of ϕ (figure 2d). Note, that in figure 2d the red dashed line represents the locus of neutral values of T, i.e. the points where $T = mgsec\phi$, and both the systems remain unobservable along this line. So, even at the instants when the MAV is not moving (does not have a finite velocity), a non-neutral thrust input to the system, that induces a finite vertical acceleration, will render the system states observable. However, the same does not hold true for moments, i.e. when all the other states and inputs are maintained at their neutral values, variation of moment values does not augment the system observability, as revealed by figure 2e. Thus, it can be inferred that for slow manoeuvres, thrust inputs are more effective than moment inputs, in rendering the states (including attitude) observable.

In this section, through non-linear observability analysis, we have theoretically established that it is feasible to estimate the attitude of a flying robot using optical flow measurements and the knowledge of efference copy inputs. In the next section, we use the structure of system $\sum_1$ to design an extended Kalman filter, whose performance is verified in simulations.

III. Verification through Simulations

In this section, we intend to verify the findings of the observability analysis through simulations. An Extended Kalman Filter (EKF) state estimator has been designed based on the structure of system $\sum_1$, described by equation 17 in section II-G. First, the designed estimator has been tested in a noise-delay free scenario, to verify its convergence and the findings of the observability analysis. Then, the effects of noise and delays, in various inputs and measurements, on the EKF's performance have been analysed. The estimator's performance has also been verified against simultaneous discrepancies in various inputs and measurements. Further, the state estimates obtained from the EKF have been used to perform closed loop attitude and altitude control of the simulated MAV and the effect of optical flow sample rate on the controller's stability has been analysed.

A. Simulated System

A 3 degrees of freedom (3-DoF: free to move in the $Y_{\mathcal{I}}Z_{\mathcal{I}}$ plane and rotate about the $X_{\mathcal{I}}$ axis) quadcopter model has been simulated whose dynamics is governed by the motion model of $\sum_1$ as described in equation 17a. The mass and moment of inertia of the MAV are set similar to a Bebop quadcopter. It is also assumed that the MAV has perfect noise free knowledge of its states and hence a feedback PD control loop has been implemented to stabilize and control the MAV's flight.

Figure 3 depicts the response of the simulated MAV to simultaneous reference step inputs in roll angle ϕ and height $z_{\mathcal{I}}$. This manoeuvre of the MAV will be used as a standard manoeuvre to test the performance of the estimator designed in section III-B. This particular manoeuvre has been chosen to test the estimator in simulation, since it effectively combines: hover ($t < 20s$, $t > 80s$), rotational motion ($t \approx 20s$), vertical motion ($t \approx 80s$) and simultaneous rotational and vertical motion ($t \approx 40s$).

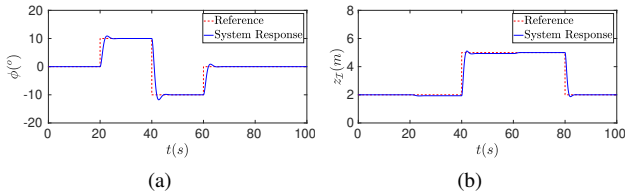

(a) (b)

Fig. 3: Response of the simulated MAV system to simultaneous reference step inputs in (a) roll angle (ϕ) and (b) height ($z_{\mathcal{I}}$).

B. Filter Design

An EKF state estimator [34] has been implemented to estimate the MAV's states. This choice of the filter has been made since the EKF fits well with the way the motion model has been described (section II-G) as the EKF also uses a state function model and observation model which can be kept exactly as they have been described in equation 17.

In the quadcopter, used in this study to verify the proposed estimator (section IV), the inner stabilization loop runs at 500Hz. Capturing images from the bottom camera of the quadcopter and using a standard vision pipeline (section IV-C), optical flow measurements can be sampled at an average rate of 30Hz. To keep the simulations realistic and in-line with the experimental platform, the simulated EKF is run at 500Hz, while the optical flow measurements are sampled at 30Hz. Since optical flow observables are the only measurements being used by the EKF, during the iterations when optical flow is not sampled, the measurement update step in the EKF is not performed.

C. Noise-Delay Free Estimation

We start the simulation analysis with an ideal noise-delay free scenario. The noise free scenario has been specifically chosen to check the convergence of the designed EKF and verify the inferences drawn from the observability analysis. Step references in ϕ and $z_{\mathcal{I}}$, as depicted in figure 3, are given as inputs and response of the MAV model is estimated using the EKF.

Figure 4 depicts the state estimation results for the noise-delay free scenario. It can be observed that the EKF converges to provide accurate state estimates. Moreover, on close inspection of the $\pm 3\sigma$ estimation error bands, obtained from the estimation error covariance, the findings of the observability analysis can be further verified. Figure 5 depicts the variation of degree of observability, DO, during the manoeuvre. The estimation error variances for all the states remain high till $t = 20s$ as the MAV is in hover and the system observability remains low due to lack of motion. At $t = 20s$ a moment input is provided to increase ϕ in response to the step reference. The

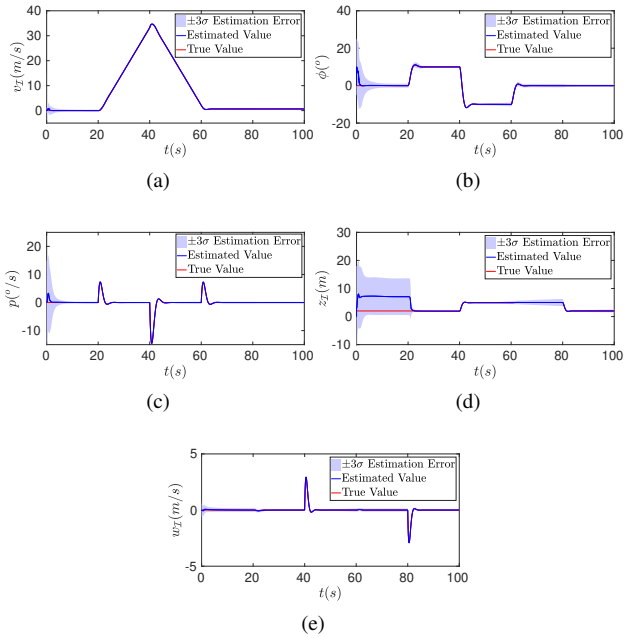

Fig. 4: Estimation results for an ideal noise-delay free scenario. (a) Horizontal velocity $v_{\mathcal{I}}$, (b) roll angle ϕ, (c) roll rate p, (d) height $z_{\mathcal{I}}$ and (e) vertical velocity $w_{\mathcal{I}}$

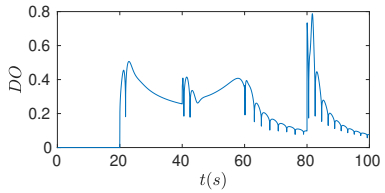

Fig. 5: Variation of degree of observability DO during the manoeuvre depicted in figure 3. Higher values of DO signify higher observability of the system, with $DO = 1$ for an identity observability matrix and $DO = 0$ for a singular observability matrix.

moment input increases p. This excitation in the motion states and the input increases the observability of the system resulting in the convergence of state estimates to the true values of the states and decrease in the estimation error variance. As soon as the MAV achieves the reference attitude, all motion states and inputs return to their neutral values, except $v_{\mathcal{I}}$. However, as concluded from the observability analysis, the system exhibits low observability for high values of $v_{\mathcal{I}}$ (figure 2a). Therefore, the observability degree slightly decreases with increasing velocity between $t = 20s$ and $t = 40s$, and increases again at $t = 40s$ when the system is excited through inputs in both T and $M_{x_{\mathcal{B}}}$. Now, between $t = 40s$ to $t = 60s$ the only non-neutral state of the MAV is again $v_{\mathcal{I}}$, which decreases at a constant rate during this interval. So, the system observability registers a slight rise during the interval. At $t = 60s$ the observability degree momentarily rises because of moment inputs and thus the error variances in the state estimates decrease, but after the application of the moment, the MAV returns to a hovering state and due to which the observability rapidly drops, while the errors in state estimates increase. At, $t = 80s$ an excitation in T is applied to reduce the height of the MAV which momentarily increases the observability and decreases the error covariance of estimation, but once again after $t = 80s$, the MAV returns to hover and hence the observability of the system and estimation error covariance deteriorates.

Though analysing the noise-delay free scenario is a good method to verify convergence of the EKF and confirm the findings of the observability analysis, in real scenarios the measurements and inputs to the system are corrupted with noise and delays. Hence, it is important to test the performance of the estimator in scenarios with noise and delays. In the following sections we analyse the effects of noise and delays in the optical flow measurements and efference copy inputs.

D. Effects of Noise and Delays in Optical Flow Measurements

Though in simulations the optical flow measurements are computed through equation 17b, in real applications optical flow vectors are obtained by processing the image frames captured by the on-board camera (the algorithms that have been used to compute the optical flow measurements during the experiments are discussed in section IV-C). These algorithms, calculating optical flow, are often based on ideal assumptions and not confirming to these assumed conditions introduces discrepancies in the obtained values. Further, the processing the computer vision algorithms also introduces lags in the system. Thus, in real world scenarios, the optical flow measurements are corrupted with irregular noise and delays. Examining the robustness of the estimator against noisy-delayed optical flow data is necessary to verify its feasibility in real applications. In this subsection, the performance of the estimator is analysed against different levels of noise and delays in the ventral flow and divergence observations.

Since the focus of this study is to estimate the attitude of a MAV, we adopt the Root Mean Square Error (RMSE) in attitude estimates as the measure of estimator accuracy in this article. For a Kalman filter (KF), RMSE is the most natural finite-sample approximation of standard deviation in estimation errors [35], and since a KF is designed to minimize the Mean Squared Error (MSE) of predictions, RMSE provides an intuitive measure of the filter performance. As such, RMSE is one of the most popular measures of estimation accuracy [35], [36], [37]. Equation 21a defines the RMSE in estimated values of a state x at each time instant, when the estimator is run N times for different noise realizations. The obtained values are averaged over the time duration of the whole trajectory to calculate the Average RMSE (ARMSE) values as defined in equation 21b.

$$RMSE_x(t) = \sqrt{\frac{\sum_{k=1}^{N}(\hat{x}_k(t) - x_k(t))^2}{N}} \tag{21a}$$

TABLE I: ARMSE in roll angle (ϕ) estimates for various levels of Gaussian noise in optical flow measurements. Noise standard deviation (σ) values are in rad/s and s^{-1} for ventral flow and divergence measurements respectively.

Measurement	Noise σ	$ARMSE_\phi$ (^{o})
Ventral Flow $y_{\dot{\omega}_y}$	0.01	0.26
	0.10	0.36
	0.50	1.19
	1.00	3.28
Divergence $y_{\dot{\omega}_z}$	0.01	0.26
	0.10	0.31
	0.50	1.66
	1.00	2.47

TABLE II: ARMSE in roll angle (ϕ) estimates for various levels of delay in optical flow measurements.

Measurement	Delay (s)	$ARMSE_\phi$ (^{o})
Ventral Flow $y_{\dot{\omega}_y}$	0.04	0.29
	0.20	0.44
	0.50	0.76
	1.00	1.23
Divergence $y_{\dot{\omega}_z}$	0.04	0.28
	0.20	0.41
	0.50	0.64
	1.00	1.04

$$ARMSE_x = \frac{\sum_{t=0}^{T} RMSE_x(t)}{\tau} \tag{21b}$$

Where, $\hat{x}$ represents the estimated values of state x and τ represents the total time duration of the performed manoeuvre.

The EKF is tested for various Gaussian noise and delay levels in the ventral flow and divergence measurements, as listed in tables I and II. To compensate for the randomness introduced due to Gaussian noise generation, for each scenario, the simulator is run for 50 different noise realizations. While analysing the estimator against noise/delay in a particular measurement, the other measurements and inputs of the system are kept noise-delay free. The resulting $RMSE_\phi$ time variations are depicted in figure 6 and tables I and II list the $ARMSE_\phi$ values.

The EKF registers high estimation errors for noise standard deviation of order 1 rad/s and 1 s^{-1} (for ventral flow and divergence measurements respectively) which of course are quite high values. However, for more realistic noise values, the filter converges and performs satisfactorily well. The EKF is tested for delays as high as $1s$ in the optical flow measurements and the estimator proves to be robust to those delays. The $RMSE_\phi$ time variation, as depicted in figures 6d and 6b, reveals that the estimator is more sensitive to measurement delays during rotations than during vertical manoeuvres. This result is in line with the inference drawn during observability analysis, in section II-H, that excitation in T is more effective in augmenting the system observability, than excitation in $M_{x_\mathcal{B}}$. Further, the $RMSE_\phi$ peaks at $t \approx 40s$ and $t \approx 80s$ are higher in figure 6b than in figure 6d, thus indicating that the estimator is more sensitive to delays in divergence measurements than ventral flow measurements during vertical manoeuvres. This is to be expected, since at low roll angles, ventral flow observations contain significantly less information about the MAV's vertical motion than the divergence observations. Here, the term vertical refers to the $Z_\mathcal{I}$ direction.

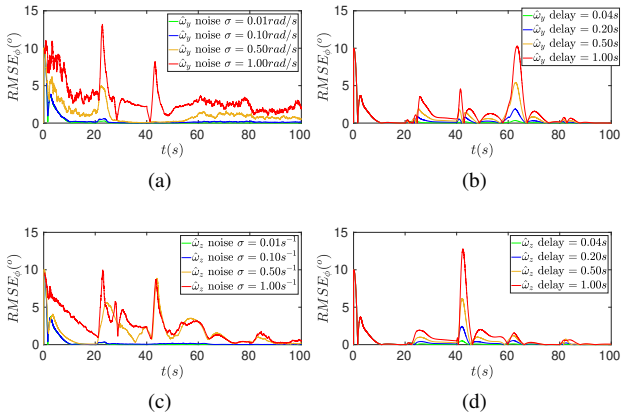

Fig. 6: Variation of RMSE in ϕ estimates ($RMSE_\phi$) with time, for different levels of noise and delays in optical flow measurements. RMSE values have been calculated over 50 runs of the simulator with different noise realizations. (a) $RMSE_\phi$ variation for different levels of noise in ventral flow measurements, (b) $RMSE_\phi$ variation for different levels of delays in ventral flow measurements, (c) $RMSE_\phi$ variation for different levels of noise in divergence measurements, (d) $RMSE_\phi$ variation for different levels of delays in divergence measurements.

E. Effects of Noise and Delays in Efference Copy Inputs

Along with optical flow measurements, the estimator also makes use of the knowledge of efference copies (thrust T and moment $M_{x_\mathcal{B}}$) to estimate the MAV's states. However, these efference copy inputs are not readily available and have to be estimated from the control commands sent to the MAV's actuators or the MAV's motor speeds. The models used to estimate the efference inputs are not perfect and involve certain discrepancies, as discussed in section IV-B. Thus, to be feasible in real robot applications, the estimator needs to be robust to those discrepancies. In this subsection, the estimator performance is examined against various levels of Gaussian noise and delays in thrust and moment inputs to the EKF. As has been done in the previous subsection, during each studied scenario, the noise and delays in other inputs and measurements are kept zero. The EKF is tested over 50 simulation runs, for each case, with different noise realizations. Tables III and IV list the $ARMSE_\phi$ values and figure 7 depicts the time variation of $RMSE_\phi$ values for various levels of noise and delays in the efference copy inputs. Note that the noise standard deviations for T and $M_{x_\mathcal{B}}$ are represented in proportion to m and $I_{x_\mathcal{B}}$ respectively. This has been done to make the values more representative of the noise introduced in acceleration and angular acceleration of the MAV, thus making the analysis more intuitive.

Interestingly, the estimator is robust to high values of noise in T (tested for noise standard deviation as high as $5m$ N), however, loses its stability for delays in T inputs approaching $1s$. On the other hand, the estimator converges for delays and

TABLE III: ARMSE in roll angle (ϕ) estimation for various levels of Gaussian noise in efference copy inputs. Noise standard deviation (σ) values are proportional to $I_{x_\mathcal{B}}$ and m for moment and thrust respectively.

Input	Noise σ	$ARMSE_\phi$ (^{o})
Moment $M_{x_\mathcal{I}}$	$0.01I_{x_\mathcal{B}}$	0.32
	$0.05I_{x_\mathcal{B}}$	0.58
	$0.10I_{x_\mathcal{B}}$	0.91
	$0.50I_{x_\mathcal{B}}$	6.79
Thrust T	$0.10m$	0.25
	$0.50m$	0.26
	$1.00m$	0.27
	$5.00m$	0.35

TABLE IV: ARMSE in roll angle (ϕ) estimation for various levels of delay in efference copy inputs.

Input	Delay (s)	$ARMSE_\phi$ (^{o})
Moment $M_{x_\mathcal{I}}$	0.04	0.28
	0.20	0.40
	0.50	0.64
	1.00	1.02
Thrust T	0.04	0.26
	0.20	0.32
	0.50	0.69
	1.00	156.71

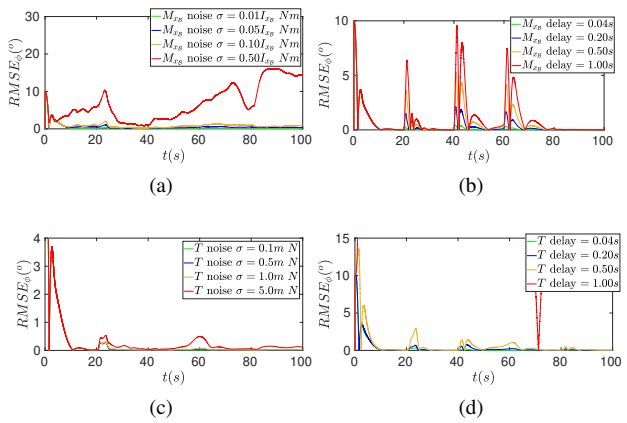

Fig. 7: Variation of RMSE in ϕ estimates ($RMSE_\phi$) with time for different levels of noise and delays in efference copy inputs. RMSE values have been calculated over 50 simulation runs with different noise realizations. (a) $RMSE_\phi$ variation for different levels of noise in moment input, (b) $RMSE_\phi$ variation for different levels of delays in moment input, (c) $RMSE_\phi$ variation for different levels of noise in thrust input, (d) $RMSE_\phi$ variation for different levels of delays in thrust input.

noise in $M_{x_\mathcal{B}}$ inputs as high as $1s$ and $0.1I_{x_\mathcal{B}}$, but registers high $ARMSE_\phi$ values. Thus, estimation accuracy in ϕ is more robust to discrepancies in T inputs as long as the lag remains low, but discrepancies in $M_{x_\mathcal{B}}$ inputs result in higher inaccuracy in ϕ estimates. The sensitivity of the estimator to inaccurate $M_{x_\mathcal{B}}$ values can be reasoned as the attitude is more directly related to the moments (second derivative) than the thrust values. The implications of this subsection's findings are discussed in section IV-B where models to estimate T and $M_{x_\mathcal{B}}$ are obtained to test the estimator with real flight data.

F. Estimation in presence of noise and delays

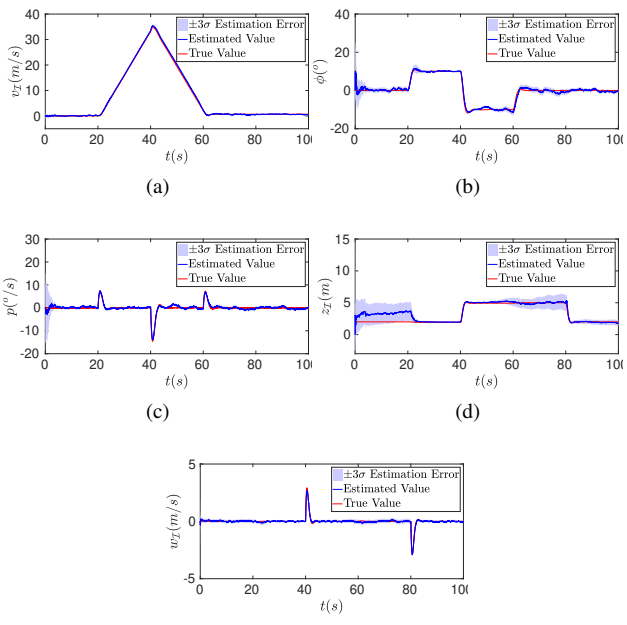

Fig. 8: Estimation results in presence of noise and delays in the measurements and inputs. (a) Horizontal velocity $v_\mathcal{I}$, (b) roll angle ϕ, (c) roll rate p, (d) height $z_\mathcal{I}$ and (e) vertical velocity $w_\mathcal{I}$

Simulating the estimator with noise and lags in a particular input or measurement, while keeping other inputs and measurements noise free, is an apt method of analysing the sensitivity of the EKF to discrepancies in particular inputs and measurements. However, while functioning in a real robot, the estimator has to perform against simultaneous discrepancies in various measurements and inputs. In this subsection, the estimator is tested in presence of noise and delays, representative of the values expected to be experienced in a real robot, in all the measurements and inputs.

The moment and thrust inputs to the EKF are lagged by $0.04s$ delay each and polluted with Gaussian noise having standard deviation values $0.1I_{x_\mathcal{B}}$ and $0.5m$ respectively. To simulate the external disturbances experienced by a flying MAV, moment and thrust inputs to the simulated MAV system are corrupted with Gaussian noise having standard deviation values $0.05I_{x_\mathcal{B}}$ and $0.1m$ respectively. Further, a lag of $0.1s$ and Gaussian noise with standard deviation values $0.1rad/s$ and $0.1s^{-1}$ respectively, are added to the ventral flow and divergence measurements.

Figure 8 depicts the estimation results obtained for the described scenario. Due to the presence of noise and delays, the estimation uncertainty, depicted by the blue $\pm 3\sigma$ error band, is more compared to the noise-free scenario (figure 4), however it follows the same variation trends as described in section III-C. Thus, further verifying the inferences drawn from the observability analysis in section II-H.

To analyse convergence of the EKF, measurement innovations (or residuals) are utilized. Measurement innovations are defined as the difference between the sensor measurements and the predicted measurements, as described by equation 22. For a converged EKF, the innovation sequences should follow a zero centred Gaussian distribution. Figure 9 depicts the histogram distributions of ventral flow and divergence measurement innovations. It can be visually verified that the histogram distributions resemble a Gaussian distribution. To analytically verify this observation, we used the Kolmogorov-Smirnov test (KS test) [38] of normality. The KS test, examines the null hypothesis that the distribution of data in a particular series is significantly similar to a Gaussian distribution. A significance level of $p = 0.05$ has been used to test the innovation sequences. For both, ventral flow and divergence measurement innovations, the KS test validated the null hypothesis with p-values 0.5292 and 0.4001 respectively, thus verifying the normality of the sequences. Further, the means of the innovations are calculated as: $6.25 \times 10^{-4} rad/s$ for ventral flow innovations and $-2.3 \times 10^{-3} s^{-1}$ for divergence innovations, verifying that the means of both the innovation sequences are close to zero. Thus, the innovation sequences follow zero centred Gaussian distribution suggesting that the EKF converges to its optimum state.

$$\boldsymbol{i}_{\boldsymbol{y}_m}(t) = \boldsymbol{y}_m(t) - \boldsymbol{h}(\hat{\boldsymbol{x}}(t, t-1), t) \tag{22}$$

Here, $\boldsymbol{y}_m(t)$ represents the measurements, $\boldsymbol{i}_{\boldsymbol{y}_m}(t)$ represents the measurement innovations and $\hat{\boldsymbol{x}}(t, t-1)$ represents the predicted state at time instant t.

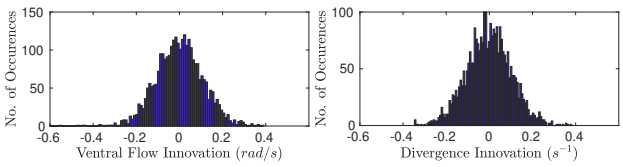

(a) (b)

Fig. 9: Histogram distribution of (a) ventral flow innovation values, mean $= 6.25 \times 10^{-4} rad/s$, KS-test p-value$= 0.5292$ and (b) divergence innovation values, mean $= -2.3 \times 10^{-3} s^{-1}$, KS-test p-value$= 0.4001$.

G. Attitude-Altitude Controller

The motivation behind investigating the optical flow based attitude estimator in this study is to finally use the estimated values to stabilize and control the orientation of an inherently unstable MAV. In most MAV applications, that use IMUs as the primary sensors to estimate attitude, the measurements are sampled at high frequencies ($\approx 200 - 500Hz$) to stabilize the MAV's dynamics. However, low frame rates associated with most available cameras, limit the efficiency an optical flow based controller. For instance, optical flow measurements are sampled from the bottom camera of a Bebop, using

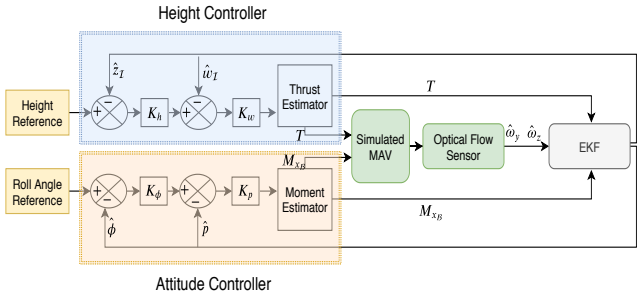

Fig. 10: Block diagram depicting the implementation of the attitude-altitude control loop.

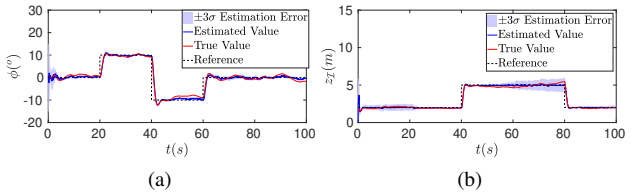

(a) (b)

Fig. 11: Performance of the attitude-altitude controller. Optical flow measurements are sampled at 30Hz. (a) Roll angle ϕ tracking performance, (b) Height $z_{\mathcal{I}}$ tracking performance.

Paparazzi vision pipeline (section IV-C), at a frequency of 30Hz. Thus, apart from verifying the convergence of the proposed estimator, it is important to analyse if the estimates are computed fast enough to stabilize the dynamics of a MAV.

A simple PD control loop, as depicted in figure 10, has been implemented in simulation to control the roll angle (ϕ) and height ($z_{\mathcal{I}}$) of the MAV. Step inputs in attitude and altitude reference are kept similar to as analysed in the previous subsections (figure 3). As has been done in this analysis so far, the mass and moment of inertia of the simulated MAV are kept the same as a Bebop 1 quadcopter. The noise and delay levels are kept the same as described in section III-F. We first analyse the scenario where the EKF runs at 500 Hz while the optical flow measurements are sampled at 30 Hz. Figure 11 depicts the controller's performance in tracking ϕ and $z_{\mathcal{I}}$ references. Despite the low sample rate, the controller is able to stabilize and control the dynamics of the simulated MAV.

It is interesting to observe the controller's performance when the MAV is in hover ($t \approx 0 - 20s$ and $t > 80s$). As discussed in the previous sub-sections, due to the lack of motion during hover, the observability remains low and the estimation error covariance increases. In presence of noise, this causes the estimates to diverge from the true state values. However, as the estimates diverge, the differences between the estimated states and reference inputs increase, which

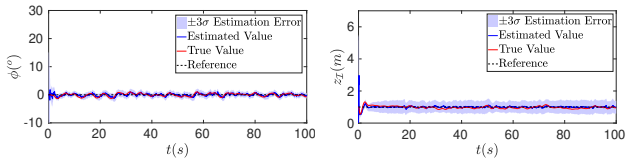

(a) (b)

Fig. 12: Performance of the attitude-altitude controller in maintaining the MAV at hover. The repeated excitation of the control inputs, retains system observability and causes small oscillations in the states of the MAV. (a) Roll angle ϕ tracking performance, (b) Height $z_{\mathcal{I}}$ tracking performance.

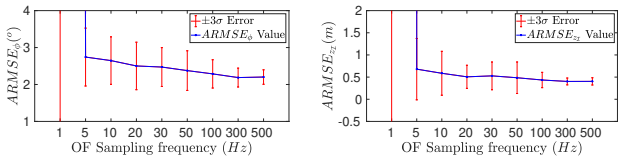

(a) (b)

Fig. 13: Average RMSE in (a) roll angle ϕ and (b) height $z_{\mathcal{I}}$ reference tracking for the simulated controller with the optical flow measurements sampled at different sampling frequencies. The ARMSE values are obtained over 50 simulation runs with different noise realizations. The red bars represent $\pm 3\sigma$ errors in the RMSE values. At $1Hz$ sampling frequency, the controller is unstable and hence the corresponding data points are out of bounds in the figures.

induces (bad) corrective actions through thrust and/or moment commands. This excitation in control inputs increases the observability of the system and hence the estimates converge again with the true state values. The convergence of the estimates leads to (good) corrective actions from the controller, which (re)stabilizes the flight. Therefore, in flight conditions with low motion of the MAV, the controller repeatedly excites the input commands with 'good' and 'bad' corrective actions. This leads to small oscillatory motion of the MAV. The phenomenon becomes more clear by observing the figure 12 where we analyse the controller's performance in maintaining the MAV at hover.

As discussed, the sample rate of the optical flow measurements plays a very important role in the controller's ability of stabilizing the MAV. To study the influence of measurement sample rate, we simulate the controller with the optical flow measurements sampled at various frequencies. ARMSE between the true MAV states and reference states has been chosen as the measure of controller's performance. In this analysis, the ARMSE corresponding to the state x is computed as described in equation 23. x_r represents the reference value of state x.

$$ARMSE_x = \frac{\sum_{k=1}^{k=N} \sqrt{\frac{\sum_{t=0}^{\tau}(x(t) - x_r(t))^2}{\tau}}}{N} \tag{23}$$

50 simulation runs have been performed for each sample rate, while keeping the noise and delays at the same level as described in section III-F. The obtained ARMSE values (with $\pm 3\sigma$ deviations in RMSE), in tracking ϕ and $z_{\mathcal{I}}$ references, are depicted in figures 13a and 13b respectively. We can conclude that the controller becomes unstable below 5Hz optical flow sampling frequency, while resulting in high values of reference tracking errors for sampling frequencies below 10Hz. For higher values of measurement sampling frequencies, the controller's performance improves.

In this section, we have designed an EKF based on the findings of the observability analysis, described in section II. The estimator has been tested in simulation and its performance in estimating the MAV's states has been verified. Further, a closed loop PD controller has been implemented that controls the attitude and altitude of the MAV using state estimates computed by the proposed estimator. In the following section, we verify the performance of the estimator in practice using flight data recorded on a flying robot.

IV. Verification through Experiments

In this section we verify the performance of the proposed estimator in practice on real flight data recorded on a Parrot Bebop quadcopter. The quadcopter is flown in a controlled environment to perform certain manoeuvres, as discussed in the following subsections. The estimator is run off-line, on logged flight data, to estimate the states of the MAV.

In this section, to measure the quality of measured/estimated values, we have used RMSE between the ground truth and the measured/estimated values of various quantities for single manoeuvres. Thus, instead of using the RMSE relation described in equation 21a, we use the following equation for calculating the RMSE between true value x and measured/estimated value $\hat{x}$ of a quantity x, over a manoeuvre of total duration τ:

$$RMSE_x = \sqrt{\frac{\sum_{t=0}^{\tau}(\hat{x}(t) - x(t))^2}{\tau}} \tag{24}$$

A. Experimental Setup

The experiments have been conducted indoors in a controlled flight arena called CyberZoo, at the faculty of Aerospace Engineering, Delft University of Technology. A Parrot Bebop quadcopter has been used as the MAV platform to verify the estimator. The MAV runs custom autopilot software designed using the open-source autopilot framework Paparazzi UAV[1]. A quaternion based PID inner control loop, available in Paparazzi, has been used to stabilize the attitude of the Bebop using ego-motion data from IMU. Further the outer control loop commands the position of the quadcopter inside

[1]Paparazzi UAV: http://wiki.paparazziuav.org/wiki/Main_Page

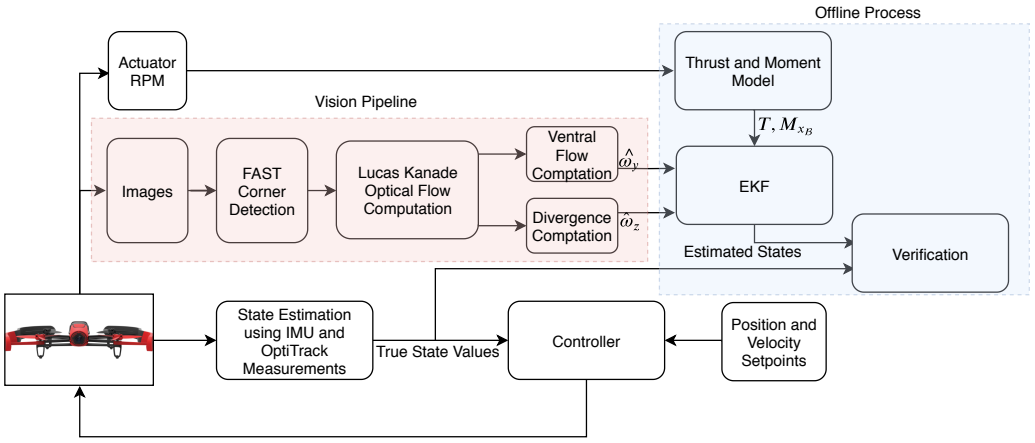

Fig. 14: Block diagram depicting the experimental verification procedure.

the CyberZoo, using position data from OptiTrack motion capture system. The bottom camera of the MAV has been used to record images which are processed to obtain the optical flow measurements, as discussed in section IV-C. To obtain accurate optical flow measurements, all flights are performed over a textured mat as visible in figure 15. Figure 14 depicts the experimental verification procedure adopted in this study.

Fig. 15: Bebop flying over a textured surface at CyberZoo during the experiments.

B. Thrust and Moment Model

The proposed estimator uses the knowledge about thrust T and moment $M_{x_\mathcal{B}}$ efference copies. The efference copies can be obtained from the control commands sent to the MAV's actuators or from the velocities of the actuators. There exists a time lag between the transmission of control commands to the motor mixing module, that computes the commands to be sent to individual motor speed controllers, and the generation of T and $M_{x_\mathcal{B}}$. This lag is expected to be less between the motors' rotational velocities and the generated T and $M_{x_\mathcal{B}}$. Thus, to reduce the effect of the time difference, T and $M_{x_\mathcal{B}}$ values are estimated from the rotor velocities using the linear model described in equation 25. The linear model is inspired from the reduced model of forces and moments [39], with the assumptions that the aerodynamic effects are negligible and the pitch and yaw rates remain small during the flight.

$$T = \kappa_1\Omega_1^2 + \kappa_2\Omega_2^2 + \kappa_3\Omega_3^2 + \kappa_4\Omega_4^2 \tag{25a}$$

$$M_{x_\mathcal{B}} = b(\kappa_1\Omega_1^2 - \kappa_2\Omega_2^2 - \kappa_3\Omega_3^2 + \kappa_4\Omega_4^2) \tag{25b}$$

b denotes the distance between MAV's CoG and motor axes, along the $Y_\mathcal{B}$ axis. Ω_i and parameter κ_i respectively denote the rotational speed and thrust coefficient of the ith rotor. We used a Weighted Least Squares (WLS) parameter estimation approach to compute the parameters κ_i, $i = 1, 2, 3, 4$, for the MAV used in the experiments. The equations corresponding to $M_{x_\mathcal{B}}$ are weighted 100 times more than the equations corresponding to T to compensate for the difference in scales of T and $M_{x_\mathcal{B}}$ values. A merged data set of individual manoeuvres performed by the MAV in response to reference step inputs in vertical velocity and roll angle has been used to fit the model. True values of T are computed by low-pass filtering and the (unscaled-unbiased) accelerometer measurements along the $Z_\mathcal{B}$ direction and multiplying the resulting values with m. Further, the true values of $M_{x_\mathcal{B}}$ are computed by differentiating the low pass filtered, (unscaled) gyroscope roll rate measurements and multiplying the resulting values with $I_{x_\mathcal{B}}$. Table V lists values of the computed parameters, κ, and figure 16 depicts the performance of the computed model in estimating the values of T and $M_{x_\mathcal{B}}$ for the same data-set which has used to fit the model. 81.11% prediction R^2 value was achieved for the T estimation model, however, the $M_{x_\mathcal{B}}$ estimation model performed poorly with R^2 value 12.41%.

Further investigating the moment model, we found that the unaccounted aerodynamic effects significantly affect the generated moments, even during low velocity manoeuvres. This inference is in accordance with the remark made in [40], where the authors have modelled the moments produced by aerodynamic effects on a Bepobop quadcopter. The derived model includes terms corresponding to the translational and

TABLE V: Estimated parameters of the thrust T and moment $M_{x_\mathcal{B}}$ model. The values of the obtained thrust coefficient parameters, κ, are listed in the units kgm.

κ_1	κ_2	κ_3	κ_4
1.49×10^{-6}	1.79×10^{-6}	1.21×10^{-6}	1.40×10^{-6}

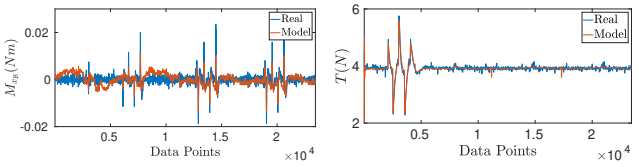

(a) (b)

Fig. 16: Estimation performance of the thrust and moment model on the estimation data-set. (a) Moment $M_{x_\mathcal{B}}$ estimation. Estimation $R^2 = 12.41\%$ (b) Thrust T estimation. Estimation $R^2 = 81.11\%$.

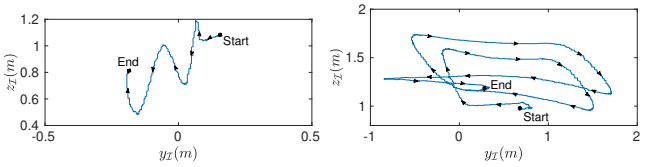

(a) (b)

Fig. 17: Trajectory followed by the MAV in $Y_\mathcal{I} - Z_\mathcal{I}$ plane during the maneuveres (a)$\mathcal{M}_1$ and (b)$\mathcal{M}_2$.

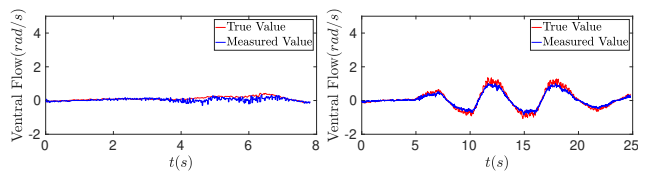

(a) (b)

Fig. 18: Ventral flow $\hat{\omega}_y$ measurements computed during the manoeuvres $\mathcal{M}_1$ and $\mathcal{M}_2$. The 'True Value' of $\hat{\omega}_y$ has been computed by substituting the values of the state estimates, obtained using the IMU and OptiTrack measurements, into equation 17b. (a) $\hat{\omega}_y$ measurements during manoeuvre $\mathcal{M}_1$. (b) $\hat{\omega}_y$ measurements during manoeuvre $\mathcal{M}_2$.

rotational velocities of the MAV. However, since we intend to not use any sensory information other than optical flow measurements, we do not have direct access to the values of these states. This poses a 'chicken and egg' problem, where we require the values of the moments to estimate the motion states of the MAV and need the values of the same motion states to estimate the values of the moments.

This deficiency of our estimator remains unsolved in the scope of the current investigation and we intend to tackle it in the future studies. To validate the feasibility of the proposed estimator, we consider manoeuvres where the applied moments on the quadcopter remain small and hence can be approximated as zero. We thus use only the values estimated by the thrust model as input to the EKF. The first considered manoeuvre, $\mathcal{M}_1$, is where the quadcopter responds to vertical velocity reference step inputs, while maintaining its horizontal position and orientation. Figure 17a depicts the trajectory followed by the Bebop in the $Y_\mathcal{I} Z_\mathcal{I}$ plane. In the second manoeuvre, $\mathcal{M}_2$, the quadcopter is given position set-points to move in an approximate vertical rectangular trajectory, as depicted in figure 17b. Note, that in $\mathcal{M}_2$, to move horizontally, the MAV has to change its roll angle, and thus the actual moments being applied are higher than in $\mathcal{M}_1$. On the other hand, in $\mathcal{M}_1$, though the moment values remain low, the MAV only moves vertically, thus measuring low ventral flow values (with high errors). As we will discuss in section IV-D, despite these discrepancies, the estimator converges and is able to calculate the state estimates with good levels of accuracy for the considered manoeuvres.

C. Optical Flow Computation

The image processing pipeline used to obtain the optical flow measurements from the images captured through the bottom camera of the MAV is depicted in figure 14. Maximally 25 corners are detected in each 240×240 image utilizing the Features from Accelerated Segment Test (FAST) corner tracking algorithm [41][42], and these features are tracked to the next image using the Lucas-Kanade optical flow algorithm [43]. Among the vectors computed by tracking the corners, the median vector is selected as global ventral flow, and its components are scaled, using the camera's intrinsic properties and the time difference between the two captured frames, to compute the ventral flow components in rad/s. Figure 18 depicts the measured $Y_\mathcal{I}$ ventral flow component ($y_{\hat{\omega}_y}$) for the manoeuvres $\mathcal{M}_1$ and $\mathcal{M}_2$. The ground truth in the figure has been computed by substituting the state estimates obtained from on-board IMU and OptiTrack measurements into equation 17b.

In Paparazzi, there are two different divergence computation algorithms available: Size Divergence [27] and Linear Flow Fit [44]. Here, we compare the measurements computed by both the methods, for the regime of the manoeuvres being considered in this study.

The Size Divergence method computes flow divergence by utilizing distances between the tracked corners in two subsequent images. 100 pairs of tracked corners are randomly sampled with replacement among all the possible pairs. Then, for each pair i, the distance between the corners in the previous image, $d_{(t-\Delta t),i}$ and the current image $d_{(t),i}$ are computed.

By calculating the ratio of $d_{(t-\Delta t),i} - d_{(t),i}$ to $d_{(t-\Delta t),i}$, the expansion and contraction of the flow is measured. To compute the global divergence, the average of these calculated ratios is taken. Further, using the time difference between the two subsequent images, the flow divergence in s^{-1} is computed. Equation 26 summarizes the method described here. N_p denotes the number of corner pairs sampled.

However, the Size Divergence algorithm has been derived with the assumption of the MAV moving in the vertical direction [27] and hence rotations and horizontal motion might induce discrepancies in the divergence measurements.

$$\hat{\omega}_z = \frac{1}{N_p}\sum_{i=1}^{N_p}\frac{1}{\Delta t}\left[\frac{d_{(t-\Delta t),i} - d_{(t),i}}{d_{(t-\Delta t),i}}\right] \tag{26}$$

The second vision algorithm, Linear Flow Fit, is based on the Longuet-Higgins and Prazdny mathematical model of optical flow [15], described in equation 1. The algorithm assumes that the flow vectors are de-rotated, and hence only contain information about the translational component of optical flow. With this assumption and neglecting the second order terms in $\hat{x}$ and $\hat{y}$, the equation 1 is modified and a linear model is approximated between the flow vectors and their pixel coordinates, as described by equation 27. The parameters of the linear model, $\boldsymbol{p_u} = [p_{u_1}, p_{u_2}, p_{u_3}]$ and $\boldsymbol{p_v} = [p_{v_1}, p_{v_2}, p_{v_3}]$, are estimated using a maximum likelihood linear least squares estimate within a robust RANdom SAmple Consensus (RANSAC) estimation technique [45].

$$\hat{u} = \boldsymbol{p_u}[1, \hat{x}, \hat{y}] = -\hat{\omega}_x + (\hat{\omega}_x\alpha + \hat{\omega}_z)\hat{x} + \hat{\omega}_x\beta\hat{y} \tag{27a}$$

$$\hat{u} = \boldsymbol{p_v}[1, \hat{x}, \hat{y}] = -\hat{\omega}_y + \hat{\omega}_y\alpha\hat{x} + (\hat{\omega}_y\beta + \hat{\omega}_z)\hat{y} \tag{27b}$$

α and β denote the gradients of the ground surface. Note, that since in this study we focus on flying over a flat textured surface without any inclination, $\alpha = 0$ and $\beta = 0$. The divergence can be obtained as:

$$\hat{\omega}_z = \frac{p_{u_2} + p_{v_3}}{2} \tag{28}$$

Note that the Linear Flow Fit method assumes the availability of de-rotated flow vectors. However, we use the raw flow vectors (including rotational component) for divergence computation, which might introduce errors in the calculated measurements. Since both the methods involve assumptions that are violated by the manoeuvres being considered in this study, the quality of measurements obtained by the two methods are compared. Figure 19 depicts the divergence measurements obtained, using the two described algorithms, during manoeuvres $\mathcal{M}_1$ and $\mathcal{M}_2$. The ground truth is calculated by substituting the state estimates, obtained from IMU and OptiTrack measurements, into equation 17b. It can be observed that the Size Divergence method results in higher number of outliers. Further, calculating the RMSE between the ground truth and the divergence measurements results in the values listed in table VI. Since, the Linear Flow Fit method results in relatively more accurate divergence measurements, it has been used to test the estimator's performance on real flight data, as described in section IV-D.

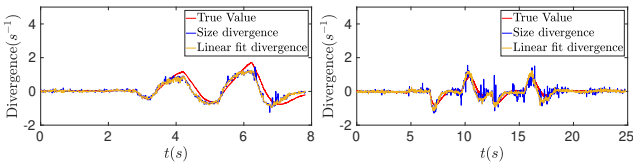

(a) (b)

Fig. 19: Divergence $\hat{\omega}_z$ measurements computed using the Size Divergence and Linear Flow Fit methods. The 'True Value' of $\hat{\omega}_z$ has been computed by substituting the values of state estimates, obtained using the IMU and OptiTrack measurements, into equation 17b. (a) $\hat{\omega}_z$ measurements during manoeuvre $\mathcal{M}_1$ (b) $\hat{\omega}_z$ measurements during manoeuvre $\mathcal{M}_2$.

TABLE VI: RMSE in optical flow measurements during the maneuveres $\mathcal{M}_1$ and $\mathcal{M}_2$. The RMSE values for the ventral flow measurements are in units rad/s and for the divergence measurements are in units s^{-1}.

Measurement	RMSE	
	Maneuvere $\mathcal{M}_1$	Maneuvere $\mathcal{M}_2$
Ventral Flow	0.14	0.15
Size Divergence	0.29	0.18
Linear Flow Fit Divergence	0.28	0.15

D. Estimation Results

In this subsection, we present the results obtained by testing the estimator against real flight data recorded on a Parrot Bebop quadcopter during the manoeuvres $\mathcal{M}_1$ and $\mathcal{M}_2$ depicted in figure 17. The state estimates have been compared with the true state values obtained from the on-board inertial sensors and the OptiTrack positioning system. During manoeuvre $\mathcal{M}_1$, the MAV translates in the vertical direction while maintaining its orientation and horizontal position. Thus, the MAV's roll angle (ϕ) remains close to zero and does not vary much. To verify the EKF's convergence, the initial state estimates provided to the estimator are set to be far from the true initial state values of the MAV. Table VII lists the initial state estimates provided to the EKF and the true initial values of the states during the manoeuvres $\mathcal{M}_1$ and $\mathcal{M}_2$.

As discussed in section IV-B, due to complex aerodynamic effects, we could not fit an accurate function for the calculation of moments using the rotor velocities. So, the manoeuvres $\mathcal{M}_1$ and $\mathcal{M}_2$ have been chosen such that the moment values remain low and thus are approximated to be zero. The EKF has been tuned to have high process noise variance corresponding to the state p. This has been done to decrease the estimator's

TABLE VII: Initial state estimates provided to the EKF and the true intial state values during the manoeuvres $\mathcal{M}_1$ and $\mathcal{M}_2$.

Initial State Values	EKF	$\mathcal{M}_1$	$\mathcal{M}_2$
$v_{\mathcal{I}}\ (m/s)$	2	0.01	0.11
$\phi\ (^o)$	10	0.11	0.25
$p\ (^o/s)$	10	-6.93	-1.76
$z_{\mathcal{I}}\ (m)$	2	1.10	0.97
$w_{\mathcal{I}}\ (m/s)$	2	-0.05	-0.01

confidence on the moment inputs, since the term containing moment only appears in the derivative equation of p (see equation 17a).

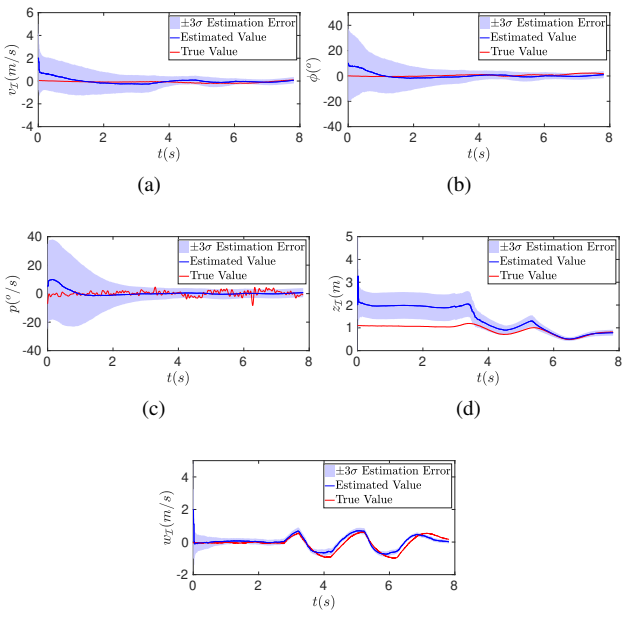

Fig. 20: Estimator's performance on real flight data recorded on a Bebop 1 quadcopter during manoeuvre $\mathcal{M}_1$. (a) Horizontal velocity $v_{\mathcal{I}}$, (b) roll angle ϕ, (c) roll rate p, (d) height $z_{\mathcal{I}}$ and (e) vertical velocity $w_{\mathcal{I}}$

Figures 20 and 21 depict the estimation results for manoeuvres $\mathcal{M}_1$ and $\mathcal{M}_2$ respectively. In $\mathcal{M}_1$, only the vertical motion states, $z_{\mathcal{I}}$ and $w_{\mathcal{I}}$ have been excited and hence the other states, including p, remain close to zero. Thus, approximating the moment values to be zero is an appropriate assumption. It can be observed that, even though the time interval of the manoeuvre considered is low ($\tau \approx 8s$), the estimates converge to their true values and the estimation error variances decrease. The RMSE between the true and estimated values of ϕ is computed to be 2.56^o, which is satisfactorily low considering the wrong initial estimate given to the EKF and the low time

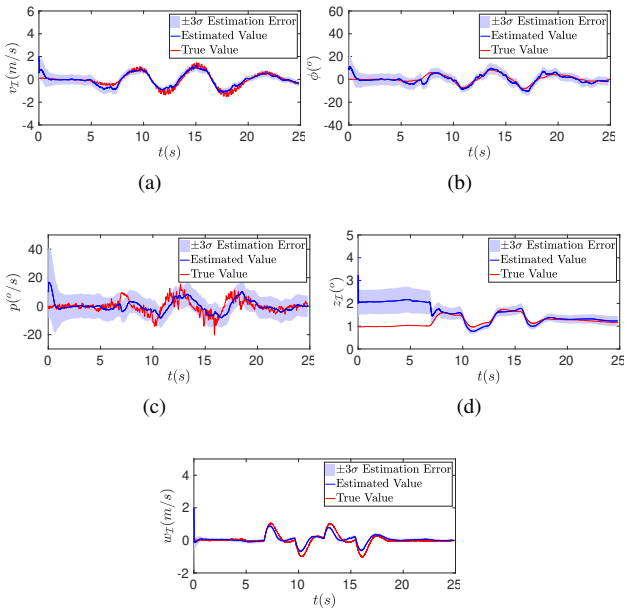

Fig. 21: Estimator's performance on real flight data recorded on a Bebop 1 quadcopter during manoeuvre $\mathcal{M}_2$. (a) Horizontal velocity $v_{\mathcal{I}}$, (b) roll angle ϕ, (c) roll rate p, (d) height $z_{\mathcal{I}}$ and (e) vertical velocity $w_{\mathcal{I}}$

duration of the manoeuvre.

However, in $\mathcal{M}_2$, the MAV also translates horizontally, due to which ϕ and p vary. Thus, significant values of moment act on the MAV. Despite setting the process noise variance corresponding to the state p at a high value, the discrepancy in the moment values input to the EKF affects the estimator's accuracy. As can be expected, the p estimates are affected the most. p estimation error variance remains high through-out the manoeuvre and a high RMSE value of $4.65^o/s$ is registered between the true and estimated state values of p. However, despite the zero moment inputs, the predicted values of p in the EKF are corrected using the optical flow observations and the variation trend in the estimated values of p matches the variation trend in the true p values, as depicted in figure 21c. The estimated values of the other states, including ϕ, converge to their true values and the estimation error variances reduce. Considering the discrepancies in the information provided to the EKF (moment model), reasonable attitude estimation accuracy is obtained, with RMSE between true and estimated values of ϕ being 2.12^o.

Through the results depicted in figure 20 and 21 we verify a proof of concept of the proposed optical flow based attitude estimator. Despite the deficiencies in the inputs and measurements provided to the estimator, it converges and provides state estimates with considerable accuracy. In the following section, we discuss various aspects and implications of the introduced approach and conclude the article.

V. Discussion

In this section we reflect on various aspects and implications of the optical flow based attitude estimation approach introduced in this article.

A. Moment Model

It is necessary that we remark upon the main deficiency in the presented work: the dependency on moment efference copies and the inability to estimate a model to accurately compute the moments.

As discussed in section III-E, accuracy of the attitude estimates is more sensitive to discrepancies in the moment inputs than the thrust inputs. Further, the low moment of inertia, associated with most MAVs, means that even small errors in the estimated moments translate into large errors in the predicted angular accelerations. The EKF only has two observations, to correct for these errors, neither of which provide a direct measure of the attitude or the rate of change of attitude. Thus, the estimator's accuracy critically depends on error-free knowledge of the moment inputs.

On a Bebop, moment generation is significantly affected by the aerodynamic effects due to translational motion, even in relatively slow flights [40]. Thus, fitting a model to estimate the moments using only the rotor velocities (or the control commands) is difficult. As, the moments are being augmented by translational and rotational velocities, ideally terms corresponding to these velocities should also be used to calculate the moment. However, in this investigation we have conditioned ourselves to use optical flow measurements as the only sensory information, we cannot use additional sensors to measure the velocities. This poses a 'chicken and egg' problem where we need the values of moments to estimate the velocities and on the other hand, we need the values of the velocities to estimate the moments.

For applicability of the approach in real robots, it is necessary to find a solution to this 'chicken and egg' problem. In future studies, we intend to utilize advanced model fitting methods to fit the moment estimation function. Another viable solution might be to accommodate the aerodynamic terms in the estimator's motion model. The proposed solution can be summarized through the following equations:

$$\frac{d}{dt}p = \frac{M}{I_{x_\mathcal{B}}} \tag{29a}$$

$$M = f(\Omega_1, \Omega_2, \Omega_3, \Omega_4, v_\mathcal{I}, w_\mathcal{I}, p) \tag{29b}$$

Here, we propose that the roll rate, p, derivative relation in equation 17a be replaced by equation 29a. Thus, instead of directly using $M_{x_\mathcal{B}}$ as an input to the model, we augment the motion model by including a non-linear function of moment estimation, M, that depends on the rotor speeds and the MAV's velocities. Similarly, a non-linear function for thrust estimation can also be modelled which would then replace the thrust, T, terms in the motion model. For instance, the aerodynamic model derived in [40] can be used as the said non-linear functions. The new system would take the rotor velocities as inputs instead of the thrust and moment values. However, the change in the motion model would augment the observability relations. The implications of the proposed strategy, of estimating moments, on the system's observability remains to be investigated in future studies.

B. Control of a Tailless Flapping Wing MAV: DelFly Nimble

The attitude estimation approach introduced in this article uses optical flow measurements from a monocular camera as the only sensory information and thus provides a very attractive solution for miniaturization of MAVs. For tiny flying robots, like DelFly Nimble [1], Robobee [46], or tiny quadrotor pocket drones [47], every sensor setup is a significant payload. Thus the proposed optical flow based state estimation strategy is highly relevant for such MAVs. The approach might even be essential for inherently unstable FWMAVs, like the DelFly Nimble, that require active ego-motion estimation and stabilization. In future studies, we intend to implement the proposed attitude estimation approach for flight stabilization and control of the Nimble. In this subsection, we present a preliminary analysis on the feasibility of the proposed approach for flight control of a DelFly Nimble.

The flight dynamics of the Nimble is complicated. Thus for this preliminary analysis, we use the same MAV model as has been used so far in this investigation, with the mass and moment of inertia of the simulated MAV set equal to that of the Nimble. An attitude-altitude controller, as discussed in section III-G, has been implemented to control the height and roll angle of the MAV. The Nimble, with mass of $0.029kg$ and inertia of $1.26 \times 10^{-4} kgm^2$ about its $Y_\mathcal{B}$ axis [48], has approximately 10 times less mass and inertia as compared to a Bebop quadcopter. Thus, it can be expected to be more sensitive to noise and delays in the inputs and measurements. Note that since we simulate the roll dynamics of the MAV, we have used the Nimble's inertia about $Y_\mathcal{B}$ axis as the simulated MAV's inertia about $X_\mathcal{B}$ axis. Further, the 4g stereovision system, Stereoboard [49], has been modified into a monocular setup which is lightweight enough to be carried on a Nimble. The monocam setup has a frame rate of about 30Hz and thus we simulate the controller with the optical flow measurements being sampled at 30Hz and the EKF running at 500Hz. For this analysis, the delays in all the inputs and measurements and the noise in the measurements are kept the same as described in section III-F. However, having 10 times less mass and inertia, we set the noise values in thrust and moments to be 10 times the values used in section III-F, thus keeping the noise, in vertical acceleration and angular acceleration, of the same order as previously considered. The simulated MAV has been given the same reference attitude and height to track as used in III-G (refer figure 3).

As expected, we observed that the simulated MAV controller is more sensitive to the noise and delays in the inputs, and thus the EKF has been tuned to have higher values of process noise variances corresponding to the states $w_\mathcal{I}$ and p. Figure 22 depicts the results obtained by simulating the controller.

Though the controller struggles to track the reference states and the MAV oscillates, the system does-not become unstable and the reference trajectory is approximately tracked

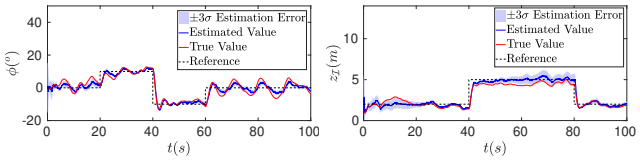

(a) (b)

Fig. 22: Performance of the attitude-altitude controller on a MAV model with mass and inertia representing a DelFly Nimble. (a) Roll angle ϕ tracking performance, (b) Height $z_{\mathcal{I}}$ tracking performance.

though with high errors. Therefore, the preliminary analysis establishes that it is feasible to use the introduced approach for flight stabilization of a MAV of the scale of Nimble. However, being a FWMAV, the Nimble's body experiences considerably more oscillations and disturbances as compared to a Bebop. Thus the optical flow readings as well as the efference copy inputs can be expected to be more noisy. Given the sensitivity of the simulated system to noise and the poor performance of the controller in the scenario studied (figure 22), in practice it might be necessary to sample the optical flow measurements at a higher frame rate. However, only a few available cameras, like the Curved Artificial Compound Eyes (CURVACE) [50], have high frame rates and are light enough to be used on the Nimble. In future investigations, we will consider implementing the approach presented in this article on a Nimble using a suitable camera.

C. Implications for Insect Flight

Various theories of insect flight suggest that insects employ visuo-motor control strategies to perform various navigation tasks [4], thus using optical flow measurables directly in a control loop, without estimating the absolute values of their states. However, there are evidences suggesting that the insects might be able to estimate the absolute values of their states [25][24]. Some approaches have been developed that hypothesize how the insects can estimate their velocities [28] and distances [24][26] using optical flow and control efference copies. However, to the best of our knowledge, the strategies used by insects for optical flow based estimation of orientation is largely un-explained. Our findings form a novel hypothesis about how some flying insects can estimate their states, including attitude, using optical flow as the prominent sensory information.

In our analysis, we showed that while maintaining the MAV in hover with the attitude-altitude control strategy (section III-G), the thrust and moment control inputs are repeatedly excited with 'good' and 'bad' corrective actions. This causes the MAV to perform small oscillations. It will be an interesting case to investigate whether similar oscillations are also found in hovering insects. If these oscillations are indeed found to be performed by the insects, it can then be hypothesized that the oscillations play a more critical role in the flight stability of insects that do not have halteres (and thus prominently depend on optical flow for flight stabilization), than in insects that possess the said rotational rate sensing organs. Experimentally studying and comparing the hovering flight characteristics of the two kinds of insects would test the stated hypothesis and further help elucidate the flight control strategies employed by insects.

VI. Conclusions

In this article, we have proposed a novel bio-inspired state estimation technique that uses optical flow measurements (as the only sensory information) and the knowledge of control efference copies to estimate the roll attitude, roll rate, height, horizontal and vertical velocities of a MAV flying over a flat textured surface with three degrees of freedom (3-DoF). We used non-linear observability analysis to mathematically prove the feasibility of estimating orientation of a MAV using optical flow measurements. This analysis has been verified in simulations. A closed loop attitude-altitude controller based on the proposed estimator has been shown to be capable of stabilizing the flight of a MAV. Further, we verified a proof of concept of the estimator by demonstrating its performance on flight data of a real robotic platform. In future investigations, we intend to devise a more effective strategy of estimating the values of the efference inputs and incorporate it with the estimator. Further, we will implement the proposed approach to estimate and stabilize the flight of a MAV in real-time.

The findings of this study propose a promising technique for miniaturization of MAVs and provide a novel hypothesis about optical flow based attitude estimation strategies used by the insects. Thus this study brings us a small step closer towards making MAVs as nimble as the insects.

References

[1] M. Karásek, F. T. Muijres, C. De Wagter, B. D. Remes, and G. C. de Croon, "A tailless aerial robotic flapper reveals that flies use torque coupling in rapid banked turns," *Science*, vol. 361, no. 6407, pp. 1089–1094, 2018.

[2] N. M. Barbour, "Inertial navigation sensors," Charles Stark Draper Lab Inc Cambridge Ma, Tech. Rep., 2010.

[3] G. K. Taylor and H. G. Krapp, "Sensory systems and flight stability: what do insects measure and why?" *Advances in insect physiology*, vol. 34, pp. 231–316, 2007.

[4] M. V. Srinivasan, "Honeybees as a model for the study of visually guided flight, navigation, and biologically inspired robotics," *Physiological reviews*, vol. 91, no. 2, pp. 413–460, 2011.

[5] W. Shyy, C.-k. Kang, P. Chirarattananon, S. Ravi, and H. Liu, "Aerodynamics, sensing and control of insect-scale flapping-wing flight," *Proceedings of the Royal Society A: Mathematical, Physical and Engineering Sciences*, vol. 472, no. 2186, p. 20150712, 2016.

[6] W. Kirchner and M. Srinivasan, "Freely flying honeybees use image motion to estimate object distance," *Naturwissenschaften*, vol. 76, no. 6, pp. 281–282, 1989.

[7] C. T. David, "Compensation for height in the control of groundspeed bydrosophila in a new,barber's polewind tunnel," *Journal of Comparative Physiology A: Neuroethology, Sensory, Neural, and Behavioral Physiology*, vol. 147, no. 4, pp. 485–493, 1982.

[8] M. Srinivasan, S. Zhang, M. Lehrer, and T. Collett, "Honeybee navigation en route to the goal: visual flight control and odometry," *Journal of Experimental Biology*, vol. 199, no. 1, pp. 237–244, 1996.

[9] G. Portelli, F. Ruffier, F. L. Roubieu, and N. Franceschini, "Honeybees' speed depends on dorsal as well as lateral, ventral and frontal optic flows," *PloS one*, vol. 6, no. 5, p. e19486, 2011.

[10] G. Portelli, J. R. Serres, and F. Ruffier, "Altitude control in honeybees: joint vision-based learning and guidance," *Scientific reports*, vol. 7, no. 1, p. 9231, 2017.

[11] E. Baird, M. V. Srinivasan, S. Zhang, R. Lamont, and A. Cowling, "Visual control of flight speed and height in the honeybee," in *International Conference on Simulation of Adaptive Behavior*. Springer, 2006, pp. 40–51.

[12] M. V. Srinivasan, S.-W. Zhang, J. S. Chahl, E. Barth, and S. Venkatesh, "How honeybees make grazing landings on flat surfaces," *Biological cybernetics*, vol. 83, no. 3, pp. 171–183, 2000.

[13] E. Baird, N. Boeddeker, M. R. Ibbotson, and M. V. Srinivasan, "A universal strategy for visually guided landing," *Proceedings of the National Academy of Sciences*, vol. 110, no. 46, pp. 18 686–18 691, 2013.

[14] R. Goulard, J.-L. Vercher, and S. Viollet, "To crash or not to crash: how do hoverflies cope with free-fall situations and weightlessness?" *Journal of Experimental Biology*, vol. 219, no. 16, pp. 2497–2503, 2016.

[15] H. C. Longuet-Higgins and K. Prazdny, "The interpretation of a moving retinal image," *Proceedings of the Royal Society of London. Series B. Biological Sciences*, vol. 208, no. 1173, pp. 385–397, 1980.

[16] A. Santamaria-Navarro, J. Sola, and J. Andrade-Cetto, "High-frequency mav state estimation using low-cost inertial and optical flow measurement units," in *2015 IEEE/RSJ International Conference on Intelligent Robots and Systems (IROS)*. IEEE, 2015, pp. 1864–1871.

[17] V. Grabe, H. H. Bülthoff, and P. R. Giordano, "A comparison of scale estimation schemes for a quadrotor uav based on optical flow and imu measurements," in *2013 IEEE/RSJ international conference on intelligent robots and systems*. IEEE, 2013, pp. 5193–5200.

[18] K. McGuire, G. De Croon, C. De Wagter, K. Tuyls, and H. Kappen, "Efficient optical flow and stereo vision for velocity estimation and obstacle avoidance on an autonomous pocket drone," *IEEE Robotics and Automation Letters*, vol. 2, no. 2, pp. 1070–1076, 2017.

[19] W. E. Green, P. Y. Oh, and G. Barrows, "Flying insect inspired vision for autonomous aerial robot maneuvers in near-earth environments," in *IEEE International Conference on Robotics and Automation, 2004. Proceedings. ICRA'04. 2004*, vol. 3. IEEE, 2004, pp. 2347–2352.

[20] J.-C. Zufferey and D. Floreano, "Fly-inspired visual steering of an ultralight indoor aircraft," *IEEE Transactions on Robotics*, vol. 22, no. 1, pp. 137–146, 2006.

[21] R. J. Moore, K. Dantu, G. L. Barrows, and R. Nagpal, "Autonomous mav guidance with a lightweight omnidirectional vision sensor," in *2014 IEEE International Conference on Robotics and Automation (ICRA)*. IEEE, 2014, pp. 3856–3861.

[22] F. Expert and F. Ruffier, "Flying over uneven moving terrain based on optic-flow cues without any need for reference frames or accelerometers," *Bioinspiration & biomimetics*, vol. 10, no. 2, p. 026003, 2015.

[23] J. Goosen, "Design aspects of a bio-inspired flying sensor node," in *SENSORS, 2012 IEEE*. IEEE, 2012, pp. 1–4.

[24] F. Van Breugel, K. Morgansen, and M. H. Dickinson, "Monocular distance estimation from optic flow during active landing maneuvers," *Bioinspiration & biomimetics*, vol. 9, no. 2, p. 025002, 2014.

[25] R. Goulard, J.-L. Vercher, and S. Viollet, "Modeling visual-based pitch, lift and speed control strategies in hoverflies," *PLoS computational biology*, vol. 14, no. 1, p. e1005894, 2018.

[26] G. C. de Croon, "Monocular distance estimation with optical flow maneuvers and efference copies: a stability-based strategy," *Bioinspiration & biomimetics*, vol. 11, no. 1, p. 016004, 2016.

[27] H. Ho, G. de Croon, E. Van Kampen, Q. Chu, and M. Mulder, "Adaptive control strategy for constant optical flow divergence landing," *arXiv preprint arXiv:1609.06767*, 2016.

[28] H. W. Ho, G. C. de Croon, and Q. Chu, "Distance and velocity estimation using optical flow from a monocular camera," *International Journal of Micro Air Vehicles*, vol. 9, no. 3, pp. 198–208, 2017.

[29] R. Hermann and A. Krener, "Nonlinear controllability and observability," *IEEE Transactions on automatic control*, vol. 22, no. 5, pp. 728–740, 1977.

[30] G. J. Olsder and J. Van der Woude, *Mathematical systems theory*. VSSD Delft, 2005.

[31] A. J. Krener and K. Ide, "Measures of unobservability," in *Proceedings of the 48h IEEE Conference on Decision and Control (CDC) held jointly with 2009 28th Chinese Control Conference*. IEEE, 2009, pp. 6401–6406.

[32] F. Arrichiello, G. Antonelli, A. Aguiar, and A. Pascoal, "An observability metric for underwater vehicle localization using range measurements," *Sensors*, vol. 13, no. 12, pp. 16 191–16 215, 2013.

[33] B. T. Hinson and K. A. Morgansen, "Flowfield estimation in the wake of a pitching and heaving airfoil," in *2012 American Control Conference (ACC)*. IEEE, 2012, pp. 1085–1091.

[34] S. F. Schmidt, "The kalman filter-its recognition and development for aerospace applications," *Journal of Guidance, Control, and Dynamics*, vol. 4, no. 1, pp. 4–7, 1981.

[35] X. R. Li and Z. Zhao, "Measures of performance for evaluation of estimators and filters," in *Signal and Data Processing of Small Targets 2001*, vol. 4473. International Society for Optics and Photonics, 2001, pp. 530–541.

[36] J. Havlík and O. Straka, "Performance evaluation of iterated extended kalman filter with variable step-length," in *Journal of Physics: Conference Series*, vol. 659, no. 1. IOP Publishing, 2015, p. 012022.

[37] A. Toloei and S. Niazi, "State estimation for target tracking problems with nonlinear kalman filter algorithms," *International Journal of Computer Applications*, vol. 98, no. 17, 2014.

[38] H. W. Lilliefors, "On the kolmogorov-smirnov test for normality with mean and variance unknown," *Journal of the American statistical Association*, vol. 62, no. 318, pp. 399–402, 1967.

[39] R. Mahony, V. Kumar, and P. Corke, "Multirotor aerial vehicles: Modeling, estimation, and control of quadrotor," *IEEE robotics & automation magazine*, vol. 19, no. 3, pp. 20–32, 2012.

[40] S. Sun, R. Schilder, and C. C. de Visser, "Identification of quadrotor aerodynamic model from high speed flight data," in *2018 AIAA Atmospheric Flight Mechanics Conference*, 2018, p. 0523.

[41] E. Rosten and T. Drummond, "Fusing points and lines for high performance tracking," in *ICCV*, vol. 2. Citeseer, 2005, pp. 1508–1515.

[42] E. Rosten and T. Drummond, "Machine learning for high-speed corner detection," in *European conference on computer vision*. Springer, 2006, pp. 430–443.

[43] B. D. Lucas, T. Kanade *et al.*, "An iterative image registration technique with an application to stereo vision," 1981.

[44] G. De Croon, H. Ho, C. De Wagter, E. Van Kampen, B. Remes, and Q. Chu, "Optic-flow based slope estimation for autonomous landing," *International Journal of Micro Air Vehicles*, vol. 5, no. 4, pp. 287–297, 2013.

[45] M. A. Fischler and R. C. Bolles, "Random sample consensus: a paradigm for model fitting with applications to image analysis and automated cartography," *Communications of the ACM*, vol. 24, no. 6, pp. 381–395, 1981.

[46] K. Y. Ma, P. Chirarattananon, S. B. Fuller, and R. J. Wood, "Controlled flight of a biologically inspired, insect-scale robot," *Science*, vol. 340, no. 6132, pp. 603–607, 2013.

[47] O. Dunkley, J. Engel, J. Sturm, and D. Cremers, "Visual-inertial navigation for a camera-equipped 25g nano-quadrotor," in *IROS2014 aerial open source robotics workshop*, 2014, p. 2.

[48] K. M. Kajak, M. Karásek, Q. P. Chu, and G. de Croon, "A minimal longitudinal dynamic model of a tailless flapping wing robot for control design," *Bioinspiration & biomimetics*, 2019.

[49] C. De Wagter, S. Tijmons, B. D. Remes, and G. C. de Croon, "Autonomous flight of a 20-gram flapping wing mav with a 4-gram onboard stereo vision system," in *Robotics and Automation (ICRA), 2014 IEEE International Conference on*. IEEE, 2014, pp. 4982–4987.

[50] S. Viollet, S. Godiot, R. Leitel, W. Buss, P. Breugnon, M. Menouni, R. Juston, F. Expert, F. Colonnier, G. L'Eplattenier *et al.*, "Hardware architecture and cutting-edge assembly process of a tiny curved compound eye," *Sensors*, vol. 14, no. 11, pp. 21 702–21 721, 2014.

APPENDIX A
OBSERVABILITY ANALYSIS: VARYING ATTITUDE CONSTANT ALTITUDE CASE

For brevity, all the expressions involved in the observability analysis, for various scenarios, have not been included in the main article. Instead, the observability analysis derivations are being presented in the following appendices for reader's reference.

In this appendix, we present the observability analysis for the case: 'varying attitude, constant altitude', as described in section II-D, equation 9. Following equations describe the system being considered for observability analysis:

$$\boldsymbol{f}(\boldsymbol{x},t) = \frac{d}{dt}\begin{bmatrix} v_{\mathcal{I}} \\ \phi \\ p \\ z_{\mathcal{I}} \end{bmatrix} = \begin{bmatrix} gtan\phi \\ p \\ M_{x_{\mathcal{B}}}/I_{x_{\mathcal{B}}} \\ 0 \end{bmatrix} \tag{30a}$$

$$y_{\hat{\omega}_y} = \frac{-v_{\mathcal{I}}cos^2\phi}{z_{\mathcal{I}}} + p \tag{30b}$$

There are four states to be estimated, thus the observability matrix needs to have minimum four independent rows. Therefore, we consider the Lie derivatives up-to the third order of the ventral flow observation. The Lie derivatives can be computed as follows:

$$\mathcal{L}_f^0 y_{\hat{\omega}_y} = \frac{-v_{\mathcal{I}}cos^2\phi}{z_{\mathcal{I}}} + p \tag{31a}$$

$$\mathcal{L}_f^1 y_{\hat{\omega}_y} = \frac{M_{x_{\mathcal{B}}} z_{\mathcal{I}} - (I_{x_{\mathcal{B}}} gsin(2\phi))/2 + I_{x_{\mathcal{B}}} pv_{\mathcal{I}} sin(2\phi)}{I_{x_{\mathcal{B}}} z_{\mathcal{I}}} \tag{31b}$$

$$\mathcal{L}_f^2 y_{\hat{\omega}_y} = \frac{M_{x_{\mathcal{B}}} v_{\mathcal{I}} sin(2\phi) + I_{x_{\mathcal{B}}} gp + 2I_{x_{\mathcal{B}}} p^2 v_{\mathcal{I}} cos(2\phi) - 2I_{x_{\mathcal{B}}} gpcos(2\phi)}{I_{x_{\mathcal{B}}} z_{\mathcal{I}}} \tag{31c}$$

$$\begin{aligned} \mathcal{L}_f^3 y_{\hat{\omega}_y} = \; & -[\frac{6M_{x_{\mathcal{B}}} gcos^3(\phi) - 5M_{x_{\mathcal{B}}} gcos(\phi) + 6M_{x_{\mathcal{B}}} pv_{\mathcal{I}} cos(\phi) + 2I_{x_{\mathcal{B}}} gp^2 sin(\phi)}{I_{x_{\mathcal{B}}} z_{\mathcal{I}} cos(\phi)} + \\ & \frac{-12M_{x_{\mathcal{B}}} pv_{\mathcal{I}} cos^3(\phi) + 8I_{x_{\mathcal{B}}} p^3 v_{\mathcal{I}} cos^2(\phi) sin(\phi) - 12I_{x_{\mathcal{B}}} gp^2 cos^2(\phi) sin(\phi)}{I_{x_{\mathcal{B}}} z_{\mathcal{I}} cos(\phi)}] \end{aligned} \tag{31d}$$

Computing the Jacobian of the Lie derivatives, we obtain the following elements of the observability matrix.

$$\mathcal{O}_1 = \left\{ \frac{-cos^2(\phi)}{z_{\mathcal{I}}} \quad \frac{v_{\mathcal{I}} sin(2\phi)}{z_{\mathcal{I}}} \quad 1 \quad \frac{v_{\mathcal{I}} cos^2(\phi)}{z_{\mathcal{I}}^2} \right\} \tag{32a}$$

$$\mathcal{O}_2 = \left\{ \frac{psin(2\phi)}{z_{\mathcal{I}}} \quad \frac{-cos(2\phi)(g - 2pv_{\mathcal{I}})}{z_{\mathcal{I}}} \quad \frac{(v_{\mathcal{I}} sin(2\phi))}{z_{\mathcal{I}}} \quad \frac{sin(2\phi)(g - 2pv_{\mathcal{I}})}{2z_{\mathcal{I}}^2} \right\} \tag{32b}$$

$$\mathcal{O}_{3,1} = \frac{(2I_{x_{\mathcal{B}}} cos(2\phi)p^2 + M_{x_{\mathcal{B}}} sin(2\phi))}{I_{x_{\mathcal{B}}} z_{\mathcal{I}}} \tag{32c}$$

$$\mathcal{O}_{3,2} = \frac{-4I_{x_{\mathcal{B}}} v_{\mathcal{I}} sin(2\phi)p^2 + 4I_{x_{\mathcal{B}}} gsin(2\phi)p + 2M_{x_{\mathcal{B}}} v_{\mathcal{I}} cos(2\phi)}{I_{x_{\mathcal{B}}} z_{\mathcal{I}}} \tag{32d}$$

$$\mathcal{O}_{3,3} = \frac{(g - 2gcos(2\phi) + 4pv_{\mathcal{I}} cos(2\phi))}{z_{\mathcal{I}}} \tag{32e}$$

$$\mathcal{O}_{3,4} = \frac{-(M_{x_{\mathcal{B}}} v_{\mathcal{I}} sin(2\phi) + I_{x_{\mathcal{B}}} gp + 2I_{x_{\mathcal{B}}} p^2 v_{\mathcal{I}} cos(2\phi) - 2I_{x_{\mathcal{B}}} gpcos(2\phi))}{(I_{x_{\mathcal{B}}} z_{\mathcal{I}}^2)} \tag{32f}$$

$$\mathcal{O}_{4,1} = \frac{(-4I_{x_{\mathcal{B}}} sin(2\phi)p^3 + 6M_{x_{\mathcal{B}}} cos(2\phi)p)}{(I_{x_{\mathcal{B}}} z_{\mathcal{I}})} \tag{32g}$$

$$\begin{aligned} \mathcal{O}_{4,2} = \; & -[\frac{2I_{x_{\mathcal{B}}} gp^2 + 12I_{x_{\mathcal{B}}} gp^2 cos^2(\phi) - 24I_{x_{\mathcal{B}}} gp^2 cos^4(\phi) - 8I_{x_{\mathcal{B}}} p^3 v_{\mathcal{I}} cos^2(\phi)}{(I_{x_{\mathcal{B}}} z_{\mathcal{I}} cos^2(\phi))} + \\ & \frac{16I_{x_{\mathcal{B}}} p^3 v_{\mathcal{I}} cos^4(\phi) - 12M_{x_{\mathcal{B}}} gcos^3(\phi) sin(\phi) + 24M_{x_{\mathcal{B}}} pv_{\mathcal{I}} cos^3(\phi) sin(\phi)}{(I_{x_{\mathcal{B}}} z_{\mathcal{I}} cos^2(\phi))}] \end{aligned} \tag{32h}$$

$$\mathcal{O}_{4,3} = \; -\frac{(6M_{x_{\mathcal{B}}} v_{\mathcal{I}} cos(\phi) - 12M_{x_{\mathcal{B}}} v_{\mathcal{I}} cos^3(phi) + 4I_{x_{\mathcal{B}}} gpsin(\phi) + 24I_{x_{\mathcal{B}}} p^2 v_{\mathcal{I}} cos^2(\phi) sin(\phi) - 24I_{x_{\mathcal{B}}} gpcos^2(phi) sin(\phi))}{I_{x_{\mathcal{B}}} z_{\mathcal{I}} cos(\phi)} \tag{32i}$$

$$\mathcal{O}_{4,4} = [\frac{6M_{x_\mathcal{B}}gcos^3(\phi) - 5M_{x_\mathcal{B}}gcos(\phi) + 6M_{x_\mathcal{B}}pv_\mathcal{I}cos(\phi) + 2I_{x_\mathcal{B}}gp^2sin(\phi)}{I_{x_\mathcal{B}}z_\mathcal{I}^2cos(\phi)} + \frac{-12M_{x_\mathcal{B}}pv_\mathcal{I}cos^3(\phi) + 8I_{x_\mathcal{B}}p^3v_\mathcal{I}cos^2(\phi)sin(\phi) - 12I_{x_\mathcal{B}}gp^2cos^2(\phi)sin(\phi)}{I_{x_\mathcal{B}}z_\mathcal{I}^2cos(\phi)}] \tag{32j}$$

Note, that some elements of the Jacobian are too large to be represented in a matrix. Thus for the clarity of representation, we have split the observability matrix into row vectors (equations 32a and32b) and individual elements (equations 32c to 32j). The term $\mathcal{O}_{i,j}$ refers to the element at i^{th} row and j^{th} column of the observability matrix $\mathcal{O}$. Similar notation style has been used in the following appendices as well.

From the computed elements of the observability matrix, it can be inferred that the observability matrix is full rank. Thus the system represented by equation 9 is locally weakly observable.

APPENDIX B
OBSERVABILITY ANALYSIS OF CONSTANT ATTITUDE VARYING ALTITUDE CASE

In this appendix, we derive the observability analysis for the 'constant attitude, varying altitude case' as discussed in section II-E. The system equations (equation 13) can be restated as follows:

$$\boldsymbol{f}(\boldsymbol{x},t) = \frac{d}{dt}\begin{bmatrix} v_{\mathcal{I}} \\ \phi \\ z_{\mathcal{I}} \\ w_{\mathcal{I}} \end{bmatrix} = \begin{bmatrix} Tsin\phi/m \\ 0 \\ w_{\mathcal{I}} \\ Tcos\phi/m - g \end{bmatrix} \tag{33a}$$

$$y_{\hat{\omega}_y} = \frac{-v_{\mathcal{I}}cos^2\phi}{z_{\mathcal{I}}} + \frac{w_{\mathcal{I}}sin2\phi}{2z_{\mathcal{I}}} \tag{33b}$$

Since the system has four states, the observability matrix needs to have at least four independent rows for the system to be observable. Thus we consider Lie derivatives of the ventral flow observations up to the third order:

$$\mathcal{L}_f^0 y_{\hat{\omega}_y} = \frac{-v_{\mathcal{I}}cos^2\phi}{z_{\mathcal{I}}} + \frac{w_{\mathcal{I}}sin2\phi}{2z_{\mathcal{I}}} \tag{34a}$$

$$\mathcal{L}_f^1 y_{\hat{\omega}_y} = \frac{-(cos(\phi)(sin(\phi)w_{\mathcal{I}}^2 - v_{\mathcal{I}}cos(\phi)w_{\mathcal{I}} + gz_{\mathcal{I}}sin(\phi)))}{z_{\mathcal{I}}^2} \tag{34b}$$

$$\begin{aligned}\mathcal{L}_f^2 y_{\hat{\omega}_y} = \quad & cos(\phi)[\frac{2mw_{\mathcal{I}}^3 sin(\phi) + Tv_{\mathcal{I}}z_{\mathcal{I}}cos^2(\phi) - 2mv_{\mathcal{I}}w_{\mathcal{I}}^2 cos(\phi)}{(mz_{\mathcal{I}}^3)} + \\ & \frac{3gmw_{\mathcal{I}}z_{\mathcal{I}}sin(\phi) - Tw_{\mathcal{I}}z_{\mathcal{I}}cos(\phi)sin(\phi) - gmv_{\mathcal{I}}z_{\mathcal{I}}cos(\phi)}{(mz_{\mathcal{I}}^3)}]\end{aligned} \tag{34c}$$

$$\begin{aligned}\mathcal{L}_f^3 y_{\hat{\omega}_y} = \quad & -3cos(\phi)[\frac{2mw_{\mathcal{I}}^4 sin(\phi) - (Tgz_{\mathcal{I}}^2 sin(2\phi))/2 - Tw^2 z_{\mathcal{I}}sin(2\phi) + g^2 mz_{\mathcal{I}}^2 sin(\phi) - 2mv_{\mathcal{I}}w_{\mathcal{I}}^3 cos(\phi)}{(mz_{\mathcal{I}}^4)} + \\ & \frac{2Tv_{\mathcal{I}}w_{\mathcal{I}}z_{\mathcal{I}}cos^2(\phi) + 4gmw_{\mathcal{I}}^2 z_{\mathcal{I}}sin(\phi) - 2gmv_{\mathcal{I}}w_{\mathcal{I}}z_{\mathcal{I}}cos(\phi)}{(mz_{\mathcal{I}}^4)}]\end{aligned} \tag{34d}$$

Computing the Jacobian of the Lie derivatives, we obtain the elements of the observability matrix, as follows:

$$\mathcal{O}_1 = \left\{ \frac{-cos^2(\phi)}{z_{\mathcal{I}}} \quad \frac{(w_{\mathcal{I}}cos(2\phi) + v_{\mathcal{I}}sin(2\phi))}{z_{\mathcal{I}}} \quad \frac{(2v_{\mathcal{I}}cos^2(\phi) - w_{\mathcal{I}}sin(2\phi))}{(2z_{\mathcal{I}}^2)} \quad \frac{sin(2\phi)}{(2z_{\mathcal{I}})} \right\} \tag{35a}$$

$$\mathcal{O}_{2,1} = \frac{(w_{\mathcal{I}}cos^2(\phi))}{(z_{\mathcal{I}}^2)} \tag{35b}$$

$$\mathcal{O}_{2,2} = \frac{-(cos(2\phi)w^2 + v_{\mathcal{I}}sin(2\phi)w_{\mathcal{I}} + gz_{\mathcal{I}}cos(2\phi))}{z_{\mathcal{I}}^2} \tag{35c}$$

$$\mathcal{O}_{2,3} = \frac{(cos(\phi)(2sin(\phi)w_{\mathcal{I}}^2 - 2v_{\mathcal{I}}cos(\phi)w_{\mathcal{I}} + gz_{\mathcal{I}}sin(\phi)))}{(z_{\mathcal{I}}^3)} \tag{35d}$$

$$\mathcal{O}_{2,4} = \frac{(cos(\phi)(v_{\mathcal{I}}cos(\phi) - 2w_{\mathcal{I}}sin(\phi)))}{z_{\mathcal{I}}^2} \tag{35e}$$

$$\mathcal{O}_{3,1} = \frac{-(cos^2(\phi)(2mw_{\mathcal{I}}^2 - Tz_{\mathcal{I}}cos(\phi) + gmz_{\mathcal{I}}))}{(mz_{\mathcal{I}}^3)} \tag{35f}$$

$$\begin{aligned}\mathcal{O}_{3,2} = \quad & \frac{4mw_{\mathcal{I}}^3 cos^2(\phi) - 2mw_{\mathcal{I}}^3 - 3gmw_{\mathcal{I}}z_{\mathcal{I}} + 2mv_{\mathcal{I}}w_{\mathcal{I}}^2 sin(2\phi) + 2Tw_{\mathcal{I}}z_{\mathcal{I}}cos(\phi)}{(mz_{\mathcal{I}}^3)} + \\ & \frac{-3Tv_{\mathcal{I}}z_{\mathcal{I}}(sin(\phi) - sin^3(\phi)) - 3Tw_{\mathcal{I}}z_{\mathcal{I}}cos^3(\phi) + 6gmw_{\mathcal{I}}z_{\mathcal{I}}cos^2(\phi) + gmv_{\mathcal{I}}z_{\mathcal{I}}sin(2\phi)}{(mz_{\mathcal{I}}^3)}\end{aligned} \tag{35g}$$

$$\begin{aligned}\mathcal{O}_{3,3} = \quad & -2cos(\phi)[\frac{3mw_{\mathcal{I}}^3 sin(\phi) + Tv_{\mathcal{I}}z_{\mathcal{I}}cos^2(\phi) - 3mv_{\mathcal{I}}w_{\mathcal{I}}^2 cos(\phi) + 3gmw_{\mathcal{I}}z_{\mathcal{I}}sin(\phi)}{(mz_{\mathcal{I}}^4)} + \\ & \frac{-Tw_{\mathcal{I}}z_{\mathcal{I}}cos(\phi)sin(\phi) - gmv_{\mathcal{I}}z_{\mathcal{I}}cos(\phi)}{(mz_{\mathcal{I}}^4)}]\end{aligned} \tag{35h}$$

$$\mathcal{O}_{3,4} = \frac{(cos(\phi)(6msin(\phi)w_{\mathcal{I}}^2 - 4mv_{\mathcal{I}}cos(\phi)w_{\mathcal{I}} + 3gmz_{\mathcal{I}}sin(\phi) - Tz_{\mathcal{I}}cos(\phi)sin(\phi)))}{(mz_{\mathcal{I}}^3)} \tag{35i}$$

$$\mathcal{O}_{4,1} = \frac{(6w_{\mathcal{I}}cos^2(\phi)(mw_{\mathcal{I}}^2 - Tz_{\mathcal{I}}cos(\phi) + gmz_{\mathcal{I}}))}{(mz_{\mathcal{I}}^4)} \tag{35j}$$

$$\mathcal{O}_{4,2} = [\frac{9Tgz_{\mathcal{I}}^2cos(3\phi) - 24mw_{\mathcal{I}}^4cos(2\phi) + 18Tw_{\mathcal{I}}^2z_{\mathcal{I}}cos(3\phi) - 24mv_{\mathcal{I}}w_{\mathcal{I}}^3sin(2\phi) - 12g^2mz_{\mathcal{I}}^2cos(2\phi) + 3Tgz_{\mathcal{I}}^2cos(\phi)}{(4mz_{\mathcal{I}}^4)} + \frac{6Tw_{\mathcal{I}}^2z_{\mathcal{I}}cos(\phi) + 18Tv_{\mathcal{I}}w_{\mathcal{I}}z_{\mathcal{I}}sin(3\phi) - 48gmw_{\mathcal{I}}^2z_{\mathcal{I}}cos(2\phi) + 18Tv_{\mathcal{I}}w_{\mathcal{I}}z_{\mathcal{I}}sin(\phi) - 24gmv_{\mathcal{I}}w_{\mathcal{I}}z_{\mathcal{I}}sin(2\phi)}{(4mz_{\mathcal{I}}^4)}] \tag{35k}$$

$$\mathcal{O}_{4,3} = 6cos(\phi)[\frac{4mw_{\mathcal{I}}^4sin(\phi) - (Tgz_{\mathcal{I}}^2sin(2\phi))/2 - (3Tw_{\mathcal{I}}^2z_{\mathcal{I}}sin(2\phi))/2 + g^2mz_{\mathcal{I}}^2sin(\phi) - 4mv_{\mathcal{I}}w_{\mathcal{I}}^3cos(\phi)}{(mz_{\mathcal{I}}^5)} + \frac{3Tv_{\mathcal{I}}w_{\mathcal{I}}z_{\mathcal{I}}cos^2(\phi) + 6gmw_{\mathcal{I}}^2z_{\mathcal{I}}sin(\phi) - 3gmv_{\mathcal{I}}w_{\mathcal{I}}z_{\mathcal{I}}cos(\phi)}{(mz_{\mathcal{I}}^5)}] \tag{35l}$$

$$\mathcal{O}_{4,4} = -3cos(\phi)[\frac{8mw_{\mathcal{I}}^3sin(\phi) + 2Tv_{\mathcal{I}}z_{\mathcal{I}}cos^2(\phi) - 6mv_{\mathcal{I}}w_{\mathcal{I}}^2cos(\phi) + 8gmw_{\mathcal{I}}z_{\mathcal{I}}sin(\phi)}{(mz_{\mathcal{I}}^4)} + \frac{-4Tw_{\mathcal{I}}z_{\mathcal{I}}cos(\phi)sin(\phi) - 2gmv_{\mathcal{I}}z_{\mathcal{I}}cos(\phi)}{(mz_{\mathcal{I}}^4)}] \tag{35m}$$

It can be verified that the above elements result in a full rank observability matrix for various state-input value combinations. Thus the system represented by equation 13 is locally weakly observable.

APPENDIX C
OBSERVABILITY ANALYSIS OF THE COMPLETE MODEL (SYSTEM $\sum_1$)

In this appendix, we derive the observability matrix for the complete model of the estimator studied in this investigation. The motion model and observation equations of the system (described in equation 17) can be restated as follows:

$$\boldsymbol{f}(\boldsymbol{x},t) = \frac{d}{dt}\begin{bmatrix} v_{\mathcal{I}} \\ \phi \\ p \\ z_{\mathcal{I}} \\ w_{\mathcal{I}} \end{bmatrix} = \begin{bmatrix} Tsin\phi/m \\ p \\ M_{x_{\mathcal{B}}}/I_{x_{\mathcal{B}}} \\ w_{\mathcal{I}} \\ Tcos\phi/m - g \end{bmatrix} \tag{36a}$$

$$\boldsymbol{y} = \begin{bmatrix} y_{\hat{\omega}_y} \\ y_{\hat{\omega}_z} \end{bmatrix} = \begin{bmatrix} \dfrac{-v_{\mathcal{I}}cos^2\phi}{z_{\mathcal{I}}} + \dfrac{w_{\mathcal{I}}sin2\phi}{2z_{\mathcal{I}}} + p \\ \dfrac{-v_{\mathcal{I}}sin2\phi}{2z_{\mathcal{I}}} - \dfrac{w_{\mathcal{I}}cos^2\phi}{z_{\mathcal{I}}} \end{bmatrix} \tag{36b}$$

Since the system has five states, the observability matrix needs to have at least five independent rows for the system to be locally weakly observable. Thus we will have to consider Lie derivatives, at least up to the second order of one of the observations and up to the first order of the other observation equation. The said Lie derivatives are derived in the following equations:

$$\mathcal{L}_f^0 y_{\hat{\omega}_y} = \frac{-v_{\mathcal{I}}cos^2\phi}{z_{\mathcal{I}}} + \frac{w_{\mathcal{I}}sin2\phi}{2z_{\mathcal{I}}} + p \tag{37a}$$

$$\mathcal{L}_f^0 y_{\hat{\omega}_z} = \frac{-v_{\mathcal{I}}sin2\phi}{2z_{\mathcal{I}}} - \frac{w_{\mathcal{I}}cos^2\phi}{z_{\mathcal{I}}} \tag{37b}$$

$$\mathcal{L}_f^1 y_{\hat{\omega}_y} = \frac{2M_{x_{\mathcal{B}}}z_{\mathcal{I}}^2 + I_{x_{\mathcal{B}}}v_{\mathcal{I}}w_{\mathcal{I}} - I_{x_{\mathcal{B}}}w_{\mathcal{I}}^2 sin(2\phi) + I_{x_{\mathcal{B}}}v_{\mathcal{I}}w_{\mathcal{I}}cos(2\phi) - I_{x_{\mathcal{B}}}gz_{\mathcal{I}}sin(2\phi) + 2I_{x_{\mathcal{B}}}pw_{\mathcal{I}}z_{\mathcal{I}}cos(2\phi) + 2I_{x_{\mathcal{B}}}pv_{\mathcal{I}}z_{\mathcal{I}}sin(2\phi)}{2I_{x_{\mathcal{B}}}z_{\mathcal{I}}^2} \tag{37c}$$

$$\mathcal{L}_f^1 y_{\hat{\omega}_z} = \frac{(mw_{\mathcal{I}}^2 cos^2(\phi) - Tz_{\mathcal{I}}cos(\phi) + mpv_{\mathcal{I}}z_{\mathcal{I}} + gmz_{\mathcal{I}}cos^2(\phi) + mv_{\mathcal{I}}w_{\mathcal{I}}sin(2\phi)/2 - 2mpv_{\mathcal{I}}z_{\mathcal{I}}cos^2(\phi) + mpw_{\mathcal{I}}z_{\mathcal{I}}sin(2\phi))}{(mz_{\mathcal{I}}^2)} \tag{37d}$$

$$\begin{aligned} \mathcal{L}_f^2 y_{\hat{\omega}_y} = \; & -[\frac{4I_{x_{\mathcal{B}}}mvw^2 - 4I_{x_{\mathcal{B}}}mw_{\mathcal{I}}^3 sin(2\phi) - 4I_{x_{\mathcal{B}}}Tpz_{\mathcal{I}}^2 cos(\phi) - I_{x_{\mathcal{B}}}Tv_{\mathcal{I}}z_{\mathcal{I}}cos(3\phi) + I_{x_{\mathcal{B}}}Tw_{\mathcal{I}}z_{\mathcal{I}}sin(3\phi) + 2I_{x_{\mathcal{B}}}gmv_{\mathcal{I}}z_{\mathcal{I}}}{(4I_{x_{\mathcal{B}}}mz_{\mathcal{I}}^3)} + \\ & \frac{4I_{x_{\mathcal{B}}}mv_{\mathcal{I}}w_{\mathcal{I}}^2 cos(2\phi) - 4M_{x_{\mathcal{B}}}mw_{\mathcal{I}}z_{\mathcal{I}}^2 cos(2\phi) - 4M_{x_{\mathcal{B}}}mv_{\mathcal{I}}z_{\mathcal{I}}^2 sin(2\phi) - 3I_{x_{\mathcal{B}}}Tv_{\mathcal{I}}z_{\mathcal{I}}cos(\phi) + I_{x_{\mathcal{B}}}Tw_{\mathcal{I}}z_{\mathcal{I}}sin(\phi)}{(4I_{x_{\mathcal{B}}}mz_{\mathcal{I}}^3)} + \\ & \frac{8I_{x_{\mathcal{B}}}mpw_{\mathcal{I}}^2 z_{\mathcal{I}}cos(2\phi) - 8I_{x_{\mathcal{B}}}mp^2 v_{\mathcal{I}}z_{\mathcal{I}}^2 cos(2\phi) + 8I_{x_{\mathcal{B}}}mp^2 w_{\mathcal{I}}z_{\mathcal{I}}^2 sin(2\phi) + 2I_{x_{\mathcal{B}}}gmv_{\mathcal{I}}z_{\mathcal{I}}cos(2\phi)}{(4I_{x_{\mathcal{B}}}mz_{\mathcal{I}}^3)} + \\ & \frac{8I_{x_{\mathcal{B}}}gmpz^2 cos(2\phi) + 8I_{x_{\mathcal{B}}}mpvwzsin(2\phi) - 6I_{x_{\mathcal{B}}}gmw_{\mathcal{I}}z_{\mathcal{I}}sin(2\phi)}{(4I_{x_{\mathcal{B}}}mz_{\mathcal{I}}^3)}] \end{aligned} \tag{37e}$$

The 25 elements of the observability matrix can be computed as:

$$\mathcal{O}_1 = \left\{ \frac{-cos^2(\phi)}{z_{\mathcal{I}}} \quad \frac{(w_{\mathcal{I}}cos(2\phi) + v_{\mathcal{I}}sin(2\phi))}{z_{\mathcal{I}}} \quad 1 \quad \frac{(2v_{\mathcal{I}}cos^2(\phi) - w_{\mathcal{I}}sin(2\phi))}{(2z_{\mathcal{I}}^2)} \quad \frac{sin(2\phi)}{(2z_{\mathcal{I}}^2)} \right\} \tag{38a}$$

$$\mathcal{O}_2 = \left\{ \frac{-sin(2\phi)}{(2z_{\mathcal{I}})} \quad \frac{-(v_{\mathcal{I}}cos(2\phi) - w_{\mathcal{I}}sin(2\phi))}{z_{\mathcal{I}}} \quad 0 \quad \frac{(2w_{\mathcal{I}}cos^2(\phi) + v_{\mathcal{I}}sin(2\phi))}{(2z_{\mathcal{I}}^2)} \quad \frac{-cos^2(\phi)}{z_{\mathcal{I}}} \right\} \tag{38b}$$

$$\mathcal{O}_{3,1} = \frac{(w_{\mathcal{I}} + w_{\mathcal{I}}cos(2\phi) + 2pz_{\mathcal{I}}sin(2\phi))}{(2z_{\mathcal{I}}^2)} \tag{38c}$$

$$\mathcal{O}_{3,2} = \frac{-(w_{\mathcal{I}}^2 cos(2\phi) + gz_{\mathcal{I}}cos(2\phi) + v_{\mathcal{I}}w_{\mathcal{I}}sin(2\phi) + 2pw_{\mathcal{I}}z_{\mathcal{I}}sin(2\phi) - 2pv_{\mathcal{I}}z_{\mathcal{I}}cos(2\phi))}{(z_{\mathcal{I}}^2)} \tag{38d}$$

$$\mathcal{O}_{3,3} = \frac{-(w_{\mathcal{I}}cos(2\phi) + v_{\mathcal{I}}sin(2\phi))}{(z_{\mathcal{I}})} \tag{38e}$$

$$\mathcal{O}_{3,4} = \frac{-(2v_{\mathcal{I}}w_{\mathcal{I}} - 2w_{\mathcal{I}}^2 sin(2\phi) + 2v_{\mathcal{I}}w_{\mathcal{I}}cos(2\phi) - gzsin(2\phi) + 2pv_{\mathcal{I}}z_{\mathcal{I}}sin(2\phi) + 2pw_{\mathcal{I}}z_{\mathcal{I}}cos(2\phi))}{(2z_{\mathcal{I}}^3)} \tag{38f}$$

$$\mathcal{O}_{3,5} = \frac{(v_{\mathcal{I}} + v_{\mathcal{I}} cos(2\phi) - 2w_{\mathcal{I}} sin(2\phi) + 2pz_{\mathcal{I}} cos(2\phi))}{(2z_{\mathcal{I}}^2)} \tag{38g}$$

$$\mathcal{O}_{4,1} = \frac{(w_{\mathcal{I}} sin(2\phi) - 2pz_{\mathcal{I}} cos(2\phi))}{(2z_{\mathcal{I}}^2)} \tag{38h}$$

$$\mathcal{O}_{4,2} = \frac{(Tz_{\mathcal{I}} sin(\phi) - mw_{\mathcal{I}}^2 sin(2\phi) + mv_{\mathcal{I}} w_{\mathcal{I}} cos(2\phi) - gmz_{\mathcal{I}} sin(2\phi) + 2mpw_{\mathcal{I}} z_{\mathcal{I}} cos(2\phi) + 2mpv_{\mathcal{I}} z_{\mathcal{I}} sin(2\phi))}{(mz_{\mathcal{I}}^2)} \tag{38i}$$

$$\mathcal{O}_{4,3} = \frac{-(v_{\mathcal{I}} cos(2\phi) - wsin(2\phi))}{(z_{\mathcal{I}}} \tag{38j}$$

$$\mathcal{O}_{4,4} = \frac{-(2mw_{\mathcal{I}}^2 cos^2(\phi) - Tz_{\mathcal{I}} cos(\phi) + mpv_{\mathcal{I}} z_{\mathcal{I}} + gmz_{\mathcal{I}} cos^2(\phi) + mv_{\mathcal{I}} w_{\mathcal{I}} sin(2\phi) - 2mpv_{\mathcal{I}} z_{\mathcal{I}} cos^2(\phi) + mpw_{\mathcal{I}} z_{\mathcal{I}} sin(2\phi))}{mz_{\mathcal{I}}^3} \tag{38k}$$

$$\mathcal{O}_{4,5} = \frac{(4w_{\mathcal{I}} cos^2(\phi) + v_{\mathcal{I}} sin(2\phi) + 2pz_{\mathcal{I}} sin(2\phi))}{2z_{\mathcal{I}}^2} \tag{38l}$$

$$\begin{aligned}\mathcal{O}_{5,1} = \quad & -[\frac{2I_{x_{\mathcal{B}}} mw_{\mathcal{I}}^2 cos^2(\phi) - M_{x_{\mathcal{B}}} mz_{\mathcal{I}}^2 sin(2\phi) - I_{x_{\mathcal{B}}} Tz_{\mathcal{I}} cos^3(\phi)}{I_{x_{\mathcal{B}}} mz_{\mathcal{I}}^3} + \\ & \frac{2I_{x_{\mathcal{B}}} mp^2 z_{\mathcal{I}}^2 + I_{x_{\mathcal{B}}} gmz_{\mathcal{I}} cos^2(\phi) - 4I_{x_{\mathcal{B}}} mp^2 z_{\mathcal{I}}^2 cos^2(\phi) + 2I_{x_{\mathcal{B}}} mpw_{\mathcal{I}} z_{\mathcal{I}} sin(2\phi)}{I_{x_{\mathcal{B}}} mz_{\mathcal{I}}^3}]\end{aligned} \tag{38m}$$

$$\begin{aligned}\mathcal{O}_{5,2} = \quad & -[\frac{3I_{x_{\mathcal{B}}} Tw_{\mathcal{I}} z_{\mathcal{I}} cos(3\phi) - 8I_{x_{\mathcal{B}}} mw_{\mathcal{I}}^3 cos(2\phi) + 4I_{x_{\mathcal{B}}} Tpz_{\mathcal{I}}^2 sin(\phi) + 3I_{x_{\mathcal{B}}} Tv_{\mathcal{I}} z_{\mathcal{I}} sin(3\phi) - 8M_{x_{\mathcal{B}}} mv_{\mathcal{I}} z_{\mathcal{I}}^2 cos(2\phi)}{I_{x_{\mathcal{B}}} mz_{\mathcal{I}}^3} + \\ & \frac{-8Imv_{\mathcal{I}} w_{\mathcal{I}}^2 sin(2\phi) + 8M_{x_{\mathcal{B}}} mw_{\mathcal{I}} z_{\mathcal{I}}^2 sin(2\phi) + I_{x_{\mathcal{B}}} Tw_{\mathcal{I}} z_{\mathcal{I}} cos(\phi) + 3I_{x_{\mathcal{B}}} Tv_{\mathcal{I}} z_{\mathcal{I}} sin(\phi) - 16I_{x_{\mathcal{B}}} gmpz_{\mathcal{I}}^2 sin(2\phi)}{I_{x_{\mathcal{B}}} mz_{\mathcal{I}}^3} + \\ & \frac{-16I_{x_{\mathcal{B}}} mpw_{\mathcal{I}}^2 z_{\mathcal{I}} sin(2\phi) + 16I_{x_{\mathcal{B}}} mp^2 w_{\mathcal{I}} z^2 cos(2\phi) + 16I_{x_{\mathcal{B}}} mp^2 vz_{\mathcal{I}}^2 sin(2\phi) - 12I_{x_{\mathcal{B}}} gmw_{\mathcal{I}} z_{\mathcal{I}} cos(2\phi)}{4I_{x_{\mathcal{B}}} mz_{\mathcal{I}}^3} + \\ & \frac{-4I_{x_{\mathcal{B}}} gmv_{\mathcal{I}} z_{\mathcal{I}} sin(2\phi) + 16I_{x_{\mathcal{B}}} mpv_{\mathcal{I}} w_{\mathcal{I}} z_{\mathcal{I}} cos(2\phi)}{4I_{x_{\mathcal{B}}} mz_{\mathcal{I}}^3}]\end{aligned} \tag{38n}$$

$$\mathcal{O}_{5,3} = \quad -[\frac{2mw_{\mathcal{I}}^2 cos(2\phi) - Tz_{\mathcal{I}} cos(\phi) + 2gmz_{\mathcal{I}} cos(2\phi) + 2mv_{\mathcal{I}} w_{\mathcal{I}} sin(2\phi) - 4mpv_{\mathcal{I}} z_{\mathcal{I}} cos(2\phi) + 4mpw_{\mathcal{I}} z_{\mathcal{I}} sin(2\phi)}{mz_{\mathcal{I}}^2}] \tag{38o}$$

$$\begin{aligned}\mathcal{O}_{5,4} = \quad & [\frac{6Imv_{\mathcal{I}} w_{\mathcal{I}}^2 - 6I_{x_{\mathcal{B}}} mw_{\mathcal{I}}^3 sin(2\phi) - 2ITpz_{\mathcal{I}}^2 cos(\phi) - I_{x_{\mathcal{B}}} Tv_{\mathcal{I}} z_{\mathcal{I}} cos(3\phi) + I_{x_{\mathcal{B}}} Tw_{\mathcal{I}} z_{\mathcal{I}} sin(3\phi) + 2I_{x_{\mathcal{B}}} gmv_{\mathcal{I}} z_{\mathcal{I}}}{2I_{x_{\mathcal{B}}} mz_{\mathcal{I}}^4} + \\ & \frac{-2M_{x_{\mathcal{B}}} mw_{\mathcal{I}} z_{\mathcal{I}}^2 cos(2\phi) - 2M_{x_{\mathcal{B}}} mv_{\mathcal{I}} z_{\mathcal{I}}^2 sin(2\phi) - 3I_{x_{\mathcal{B}}} Tv_{\mathcal{I}} z_{\mathcal{I}} cos(\phi) + I_{x_{\mathcal{B}}} Tw_{\mathcal{I}} z_{\mathcal{I}} sin(\phi) + 8I_{x_{\mathcal{B}}} mpw_{\mathcal{I}}^2 z_{\mathcal{I}} cos(2\phi)}{2I_{x_{\mathcal{B}}} mz_{\mathcal{I}}^4} + \\ & \frac{-4Imp^2 v_{\mathcal{I}} z_{\mathcal{I}}^2 cos(2\phi) + 4Imp^2 w_{\mathcal{I}} z_{\mathcal{I}}^2 sin(2\phi) + 2I_{x_{\mathcal{B}}} gmv_{\mathcal{I}} z_{\mathcal{I}} cos(2\phi) - 6I_{x_{\mathcal{B}}} gmw_{\mathcal{I}} z_{\mathcal{I}} sin(2\phi)}{2I_{x_{\mathcal{B}}} mz_{\mathcal{I}}^4} + \\ & \frac{4Igmpz_{\mathcal{I}}^2 cos(2\phi) + 8I_{x_{\mathcal{B}}} mpv_{\mathcal{I}} w_{\mathcal{I}} z_{\mathcal{I}} sin(2\phi) + 6I_{x_{\mathcal{B}}} mv_{\mathcal{I}} w_{\mathcal{I}}^2 cos(2\phi)}{2I_{x_{\mathcal{B}}} mz_{\mathcal{I}}^4}]\end{aligned} \tag{38p}$$

$$\begin{aligned}\mathcal{O}_{5,5} = \quad & -[\frac{8I_{x_{\mathcal{B}}} mv_{\mathcal{I}} w_{\mathcal{I}} - 4M_{x_{\mathcal{B}}} mz_{\mathcal{I}}^2 cos(2\phi) - 12I_{x_{\mathcal{B}}} mw_{\mathcal{I}}^2 sin(2\phi) + I_{x_{\mathcal{B}}} Tz_{\mathcal{I}} sin(\phi) + I_{x_{\mathcal{B}}} Tz_{\mathcal{I}} sin(3\phi) + 8I_{x_{\mathcal{B}}} mp^2 z_{\mathcal{I}}^2 sin(2\phi)}{4I_{x_{\mathcal{B}}} mz_{\mathcal{I}}^3} + \\ & \frac{8I_{x_{\mathcal{B}}} mv_{\mathcal{I}} w_{\mathcal{I}} cos(2\phi) - 6I_{x_{\mathcal{B}}} gmz_{\mathcal{I}} sin(2\phi) + 16I_{x_{\mathcal{B}}} mpw_{\mathcal{I}} z_{\mathcal{I}} cos(2\phi) + 8I_{x_{\mathcal{B}}} mpv_{\mathcal{I}} z_{\mathcal{I}} sin(2\phi)}{4I_{x_{\mathcal{B}}} mz_{\mathcal{I}}^3}]\end{aligned} \tag{38q}$$

It can be verified that all the rows of the obtained observability matrix are linearly independent, thus rendering the system locally weakly observable.

Part II
LITERATURE STUDY

2

Inertial Measurements based Attitude Estimation in MAVs

A prerequisite to successful autonomous flight is the determination and control of the vehicle's orientation in space with respect to an inertial frame of reference. The conventional method for attitude estimation in MAVs is the use of IMUs comprising of accelerometers, gyroscopes and sometimes magnetometers. MEMS IMU sensors are popular, in the field of MAVs, because they perfectly fit the stringent weight and size restrictions that come with the challenge of miniaturization of these platforms. However, these sensors suffer from high noise and inherent drift that lead to erroneous attitude estimates. So, these attitude estimates, obtained from the inertial measurements, have to be corrected by software solutions and/or complementary sensors. This chapter is intended to present a brief review of the inertial measurements based attitude estimation techniques and highlight the drawbacks of the approach.

2.1. Inertial Sensors

Specific force sensors: accelerometers, and rotation sensors: gyroscopes, are conventionally used in MAVs as the inertial motion sensors to estimate vehicle position, orientation and velocities. Often these sensors are also supplemented by magnetic field orientation sensors, called magnetometers. This section intends to discuss the basic principles of operation and the mathematical models of these sensors.

Accelerometers

An accelerometer is the standard device used in MAVs to measure linear accelerations. All accelerometers work on the principle of a mass-spring-damper system, and measure the force required to accelerate a proof mass in the vehicle's body reference frame. Consider the system represented by figure 2.1.

Let $y_s = Y_s sin(\omega_s t)$ denote the displacement of the vehicle containing the system and x_s denote the displacement of the proof mass m. If the relative displacement of the proof mass is denoted by $r_s = x_s - y_s$, then, using Newton's second law, the equation of motion of the proof mass can be written as:

$$m\ddot{r}_s + c\dot{r}_s + kr_s = -m\ddot{y}_s = m\omega_s^2 Y_s sin(\omega t) \tag{2.1}$$

where, c denotes the damping constant of the damper and k denotes the spring constant.

[1] https://leancrew.com/all-this/2012/05/accelerometers/

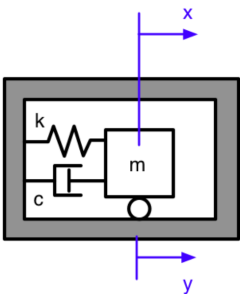

Figure 2.1: Spring-mass-damper system. Source:[1]

Then the steady state solution for r_s is also a sinusoid, with the same frequency, ω_s, and amplitude, R_s, defined by:

$$R_s = \frac{Y_s \left(\frac{\omega_s}{\omega_{sn}}\right)^2}{\sqrt{\left[1-\left(\frac{\omega_s}{\omega_{sn}}\right)^2\right]^2 + \left[2\zeta\frac{\omega_s}{\omega_{sn}}\right]^2}} \tag{2.2}$$

Where, ω_{sn} denotes the natural frequency of the spring mass system, and ζ is the damping ratio:

$$\begin{aligned} \omega_{sn} &= \sqrt{\frac{k}{m}} \\ \zeta &= \frac{c}{2\sqrt{km}} \end{aligned} \tag{2.3}$$

In equation 2.1 if the ratio $\frac{\omega_s}{\omega_{sn}}$ is assumed to be small ($\frac{\omega_s}{\omega_{sn}} << 1$) then the relation can be simplified to:

$$R_s = Y_s \left(\frac{\omega_s}{\omega_{sn}}\right)^2 \tag{2.4}$$

Thus, if the spring mass damper system is designed with a high ω_{sn} and if motion frequency of the vehicle if small compared to that value, then the displacement amplitude, R_s, of the proof mass will be proportional to the acceleration amplitude, $\omega_s^2 Y_s$, of the vehicle. Thus the acceleration of the vehicle can be measured by measuring the displacement of the proof mass and using the known natural frequency of the system. This is the basic principle of operation of all accelerometers [40].

It should be noted that the measurement of a vehicle's acceleration is complicated by the fact that it is almost impossible to distinguish between the force acting on the proof mass due to earth's gravity, g and the force required to accelerate the proof mass. Thus accelerometers measure the specific force, f^b, in vehicle's body frame, and not the vehicle's true acceleration in navigation frame, a^n_{ii}, as described in equation 2.5.

Here, the superscripts, n and b, represent the navigation and body reference frames respectively and R^{bn} is the rotation matrix for transforming values in navigation frame to the body frame. The subscripts describe the frames in which subsequent differentiations of the position have been performed to obtain the linear accelerations (with i representing the inertial frame of reference). Thus a^n_{ii} refers to the acceleration of a vehicle, w.r.t navigation reference frame, computed by double differentiating the position of the vehicle in inertial frame. For navigation, the acceleration a^n_{nn} is of interest and it can be derived from a^n_{ii} as: (formulation adopted from Kok et al. [41])

$$f^b = R^{bn}(a^n_{ii} - g^n) \tag{2.5}$$

$$a^n_{nn} = a^n_{ii} - 2\omega^n_{ie} \times v^n_n - \omega^n_{ie} \times \omega^n_{ie} \times p^n \tag{2.6}$$

Where, ω_{ie} denotes the angular velocity of earth, v is the velocity of the vehicle and p is the distance of the sensor from the earth's centre. Note that the relation has been derived with the assumption that the navigation frame is fixed to the earth reference frame, which is valid as long as the displacement of the vehicle remains small compared to the earth's size. This is a reasonable assumption for MAV applications. The term $2\omega^n_{ie} \times v^n_n$ is the Coriolis acceleration component and the term $\omega^n_{ie} \times \omega^n_{ie} \times p^n$ is the centrifugal acceleration component.

To be used in parameter estimation algorithms, a mathematical model of the sensor measurement has to be formulated and a frequently used accelerometer measurement model can be derived by combining equations 2.5 and 2.6, as formulated in equation 2.7 [41]. The model uses the assumptions that the centrifugal acceleration is absorbed in the local gravity vector and the Coriolis acceleration magnitude is small compared to the magnitude of the acceleration measurements.

$$\begin{aligned} a_{m,t} &= f^b_t + \delta^b_{a,t} + e^b_{a,t} \\ a_{m,t} &= R^{bn}_t(a^n_{nn,t} - g^n_t) + \delta^b_{a,t} + e^b_{a,t} \end{aligned} \tag{2.7}$$

Where, $\delta_{a,t}$ denotes the accelerometer bias and $e_{a,t}$ denotes the sensor noise. MEMS accelerometer noise can typically be modelled quite accurately as Gaussian noise and hence, if properly calibrated, the measurements in the three accelerometer axes are independent with the covariance matrix being diagonal. The accelerometer bias is slowly time varying. One way of treating this time varying bias is to model it as a constant parameter, assuming that the experiment duration is small compared to the time required for the bias to change significantly. Otherwise, the sensor bias variation is treated as Gaussian and the bias is estimated during the state estimation step by including it in the state vector [41].

Gyroscopes

Gyroscopes are inertial sensors that exploit the property of inertia, namely the resistance to a change in angular momentum, to sense rotational rates and the attitude of a moving platform. In their most basic form, gyroscopes are a spinning wheel or disk on an axle that is free to assume any orientation, as depicted in figure 2.2. Due to the conservation of angular momentum, a spinning rotor possesses two fundamental properties: Rigidity and Precession. Rigidity is defined as the property that resists any force or moment that tends to change the direction of the spin axis. Free gyroscopes use the rigidity property to remain in a fixed orientation relative to inertial space and hence provide reference datums for a vehicle's attitude and heading angles. Precession is defined as the property of angular change in direction of rotation under the influence of an applied force. Rate gyroscopes use the precession property to encode angular rates [42].

Though the rotating disc is the most common principle of operation for gyroscopes, gyroscopic devices based on other operating principles also exist, such as fibre optic gyroscopes, solid state ring lasers and, the ones being ubiquitously used in MAV applications, MEMS gyroscopes [13]. MEMS gyroscopes measure rotational rates based on the principle of Coriolis forces, similar to halteres in dipteran insects (discussed in Chapter 3). If a proof mass is vibrated sinusoidally in a plane that is rotating with some angular velocity, ω, then due to the acting Coriolis force the mass vibrates sinusoidally (perpendicular to the original direction of motion) with amplitude proportional to ω. Measuring this Coriolis induced motion amplitude provides the knowledge of ω.

So, the gyroscope measures the angular velocity of the body frame with respect to the inertial frame, expressed in the vehicle body frame. Let this angular velocity be denoted by ω^b_{ib}. Now, using

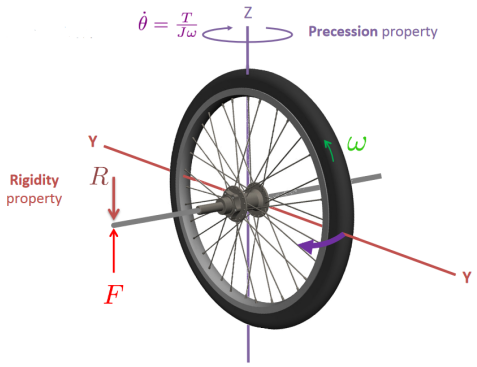

Figure 2.2: The spinning wheel: Demonstration of gyroscopic precession and rigidity. Source [42]

the same notations as were used for the derivation of the accelerometer measurement model, ω_{ib}^{b} can be expressed as: [41]

$$\omega_{ib}^{b} = R^{bn}(\omega_{ie}^{n} + \omega_{en}^{n}) + \omega_{nb}^{b} \tag{2.8}$$

To determine the orientation of the body with respect to the navigation frame, the angular velocity ω_{nb}^{b} is of interest. Using equation 2.8, a gyroscope measurement model can be described as:

$$\begin{aligned} \omega_{m,t} &= \omega_{ib,t}^{b} + \delta_{\omega,t}^{b} + e_{\omega,t}^{b} \\ \omega_{m,t} &= R_{t}^{bn}(\omega_{ie,t}^{n} + \omega_{en,t}^{n}) + \omega_{nb,t}^{b} + \delta_{\omega,t}^{b} + e_{\omega,t}^{b} \end{aligned} \tag{2.9}$$

Here, $\delta_{\omega,t}^{b}$ and $e_{\omega,t}^{b}$ represent the sensor bias and sensor noise respectively. Similar to accelerometers, MEMS gyroscope noise can be modelled as Gaussian and the gyroscope bias is slowly time varying, which can either be modelled as a constant parameter or estimated as a part of the time varying state vector.

Apart from modelling of the sensor noise and bias, various other modelling choices are also possible. If the sensor platform does not travel significant distances compared to the size of the earth, then the navigation frame can be assumed to be fixed to the earth frame making ω_{en}^{n} zero. Further, the magnitude of earth rotation, ω_{ie}^{n}, is fairly small compared to the magnitude of the actual measurements. Assuming the navigation frame is fixed to earth and the magnitude of earth's rotational velocity is negligible, the model in equation 2.9 can be simplified into:

$$\omega_{m,t} = \omega_{nb,t}^{b} + \delta_{\omega,t}^{b} + e_{\omega,t}^{b} \tag{2.10}$$

Magnetometers

Magnetometers measure the local magnetic field, which consists of the earth's magnetic field as well as the magnetic field induced by other magnetic materials in the vicinity. The local earth magnetic field is denoted by m^{n}. The horizontal component of m^{n} points towards the magnetic north pole of earth and ratio between the horizontal and vertical components is described by the dip angle δ. The local magnetic field, and hence the dip angle, varies with position on earth. But if we assume the that the displacement of the sensor platform is small compared to the size of the earth, then local magnetic field can be assumed to be constant during the experiment duration. In case the local

magnetic field is not polluted by the presence of other magnetic materials in the vicinity, then information about the vehicle's orientation can be extracted from the magnetometer measurements. Magnetometers are often used to determine the vehicle heading (orientation around the gravity vector). Information about a vehicle's orientation is encoded by the direction of the magnetic field vector, and its magnitude is irrelevant. Therefore, the magnetic field can be modelled as [41]:

$$m^n = \begin{bmatrix} cos\delta & 0 & sin\delta \end{bmatrix}^T \tag{2.11}$$

And the magnetometer measurements can be modeled as:

$$m_{m,t} = R^{bn,t} m_t^n + e_{m,t} \tag{2.12}$$

Where, e_m denotes the magnetometer noise and is often modelled as Gaussian noise. This model defines the vehicle's orientation with respect to the magnetic north. If the vehicle's orientation with respect to the true north is of interest then the magnetic declination has to be taken into account. However, in practice the magnetic field measurements are polluted by the effects of other magnetic materials in the sensor's vicinity, which is undesirable for orientation estimation applications [41].

2.2. Estimation Methods

Seemingly the most intuitive method of estimating the attitude of a vehicle is through integration of the rate gyroscope measurements. However, due to the time varying bias, the rates measured by the gyroscopes drift over time. Integration of these noisy, biased measurements lead to erroneous attitude estimates. This calls for a more sophisticated attitude estimation approach. Roll and pitch attitude information can also be extracted from accelerometer measurements as the accelerometer is sensitive to the gravity vector. Magnetometer measurements can be used to determine the vehicle heading. Hence, attitude information from the accelerometers and magnetometers can be fused with the gyroscope measurements to increase the accuracy of attitude estimates, as depicted in figure 2.3.

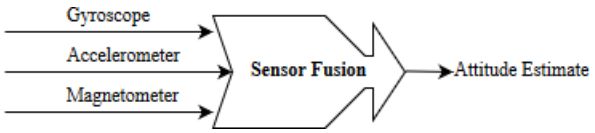

Figure 2.3: Sensor fusion to increase the accuracy of attitude estimates

Two widely used methods of sensor fusion for attitude estimation, namely Kalman filter and complimentary filter, are briefly discussed in this section.

2.2.1. Kalman Filter

In 1960, R. E. Kalman introduced Kalman filter (KF) [43] that provides a recursive solution to the discrete-data linear filtering problem. Since then, KF has been extensively utilized by researchers, particularly in the field of robotic navigation.

Consider the following discrete time controlled process:

$$\begin{aligned} \boldsymbol{x}_t &= \boldsymbol{A}\boldsymbol{x}_{t-1} + \boldsymbol{B}\boldsymbol{u}_{t-1} + \boldsymbol{w}_{t-1} \\ \boldsymbol{z}_t &= \boldsymbol{H}x_t + \boldsymbol{v}_t \end{aligned} \tag{2.13}$$

Where, $\boldsymbol{x}$ is the state vector of the process, which will be estimated by the KF. $\boldsymbol{z}$ denotes the measurements. The random variables $\boldsymbol{w}$ and $\boldsymbol{v}$ represent the process and measurement noises respectively. They are generally assumed to be independent, white noises with Gaussian distribution. Let $\boldsymbol{Q}$ denote the process noise covariance matrix and $\boldsymbol{R}$ denote the measurement noise covariance matrix. $\boldsymbol{A}$ represents the discrete system matrix, $\boldsymbol{B}$ denotes the discrete input matrix and $\boldsymbol{H}$ denotes the discrete observation matrix.

KF estimates the states of a system by using a recursive predict-update method: first, the time update step is executed during which the process state is projected forward in time, using the process motion model, to obtain the 'a priori' state predictions for the next time step. In the second step, the measurement update is executed during which the process measurements are used to correct the 'a priori' predictions and obtain an improved 'a-posteriori' estimate. After each time update and measurement update pair, the estimation process is repeated with the previous estimated states used to project the new predicted states. This recursive loop is depicted in figure 2.4. The specific equations for time and measurement updates are presented below:

Time Update

$$\begin{aligned} \hat{\boldsymbol{x}}_t^- &= \boldsymbol{A}\hat{\boldsymbol{x}}_{t-1} + \boldsymbol{B}\boldsymbol{u}_{t-1} \\ \boldsymbol{P}_t^- &= \boldsymbol{A}\boldsymbol{P}_{t-1}\boldsymbol{A}^T + \boldsymbol{Q} \end{aligned} \tag{2.14}$$

Here, $\boldsymbol{P}$ denotes the state prediction error covariance matrix. $(\hat{\cdot})$ sign over the variables represents that the value is estimated and $(-)$ sign in superscript denotes that the estimated values are not the optimal estimations but one step ahead predictions.

Measurement Update

$$\begin{aligned} \boldsymbol{K}_t &= \boldsymbol{P}_t^- \boldsymbol{H}^T (\boldsymbol{H}\boldsymbol{P}_t^- \boldsymbol{H}^T + \boldsymbol{R})^{-1} \\ \hat{\boldsymbol{x}}_t &= \hat{\boldsymbol{x}}_t^- + \boldsymbol{K}_t(\boldsymbol{z}_t - \hat{\boldsymbol{x}}_t^-) \\ \boldsymbol{P}_t &= (\boldsymbol{I} - \boldsymbol{K}_t\boldsymbol{H})\boldsymbol{P}_t^- \end{aligned} \tag{2.15}$$

Here, $\boldsymbol{K}$ denotes the Kalman gain.

As described, KF addresses the problem of estimating the state of a discrete-time controlled process which is governed by linear differential equations. However, generally the attitude estimation governing equations are non linear and hence the conventional KF has to be adapted to be able to deal with non linear systems. Extended Kalman Filter (EKF) [45] is a popular variation of the conventional Kalman filter in which the non linear state and observation equations are linearised about some nominal values before performing the time and measurement updates. Various other popular variations of the Kalman filter, like Iterated Extended Kalman Filter (IEKF) [46] and Unscented Kalman Filter (UKF)[47], also address the non linear state estimation problem.

2.2.2. Complementary Filters

Complimentary filters [48, 49] take into account the varying validity of sensor information with respect to frequency, to estimate the states. Gyroscopes provide good attitude estimates in short periods of time, but due to inherent drift, the values diverge in long term. On the other hand signals from accelerometers and magnetometers are noisy and are often corrupted by: accelerations (non gravitational) sensed by the accelerometers, and magnetic field of magnetic materials and devices in vicinity sensed by the magnetometers. Hence only the long term measurements of the accelerometers and magnetometers are reliable. A complimentary sensor takes advantage of this knowledge and uses high pass filtered gyroscopic data and low pass filtered accelerometer and magnetometer data to generate reliable attitude estimates, as depicted in figure 2.5.

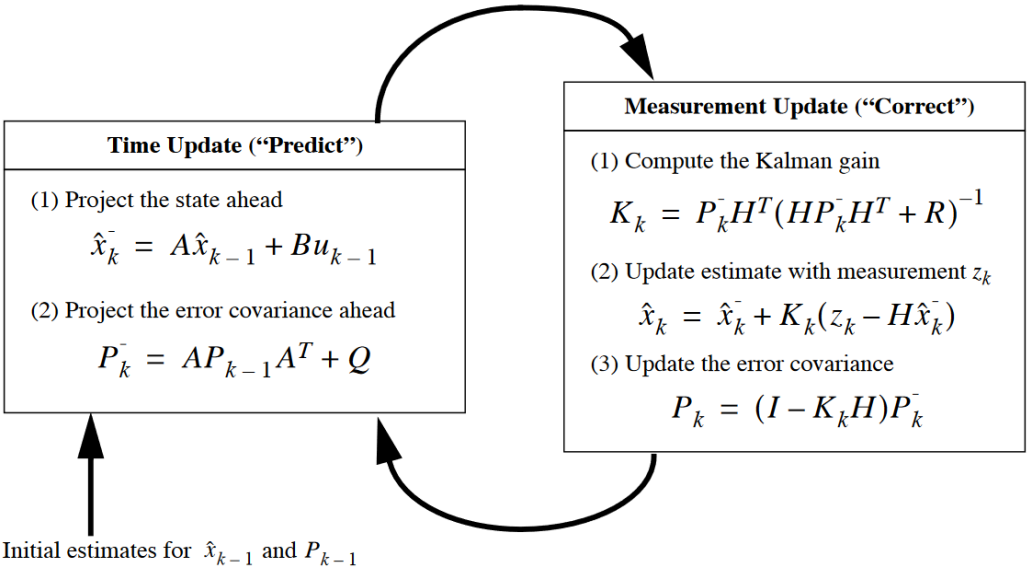

Figure 2.4: Block diagram depicting a Kalman filter operation. Source [44]

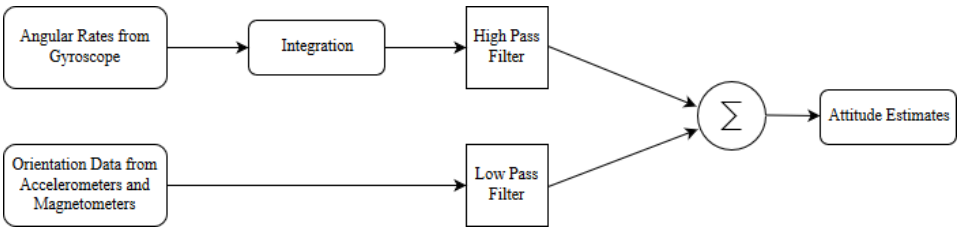

Figure 2.5: Block diagram depicting a complementary filter operation

Assume a signal x with measurements y_1 having a high frequency disturbance n_1 (like attitude data from accelerometers and magnetometers) and y_2 with a low frequency disturbance n_2 (like attitude data from the integrated gyroscope readings).

$$\begin{aligned} y_1 &= x + n_1 \\ y_2 &= x + n_2 \end{aligned} \tag{2.16}$$

The estimated value of x, denoted as $\hat{x}$, is obtained by combining low pass filtered y_1 readings and high pass filtered y_2 measurements. In frequency domain, let x, $\hat{x}$, y_1, n_1, y_2 and n_2 be denoted as $X(s)$, $\hat{X}(s)$, $Y_1(s)$, $Y_2(s)$, $N_1(s)$ and $N_2(s)$ respectively. Then the frequency domain estimated signal values can be formulated as:

$$\hat{X}(s) = L(s)Y_1(s) + (1 - L(s))Y_2(s) \tag{2.17}$$

Here, $L(s)$ denotes a low pass transfer function and hence $(1 - L(s))$ denotes a high pass transfer function. Using the relations in equation 2.16 to simplify equation 2.17, leads to:

$$\hat{X}(s) = L(s)(X(s) + N_1(s)) + (1 - L(s))(X(s) + N_2(s)) \tag{2.18}$$

$$\hat{X}(s) = X(s) + L(s)N_1(s) + (1 - L(s))N_2(s) \tag{2.19}$$

Equation 2.19 implies that the low pass transfer function $L(s)$ suppresses the high frequency noise $N_1(s)$ and the low frequency noise $N_2(s)$ is suppressed by the complementary high pass filter $(1 - L(s))$, making the estimate $\hat{X}(s)$ equal (approximately) to the true signal value $X(s)$.

Even though the complementary filters are less accurate compared to the Kalman filters, they are much simpler to implement and are computationally more efficient [50].

2.3. Limitations

As discussed, MEMS inertial sensors are cheap and light weight, perfectly suited to MAV applications. However, these sensors are cursed with high noise and inherent drift making deriving accurate attitude estimates a challenge. Sensor fusion algorithms are capable of computing satisfactory estimates of the orientation, but the fact remains that the usage of these algorithms brings about a significant processing burden. Moreover, ideally the roll and pitch angle measurements from accelerometers require a level flight (zero accelerations) condition and otherwise is corrupted with non gravitational accelerations. Magnetometer readings are also corrupted due to the magnetic field induced by other on-board devices and magnetic materials in the vicinity. This reduces the reliability of the attitude estimates obtained by fusing the signals from these sensors (especially while using complementary filters). This makes the integration of alternate sensors (like airspeed sensors for flight speed measurements, GPS for position measurements etc.) necessary for accurate state estimation and control.

Further, the financial and intellectual capital that is invested in MAV development is only justified if the MAVs are able to perform useful tasks such as surveillance, mapping, atmospheric sensing etc. To be able to perform these tasks, MAVs need to be capable of extracting useful information from their environments. Inertial sensors only provide information about the vehicles' ego-motion and do not provide any information about their environment. So, the MAVs require additional exteroceptive sensors (such as chemical sensors, light intensity sensors, laser range sensors, cameras etc.) to be able to interact with their environment. The requirement of integration of extra sensors is always highly undesirable for MAV development. Cameras are the most commonly used exteroceptive sensors in MAVs and act as the eyes of these aerial robots. As will be discussed in the subsequent chapters, natural flyers use their eyes for imagery as well as extracting spatial sense of direction and motion. If the cameras in MAVs could also be used for extracting ego-motion estimates, they might be able to complement the inertial sensor or even replace them.

3

Motion Perception and Navigation Strategies in Insects

Flying insects act as the prime inspiration for researchers working towards development of MAVs capable of efficiently flying in confined indoor spaces. With the ability to fly along longitudinal, lateral and vertical directions, combined with the ability to manoeuvre with high linear and rotational accelerations, insects are capable of out-manoeuvring any human-made flying machine at low flight speeds. This chapter intends to draw inspirations from insects by reviewing their sensing, stability and control strategies.

3.1. Ego-Motion Sensors

The absence of inherent flight stability, in many insects, makes an active feedback control system essential [7]. Insects use feedback from various sensory organs, like the halteres, antennae, ocelli and compound eyes, to stabilize and control their flight. This section summarizes various sensory organs used for ego-motion sensing in insects.

3.1.1. Mechanosensors

Mechanosensors refer to sensory organs that perceive any change in mechanical forces. Various mechanosensors in insects measure the inertial forces, limb and wing loads and orientation, and wind gusts. This section reviews various mechanosensory organs found in insects.

Halteres

In house flies and other dipteran insects, the hind pair of wings has evolved into club shaped organs known as halteres. The halteres vibrate at the wing flapping frequency and, when the insects undergo rotational motion, the halteres experience Coriolis forces, induced by the linear motion of the halteres within the rotating frame of the insects' body. Dickinson [30] demonstrated that the halteres detect these Coriolis forces and use this information to encode the insects' angular rates. Dickinson also indicated that this angular velocity feedback is crucial for insects' flight stability.

Antennae

Antennae are found in almost all insects and serve a variety of different sensory functions in different insects, like air-current sensing organs [51] and chemoreceptors [52]. Sane et al. [53] reported that the antennal mechanosensors play an important role in mediating flight control in hawkmoths, similar to the role halteres play in dipteran insects.

Hair

Insects possess tactile hair in different parts of their bodies, dedicated to different functions. They measure the angles of their appendages' joints (like head, legs, wings and body joints) using clusters of such mechanosensitive hair, called hair plates. As the appendages move, they brush against these hair, and the deformation of the hair encode the relative orientation of the appendages [54]. Wind sensitive hair clusters are also found in insects that measure wind gusts [14].

Cerci

The cerci are cone-shaped appendages, generally extending from the rear of an insect, prominently found in crickets and earwigs. The cerci, instead of being a dedicated sensory organ, houses various sensors. In many species of insects, they are covered with mechanosensitive hair, measuring air-currents. In some insects, the cerci can also include chemosensors. In some crickets and cockroaches, the cerci have club shaped hair that deflect like a pendulum under gravity's pull. These hair are thought to be important for measuring gravity orientation (graviception) in those insects [54]. These hair have been found to be important in cockroaches for flight stabilization [29], however their functions in other insects have not been explored yet [54].

3.1.2. Visual Sensors

Visual information plays an extremely important role in various insect flight behaviours like triggering escape or landing, controlling flight speed and altitude, as well as chasing mates and prey. In some insects about two thirds of all the neurons in the brain contribute to visual information processing [14], which renders vision as the insects' most important sensory modality. Most insects possess two kinds of vision sensors, about one to three ocelli on the dorsal part of the insects' head and a pair of compound eyes.

Ocelli

Ocelli are rudimentary light sensors, which complement the primary vision system in insects: the compound eyes. Typically an adult insect possesses three ocelli, each encoding information about the light levels in the environment. Together the ocellar signals provide information about the insect's orientation changes [55]. Ocelli are believed to function synergistically with the compound eyes to reduce the delay of visual responses [7]. Figure 3.1 depicts the head of a blowfly consisting of a pair of compound eyes along with three ocelli, namely medial ocellus (mo), lateral left ocellus (llo), and lateral right ocellus (rlo).

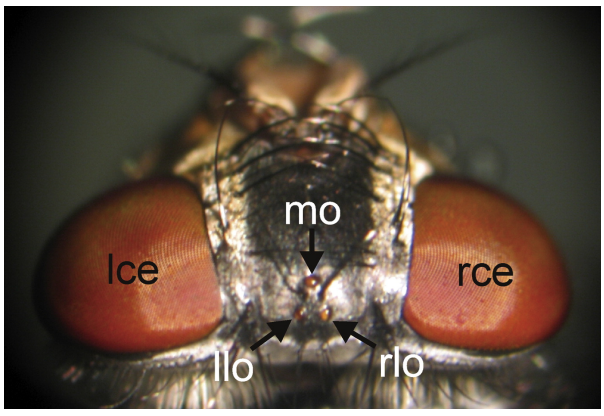

Figure 3.1: Visual sensors on a blowfly : lce and rce respectively denote the left and right compound eyes. The three ocelli of the blowfly, medial, lateral left, and lateral right ocellus, are labelled mo, llo, and rlo respectively. Source: [55]

Compound Eyes

In insects, years of evolution have created a sophisticated vision system known as the compound eyes. Each compound eye is composed of hundreds of individual photoreceptor units, called the ommatidia, arranged on a convex surface. Images received from this convex array of photoreceptors are merged to obtain panoramic vision. Figure 3.1 depicts the two compound eyes on a blowfly, marked lce and rce.

Apart from imagery, the compound eyes also provide the insects with a spatial sense of direction and motion. Each ommatidium functions in conjunction with its closest neighbours to encode image motion, forming the Elementary Motion Detectors (EMDs). A famous theoretical model of the EMD was devised by Bernhard Hassenstein and Werner Reichardt [56]. Figure 3.2 depicts the structure of a simple EMD model. The model consists of two photoreceptors, A (left) and B (right), viewing adjacent regions of the same scene. Now, since the two photoreceptors are viewing the same scene, both will encode the same temporal variation of intensity, however with a certain lead or lag depending on the direction of motion of the scene. Detecting this lead or lag in the photoreceptor signals, with respect to each other, encodes the direction of motion of the scene. A simple way of doing this is to delay the signal from A and correlate it with the signal from B and vice versa. If the delayed signal from A is more strongly correlated with the signal from B, than the delayed signal from B is correlated with the signal from A, it would mean that the signal from A leads the signal from B and hence the scene is moving from A to B. Movement sensitive neurons have been discovered and characterized whose responses are very well estimated by the EMD model discussed above [57]. Thus, these neurons encode the image motion on the insect retina, formally known as Optical Flow (OF) field [15], which helps the insects to perceive ego-motion. Optical flow is essentially the measure of the ratio between the observer's relative movement and distance of the surrounding objects in the environment. A detailed discussion about optical flow, its mathematical formulation, computation techniques and applications in MAV navigation has been presented in Chapter 4.

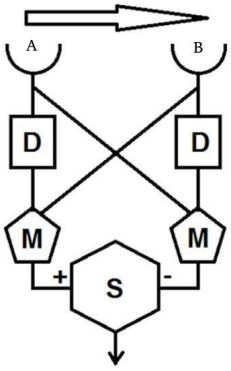

Figure 3.2: The Reichardt EMD model. Source: [58]

3.2. Importance of Optical Flow in Insect Navigation

The sensory organs, discussed in the previous section, play a very important role in insect flight stability and manoeuvrability. The visual and mechanosensory systems are capable of sensing body deviations and enable the insects to provide compensating reactions to maintain a stable flight [7]. However, there is strong evidence that the inertial mechanosensors play a rather less important role than the visual sensors in many insects. This is because the forces transduced by any inertial sensor are proportional to the size of the proof mass whose inertia reacts to the applied accelerations. Size of the proof mass is a limiting factor in a creature as small as an insect. Barring a few exceptions

(like dragonflies[1]) most flying insects do not use organs with static proof masses to measure accelerations [14]. Some insects, that have been found to measure inertial forces in flight (like dipteran flies), make use of organs that use moving proof masses, like the halteres. However, organs like halteres have not been found in some insects like the honeybees. Unlike the inconsistent presence of the inertial sensors in insects, the visual sensors are ubiquitously present in almost all insects. Thus, it can be argued that ego-motion sensed by the visual sensors and the inertial sensors might be redundant and insects rely more on their vision, to perceive ego-motion, than the inertial sensors.

Navigating through a stationary environment, insects perceive the apparent motion of the environment as retinal image shifts, or optical flow, as discussed in the previous section. Analysing the optical flow field allows the insects to estimate ego-motion and use this information for flight control and navigation. This section reviews various flight behaviours observed in insects that reveal the importance of optical flow in insect navigation : 1) the optomotor response, 2) obstacle avoidance and negotiating narrow gaps, 3) visual odometry, 4) regulating flight speed, 5) performing smooth landings 6) altitude control and 7) attitude control.

The Optomotor Response

Reichardt [59] made the observation that a tethered insect, flying inside a stripped drum, tends to execute turns in the direction of the drum's rotation. This response of the insects is called the optomotor response and it has been found to be a behaviour that is common in most flying insects. It serves to help the insects in course stabilization. For example, if a wind gust causes the insect to drift towards the left direction, it would create a rightward retinal image motion and the insect will generate a compensatory yaw torque towards the right direction. The optomotor response also forms the basis of various behaviours observed in insects, discussed in the subsequent sections.

Obstacle Avoidance and Negotiating Small Gaps

Insects demonstrate exceptional capability of gracefully flying through cluttered environments and avoiding obstacles on their flight path. To investigate how the insects gauge and balance their distance from walls and obstacles, Kirchner and Srinivasan [18] trained bees to fly through an apparatus in which each side wall consisted of a pattern of black and white gratings, as depicted in figure 3.3, adapted from [22].

The gratings on one of the side walls could be moved horizontally at any desired speed. When the gratings were held stationary, the bees tended to fly along the mid-line of the tunnel (figure 3.3A). When gratings on one side were moved in the direction of the bees' flight, thus reducing the speed of retinal image motion on the side of the moving grating, relative to the other, the bees' trajectory moved toward the side of the moving grating (figure 3.3B). When the grating was moved in the opposite direction, thus increasing the retinal image velocity on one eye relative to other, the bees shifted their trajectory towards the side of the stationary grating (figure 3.3C). These observations demonstrate that the insects might not be measuring their absolute distances from the walls, and instead might be simply balancing the retinal image speed on both eyes to navigate through small gaps.

Further, experiments were conducted with the two walls carrying gratings of different spatial frequencies. The results obtained were similar to the results obtained when gratings on both sides had the same spatial frequency (figure 3.3D-F). This result demonstrates that the bees indeed balance the retinal image speed of their two eyes and not the contrast frequencies produced by the succession of dark and light bars. The results of the above experiments remained the same irrespective of whether the contrast of the gratings, or their intensity profiles, on the two sides were equal

[1] Dragonflies have a sufficiently large and heavy head, such that the head lags behind the body during angular rotations, thereby allowing the neck tactile hair to measure angular accellerations [14].

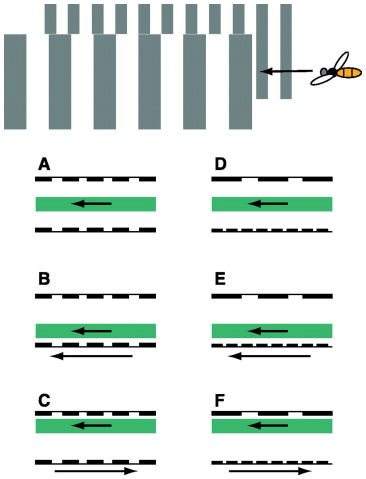

Figure 3.3: Depiction of Kirchner and Srinivasan's experiment [22]. The green shaded bars represent the positions of the flight trajectories recorded over multiple flights. Position of the long axis bar represents the mean flight trajectory position and the width of the bar represents the standard deviation. Arrow beside the wall with gratings denotes the direction of motion of the gratings

or considerably different. Thus indicating that the honeybees are capable of measuring the retinal image velocities robustly and use this information to steer a collision free flight.

Visual Odometry

To investigate how the honeybees perceive the distances they have flown, Srinivasan et al. [60] trained bees to enter a tunnel and collect the reward of sugar solution placed at a fixed distance from the entrance of the tunnel. The tunnel's walls and floor were lined with black and white gratings. The trained bees were then tested in an identical tunnel but with the reward removed. During the tests the bees were observed to search for the reward in the vicinity of the location where the reward was placed during training. This indicated that the bees remembered the position of the reward and hence somehow could measure the distance they had flown during training. When the bees, trained in a tunnel of a given cross section, were tested in a narrower tunnel, they were observed to search for the reward at a shorter distance from the entrance, and when tested in a wider tunnel, they searched at a longer distance. Further, when the textures from the walls and floor of the tunnel were removed by lining the tunnel with axial rather than vertical strips, the bees lost their ability to estimate the distance of the reward. These findings reveal that the bees possess a visually driven odometer that measures the distance flown by integrating the velocity of the retinal image.

Flight Speed Regulation

David [19] investigated how insects measure speed in the absence of acceleration sensing organs. He studied the flight of fruit flies upstream along the axis of a barber's pole wind tunnel. The author named the wind tunnel a barber's pole wind tunnel as the walls of the tunnel were decorated helical black and white stripped pattern. This caused an apparent motion of the pattern when the cylinder was rotated. During the experiments the rotational speed of the tunnel was regulated such that the fly remained stationary. Further, increasing or decreasing the rotational speed of the cylinder caused the fly to move backward or forward (respectively) along the tunnel axis such that the retinal image velocity remained constant. This revealed that the flies were holding the angular velocity of the retinal image constant to regulate their ground speed.

It appears that bees also utilize a similar strategy to regulate their flight speed [60]. This was revealed by observing bees' flight through a tapered tunnel. As the tunnel narrows down, bees tend to decrease their flight speed, thus keeping the retinal velocity of the image of the wall constant.

Further, Portelli et al. [20] also studied vision based flight control in honey bees and reported that the insects control their flight speed based on the optical flow perceived not only in the lateral and ventral parts of their visual field,but also in the dorsal part.

Performing Smooth Landings

Studies of landing behaviour in flies have revealed that in case of approaches perpendicular (or close to perpendicular) to the surface, the expansion of the retinal image of the surface (looming cues), as it is approached, provides strong cues that are used to regulate the descent speed [22]. However, the looming cues are weak, when a bee performs a landing where its angle of approach to the surface is considerably less than 45^o i.e. grazing landings. In such landings, a translational optical flow component in the front to back direction strongly dominates the image motion in the ventral visual field of the insects. Srinivasan et al. [61] observed the trajectories of honeybees landing on a flat horizontal surface and concluded that bees, approaching the surface at relatively shallow descent angles, hold the angular velocity of the image of the surface constant as they approach it. This maintains their forward velocity proportional to their height above the surface. Further, the descent speed is maintained proportional to the forward speed, hence making it proportional to the insects' height above the surface as well. This behaviour ensures that, near touch down, the bees have approximately zero horizontal as well as vertical velocities, making the landings smooth. Based on their observations, the authors derived a model of the trajectory of a honeybee performing grazing landing, as formulated in equation 3.1.

$$V_d(t) = BV_f(t) = B\omega h(t_o)e^{-\omega B(t-t_o)} \tag{3.1}$$

Where, V_d denotes the descent velocity, V_f denotes the forward velocity, B is the constant of proportionality between V_f and V_d, $\hat{\omega}$ denotes the constant angular velocity of the image of the surface and $h(t_o)$ denotes the height at initial time $t = t_o$. In a later study Chahl et al. [62] implemented the above model to control the descent of a fixed wing model aircraft, as will be discussed in section 4.4.1.

The task of landing becomes a bit more complicated when the surface is not horizontal, i.e. the landing surface inclination increases. Baird et al. [63] analysed trajectories of honeybees landing on a vertical surface and found that the bees control their speed by holding the rate of expansion of the image constant. This strategy is also applicable to landings on horizontal flat surfaces. The strategy has been used for autonomous landing of MAVs , as discussed in section 4.4.1.

Altitude Control

Portelli et al. [21] studied the altitude control behaviour in honeybees, trained to fly in a double roofed tunnel[2] after entering it near either the ceiling or the floor of the tunnel. The honeybees, entering the tunnel near the ceiling and the floor, flew forward hugging the ceiling and the floor respectively. Thus, midway through the tunnel, the bees hugging the ceiling experienced a sudden change in their distance from the tunnel ceiling. The bees reacted by increasing their altitude and quickly hugging the new higher ceiling, thus keeping the optical flow in their dorsal field of view constant. However, the bees entering the tunnel near the floor kept hugging the floor and did not react to the ceiling height change. Further, when the bees trained to hug the ceiling were made to enter the tunnel near the floor and vice versa, the bees quickly changed their altitude to hug the surface they had been trained to follow. This study shows that trained honey bees regulated their altitude based on the visual cues (optical flow patters) memorized during training.

[2] the height of the tunnel ceiling increased midway through the tunnel

Attitude Control

Insects' ability to perform highly demanding manoeuvres, requires the ability to accurately control their orientation. Many animals use gravity as a cue to maintain the up-right orientation of their body. In insects walking on the ground, gravity perception, through gravity sensitive tactile hair on cerci and limb load cues, has been found to play a significant role in gaze stabilization and body tilt compensation [29, 54]. During flight however, insects experience high accelerations, due to forces like air drag, making it very difficult to distinguish these forces from gravity. Unlike vertebrates, that have specialized organs in the vestibular system that measure accelerations, many insects lack organs that measure accelerations using a static proof mass, often attributed to the insects' diminutive stature. Halteres use a moving proof of mass to detect Coriolis forces and hence encode rotational rates, however, it is still debatable if the halteres are capable of encoding rotational accelerations [14]. Lacking well defined acceleration measuring organs, it becomes a question as to how the insects estimate and stabilize their attitude and whether gravity perception plays a major role in it. Goulard et al.[29] subjected hoverflies to freefall and studied how the insects coped with weightlessness under different visual conditions. Figure 3.4 shows the experimental apparatus and the trajectories of various hoverflies subjected to free fall, in total darkness, in a nearly uniform white environment and with two sides of the box lined with horizontal black and white strips. Falling in darkness resulted in a large number of crashes, however in presence of vertical strips almost all the hoverflies initiated wingbeats and generated large enough thrust to avoid crashing. Though, wingbeats were also initiated in total darkness, indicating that the free fall was perceived and hence involvement of other sensory modalities may not be ruled out. The authors however suggested that it is unlikely that load cues from the insects' dangling legs were used to detect free fall, instead sensing airflow generated by self-motion while falling, led to the perception of free fall. The authors concluded that the crash avoidance performance of the insects suggests the existence of a multisensory control system, depending mainly on vision rather than gravity perception or inertial sensing.

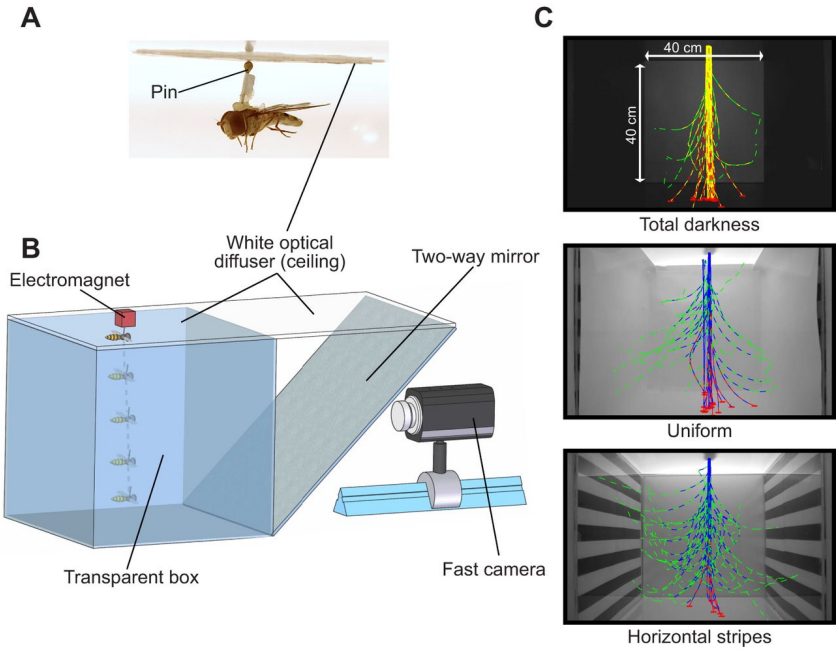

Figure 3.4: Experimental apparatus used to study the flight behaviour of hoverflies subjected to free fall. Source [29]

The secondary visual sensors, namely the ocelli, that serve as fast and ultra-sensitive horizon detectors, through their triangulation orientation permit the detection of horizon tilt along two axes. The ocelli appear to contribute to phasic dorsal light responses (DLR) that compensates for attitude changes imposed by fast head and body movements [14]. Thus the ocelli play a major role in

complementing the compound eyes in attitude stabilization of the insects and contribute towards reducing the latency of visual responses in insects [7].

3.3. Inspirations for Roboticists

Tiny flying insects, appearing in the nature, have a lot to teach to roboticists and researchers striving to make MAVs as nimble as the insects. Insects depend on a high modality sensory feedback control system to stabilize their flight and perform remarkable manoeuvres. The sensory organs involved in attitude estimation can be categorized as the inertial mechanosensors like the halteres, antennae, tactile hair and gravity sensitive pendulous hair on the cerci, and visual sensors like the ocelli and compound eyes [7]. Evidently, the visual sensors play a more important role in insect flight stabilization than the inertial sensors. Some insects, like the cockroaches possess gravity sensitive organs, however many other insects lack acceleration measuring apparatus [14]. Rotational rate measuring halteres are found in dipteran insects, however many other insects like the honeybees and other hymenopteran flying insects do not have any organs that have yet been identified to measure their rotation rates and orientation [22]. Thus the question arises, if some insects completely lack the inertial sense and only depend on vision for flight stability and control. Attitude estimation in insects is yet to be properly understood, but it is quite possible that the information encoded by the inertial sensory organs are redundant and the ego-motion information encoded by the visual sensors might be enough for flight stabilization. This hypothesis, if true would have great implications in the field of robotics. It would mean that flight stabilization can be achieved by only using suitable optical sensors encoding optical flow information. This thesis intends to contribute towards testing this hypothesis. The next chapter discusses the notion of optical flow in further detail and reviews various optical flow based MAV navigation strategies available in literature.

4

Optical Flow

Optical Flow or Optic Flow is the pattern of apparent motion of the elements of a visual scene caused by relative motion between the observer and the scene. As described in the previous chapter, natural fliers use optical flow for efficient flight control and stabilization. Inspired by the biological navigation models, several researchers have attempted to use optical flow for ego-motion estimation and state reconstruction of Micro Aerial Vehicles (MAVs). This chapter provides a detailed introduction to the field of optical flow.

4.1. Modelling Optical Flow

James J. Gibson pointed out that the deformation of the retinal image due to ego-motion was not just a nuisance but a rich source of information concerning the world in which the motion occurs [15]. Imagine the visual field of a pilot flying above a runway. Each point in the pilot's retinal image is the projection of the objects in the three-dimensional world onto a two-dimensional image surface (retinal surface). When the pilot moves relative to her environment, the points in her retinal image shift as well. This image motion can be described by a velocity field, or optical flow field, where each velocity vector points in the direction of motion of the corresponding image point and the length of the vector is proportional to the magnitude of velocity of the image point. As presented in [15], figure 4.1 depicts the optical flow field perceived a pilot (a) looking in the forward direction while performing a flyby over a runway, (b) looking forward while approaching the runway during landing and (c) looking in the right direction while performing a fly by over a runway.

The mathematical modelling of optical flow requires projecting points in 3-dimensional world on a 2-dimensional image plane. This section describes two frequently used formulations of optical flow, where the first formulation (section 4.1.1) uses a perspective projection method and the second formulation (section 4.1.2) uses a spherical projection method.

4.1.1. Formulation using Pinhole Camera Model

This camera model is used for the formulation of perspective projection, where world points are projected on a 2-D image plane. The model makes two important assumptions: 1) The camera aperture is assumed to be a point (pin hole) and 2) the image plane is assumed to be a planar surface. One of the most frequently used formulations of this model is that of Longuet-Higgins and Prazdny [17].

As depicted in figure 4.2, consider a monocular observer moving through a static environment with translational velocities, (U,V,W), and angular velocities, (A,B,C), relative to the scene. Let O be the instantaneous position of the observer's nodal point, or vantage point, where the aperture of the camera is defined, and $OXYZ$ be a Cartesian coordinate system centred and fixed at O. Let

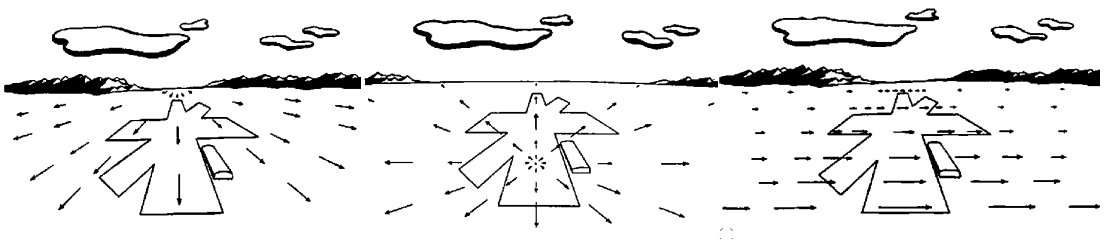

(a) (b) (c)

Figure 4.1: Optical flow field observed by a pilot (a) looking in the forward direction while performing a flyby over a runway, (b) looking forward while approaching a runway during landing and (c) looking in the right direction while performing a fly by over a runway. Source : [15]

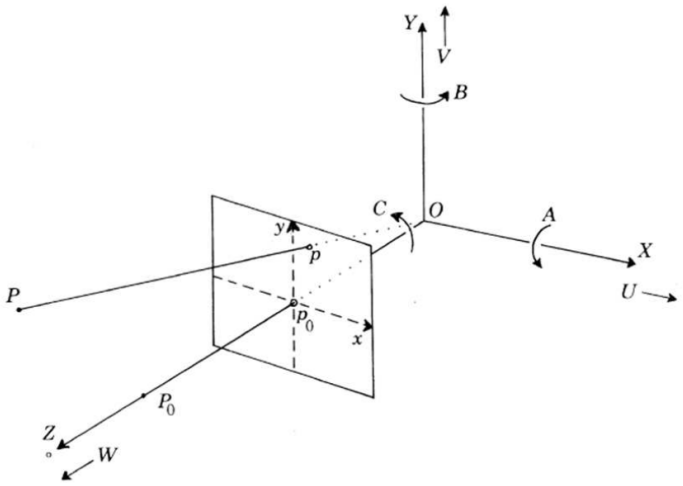

Figure 4.2: Coordinate system depicting perspective projection. Source: [17]

the Z-axis be aligned along the observer's line of sight or the optical axis. The image plane or the retinal surface, perpendicular to the optical axis (OZ), is denoted by the $\hat{x}$ and $\hat{y}$ axes. The optical axis intersects the image plane at the principal point, denoted by $p_o = (0,0,f)^T$. f represents the focal length of the sensor. We consider $f = 1$ to simplify the derivation.

The components of velocity of the world point P, with respect to the moving frame $OXYZ$ are formulated as :

$$\begin{aligned} \dot{X} &= -U - BZ + CY \\ \dot{Y} &= -V - CX + AZ \\ \dot{Z} &= -W - AY + BX \end{aligned} \tag{4.1}$$

Now, as evident from figure 4.2, the world point P can be projected on the image plane to the point $p = (\hat{x}, \hat{y})^T = (X/Z, Y/Z)^T$. As the observer is moving, the projected point p will also move with velocity components $(\hat{u}, \hat{v})^T = (\dot{\hat{x}}, \dot{\hat{y}})$. These velocity components, or optical flow components, can be related to the observer's velocity and the depth of the world point P as :

$$\begin{aligned} \hat{u} &= \frac{\dot{X}}{Z} - \frac{X\dot{Z}}{Z^2} = (-\frac{U}{Z} - B + C\hat{y}) - \hat{x}(-\frac{W}{Z} - A\hat{y} + B\hat{x}) \\ \hat{v} &= \frac{\dot{Y}}{Z} - \frac{Y\dot{Z}}{Z^2} = (-\frac{V}{Z} - C\hat{x} + A) - \hat{y}(-\frac{W}{Z} - A\hat{y} + B\hat{x}) \end{aligned} \tag{4.2}$$

Velocities $\hat{u}$ and $\hat{v}$, as given by equation 4.2, can also resolved into separate translational and rotational components, as :

$$\begin{aligned} \hat{u} &= \hat{u}^T + \hat{u}^R & & \hat{v} = \hat{v}^T + \hat{v}^R \\ \hat{u}^T &= (-U + \hat{x}W)/Z & , & \hat{v}^T = (-V + \hat{y}W)/Z \\ \hat{u}^R &= -B + C\hat{y} + A\hat{x}\hat{y} - B\hat{x}^2 & & \hat{v}^R = -C\hat{x} + A + A\hat{y}^2 - B\hat{x}\hat{y} \end{aligned} \tag{4.3}$$

Where, $\hat{u}^T$ and $\hat{v}^T$ denote the optical flow components due to observer's translational motion and $\hat{u}^R$ and $\hat{v}^R$ denote the optical flow components due to the observer's rotational motion. It is interesting to note that the translational component of optical flow is independent of observer's angular velocity (A, B, C) and the rotational component of optical flow is independent of the three-dimensional structure of the scene.

4.1.2. Formulation using Spherical Camera Model

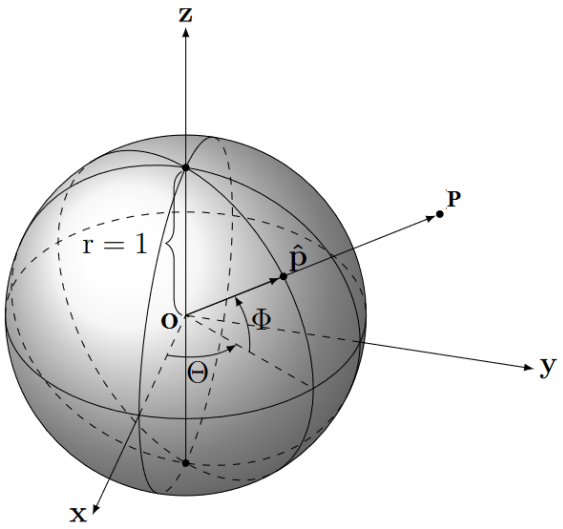

Figure 4.3: Coordinate system depicting spherical camera projection. Source: [64]

The assumptions used by pinhole camera model are not valid when using wide field of view cameras. In such cases a more general model, namely the spherical camera model is utilized. The spherical camera model involves projecting a world point onto a spherical image surface. As depicted in figure 4.3, consider a monocular observer, with it's vantage point at O, moving through a static environment described by the spherical coordinates (R, Θ, Ψ) centred at O. Let the translational velocity vector and the rotational velocity vector, of the observer, be denoted by **T** and **R** respectively. The image surface is a spherical surface centred at O and has a radius $f = 1$. The world point $P = \mathbf{P}$ is projected to the corresponding image point $p = \hat{\mathbf{p}} = \mathbf{P}/||\mathbf{P}||$. Now, as formulated by Koenderink and van Doorn [16], the velocity of the image point, as the observer moves is given by :

$$\hat{\mathbf{v}} = \frac{1}{||\mathbf{P}||}[(\mathbf{T}.\hat{\mathbf{p}})\hat{\mathbf{p}} - \mathbf{T}] - \mathbf{R} \times \hat{\mathbf{p}} \tag{4.4}$$

Which can also be written as :

$$\begin{aligned} \hat{\mathbf{v}} &= \hat{\mathbf{v}}^R + \hat{\mathbf{v}}^T \\ \hat{\mathbf{v}}^T &= \frac{1}{||\mathbf{P}||}[(\mathbf{T}.\hat{\mathbf{p}})\hat{\mathbf{p}} - \mathbf{T}] \\ \hat{\mathbf{v}}^R &= \mathbf{R} \times \hat{\mathbf{p}} \end{aligned} \tag{4.5}$$

Where, $\hat{\mathbf{v}}^T$ denotes the image velocity component due to the observer's translational motion and $\hat{\mathbf{v}}^R$ denotes the image velocity component due to the observer's rotational motion. So, as we could do in the case of perspective projection (equation 4.3), we can again write the optical flow vector as a linear combination of optical flow vectors that would have been caused by separate translation and rotation of the observer (equation 4.5). Moreover, similar to what was observed in equation 4.3, the translational optical flow component is independent of the observer's angular velocity and the rotational optical flow component is independent of the three-dimensional structure of the environment.

4.2. Optical Flow Estimation

So far in this chapter, the concept of optical flow has been introduced and it's mathematical formulation has been described. Equations 4.2 and 4.4 relate the optical flow field to the observer's ego-motion and the three dimensional structure of the scene. So, to be able to derive information about motion and scene structure, the first step is to estimate the optical flow vectors. This section serves to provide an overview of various optical flow estimation techniques. Optical flow estimation involves using the time varying image intensity, captured using an optical flow sensor, to compute an approximation to the image motion field. A common starting point for most optical flow estimation techniques is the assumption that the intensity patterns in the local time varying image regions remain approximately constant under motion at least for a short time duration [65]. Mathematically this can be formulated as:

$$I(\mathbf{x}, t) \approx I(\mathbf{x} + \delta\mathbf{x}, t + \delta t) \tag{4.6}$$

Where, $I(\mathbf{x}, t)$ is the image intensity function, $\delta\mathbf{x}$ is the displacement of local image region at $(\mathbf{x}, t)$ in time duration δt. Now expanding the right hand side of equation 4.6 using Taylor series expansion, ignoring the terms of order O^2 and higher, and rearranging the equation yields an expression popularly known as the brightness constancy constraint.

$$\nabla I.\hat{\mathbf{v}} + I_t = 0 \tag{4.7}$$

Where, $\hat{\mathbf{v}}$ denotes the image velocity, $\nabla I = (I_x, I_y)^T$ and I_t are the first order derivatives of the image intensity function.

However, the brightness constancy constraint is not sufficient to compute both components of $\hat{\mathbf{v}}$ as the equation 4.7 is ill poised[1]. This implies that the velocity component perpendicular to the direction of local gradient of image intensity function, can not be estimated. This phenomenon is called the aperture problem [66]. Only at the image location where there is sufficient intensity structure can the image velocity components be fully estimated using the constraint equation [67].

[1] The constraint has one linear equation and two unknowns, as $\hat{\mathbf{v}} = (\hat{u}, \hat{v})$.

For example, consider the figure 4.4. Through apertures A and B, motion is estimated to be along the normal direction of the edges. Thus the motion of the object is not correctly perceived through apertures A and B. However, through aperture C, motion can be fully estimated, since it is computed at a corner point where there is sufficient local intensity structure, i.e. intensity gradient is visible in two linearly independent spatial directions. For this reason, many optical flow estimation techniques implement, as a first step of computation, a corner detector such as the popular Harris [68] and FAST [69] corner detection algorithms.

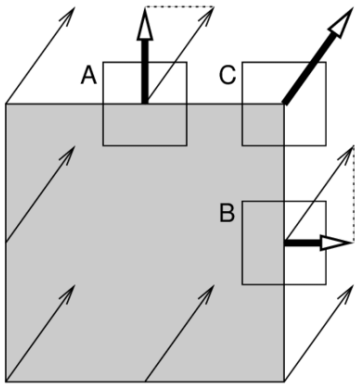

Figure 4.4: Illustration of the aperture problem occurring with a square shaped object in motion. A, B and C denote the three apertures, the thin arrows represent the direction of motion of the object and the thick arrows represent the direction of image motion perceived through the respective apertures. Source: [70]

In the following parts of this section two popular classes of optical flow detection algorithms, gradient based methods and correlation based methods, have been briefly reviewed.

4.2.1. Gradient based Methods

Gradient based optical flow estimation techniques employ the spatio-temporal derivatives of the image intensity function in conjunction with the brightness constancy assumption to estimate the optical flow field. The gradient based methods can be further categorized into local and global approaches depending on whether the algorithm is implemented in small local regions of the image or on the image as a whole.

The local gradient based estimation techniques are employed within small local neighbourhoods of the image to estimate the local optical flow vectors. The Lucas Kanade optical flow estimation method, introduced in 1981 by B. Lucas and T. Kanade [71], despite being about four decades old, is still the most widely used optical flow estimation algorithm. The method addresses the aperture problem of equation 4.7, by aiding it with the assumption that the velocity components, $\hat{u}$ and $\hat{v}$ are constant within a small neighbourhood of a point in an image. For example, if two points within a small neighbourhood in an image are considered with the above stated assumption, the brightness constancy criteria would yield two linear equations with two unknowns, hence a solvable system. The Lucas-Kanade technique obtains an overdetermined system of equations by considering more than two neighbouring pixels. The local optical flow components are then estimated using ordinary least squares. This also forms the basis from which most other techniques of this class are derived [72, 73].

The global gradient based optical flow computation methods use a global smoothness condition to compute a dense flow field over the whole image, instead of computing local flow vectors. One such energy function was introduced by Horn and Schunck [65] :

$$E(\hat{\mathbf{v}}) = \int [(\nabla I.\hat{\mathbf{v}} + I_t)^2 + \lambda(||\nabla \hat{u}||^2 + ||\nabla \hat{v}||^2)]dxdy \tag{4.8}$$

Here λ is a regularization constraint, that denotes the influence of the spatial smoothness term. Some other works in the domain of global gradient based methods include [67, 74]. The key advantage that global methods pose over the local methods is the information flow over large distances in the image [75]. Local methods encounter a singular system of equations in case of lack of intensity patterns, like for image regions containing a blank wall. Global methods on the other hand can fill in the optical flow information from nearby gradient constraints. However, the global methods suffer from poor computational efficiency, due to their iterative optimization process. So, the global methods are rarely used in applications requiring real-time computation of optical flow, like in MAVs.

4.2.2. Correlation based Methods

The correlation based matching approaches involve estimating the displacement (as an approximation of velocity) of an image patch that yields the best match (correlation) between the image patch in two consecutive frames. Matching image regions often amounts to maximizing a similarity measure, such as the normalized cross-correlation [76] and sum of squared difference (SSD) [77] of intensity values. Correlation based methods do not rely on presence of significant image features [67], generally do not suffer from the aperture problem and tend to be robust to random noise [78].

However, these methods have a major drawback: their time complexity grows quadratically with the maximum number of possible displacements allowed for the pixels. Inspired by this problem, Camus [78] proposed an alternative approach that performs the region matching in a spatio-temporal search space, thus keeping time complexity linear in number of possible displacements of the pixel.

4.3. Optical Flow Sensors

Very small conventional cameras are a frequently used sensor system for optical flow computation. For instance, Wagter et al. [79] introduced a 4 grams stereo camera with an embedded microprocessor (figure 4.5A). The maximum reachable frame rate of the stereo camera system is 30 Hz. This system has been used in [27, 80] for stereo-vision and optical flow based velocity estimation in pocket drones. de Croon in [37] introduced a monocular distance estimation method using optical flow manoeuvres and the knowledge of control inputs. The downward facing camera on a parrot AR drone was used for this study. However, generally the frame rate of these cameras are low which makes the update rate of optical flow information slow. Moreover a vast amount of effort has to be made in making processing more efficient.

Conventional cameras perceive the environment as a series of consecutive frames of images generated by capturing the pixel values at fixed time intervals. But unlike conventional cameras, the event based vision sensors capture the changes in perceived brightness by generating events. Accordingly, the outputs of these sensors are streams of events that encode variations in image intensity at a particular time and location on the image plane. Thus the event based cameras eliminate the enormous amounts of redundant information contained in the frames captured by the conventional cameras. The Dynamic Vision Sensor (DVS) is an event-based vision sensor, designed by Lichtsteiner et al. [82] and commercialized by iniLabs[2] under the product names of DVS128 (figure 4.5B), eDVS, Mini-eDVS and DAVIS240C. However, with DVS128 weighing 65 grams without lens and the Mini-eDVS weighing 5 grams (with lens), these sensors are still quite heavy to be used in small MAVs, especially in FWMAVs.

[2] https://inilabs.com/

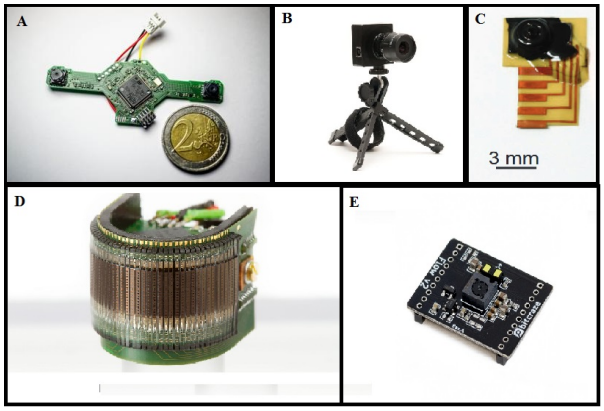

Figure 4.5: Optical flow sensors. A) 4 gram Stereoboard beside a 2 Euro coin. Source:[79], B) Dynamic Vision Sensor DVS128. Source: https://inilabs.com/, C) Centeye TAM4 integrated on a flex circuit breakout with a lens. Source: [81], D) Cylindrical CURved Artificial Compound Eye CURVACE. Source: http://curvace.org/, E) Optical mouse sensor based Bitcraze's Flow deck v2 optical flow sensor. Source: https://www.bitcraze.io/

In the pursuit of small, lightweight optical sensors, some researchers have also used custom made lightweight optical chips. Centeye[3] developed the image chip called TAM 4 (figure 4.5C) that has been used for altitude sensing in RoboBee [81]. One of Centeye's latest works is the Centeye Multi-Mode Stereo Sensor, sporting two RockCreek vision chips, IR lights for illumination and a laser light (that can be used for range sensing). The sensor has a 150^o FOV and weighs 1 gram.

Inspired by the robustness and efficiency of the biological ego-motion estimation methods, Franceschini et al. [83] built optronic velocity sensors, whose principle of operation is based on fly EMDs. Ruffier and Franceschini[24, 84] have used these EMD based sensors to demonstrate the applications of optical flow regulation for guidance and control of a tethered MAV platform. Another bio-inspired approach has been the fabrication of the CURved Artificial Compound Eye, CURVACE (figure 4.5D), that outputs a video stream with a Field of View (FoV) of $180^o \times 60^o$ [85]. It consists of 630 artificial ommatidia, which are photo-detectors similar to the ommatidia found in insect compound eyes. It is capable of delivering 1950 frames per second (fps) output and weighs 1.75 grams.

A widely used method is using the dedicated optical flow sensory chips, found in optical computer mice [86, 87](figure 4.5E). These chips consist of a tiny built in camera and hardware dedicated to computation of a single 2 dimensional optical flow vector. These sensors are generally fast and are available in cheap packages. However, their performance highly depends on illumination conditions and available contrast.

4.4. Optical Flow based MAV Navigation

In chapter 3, insect navigation behaviours were studied and contribution of optical flow in making flying insects nimble was discussed. Inspired by insect navigation, optical flow has been widely used in MAV navigation by various researchers. This section discusses various optical flow based strategies that have been proposed and utilized for MAV navigation. Table 4.1 in Section 4.4.5 summarizes the works that are being discussed in this section and highlights the knowledge gaps.

4.4.1. Landing

Grazing Landing

To the best knowledge of the author, Chahl et al. [62] presented the first vision based MAV navigation strategy implementation in which ventral optical flow components were used. The optical

[3]http://www.centeye.com/

flow, measured using a downward facing camera, was maintained constant to control the descent of a fixed wing MAV, in accordance to the model of landing honeybee trajectory derived by Srinivasan et al. [61] (equation 3.1 in section 3.2). According to the model, the forward speed and the descent speed of the MAV were maintained proportional to the height of the MAV. Though the authors could not land the aircraft using this approach, due to a finite stall speed of the aircraft, their results demonstrated the potential of the method in achieving smooth landings. In a similar study, Green et al. [23] implemented the strategy on a fixed wing MAV and demonstrated successful landings.

In further studies Ruffier and Franceschini [24] and Franceschini et al. [88] explored regulation of ventral optical flow in their autopilot OCTAVE (Optical flow based Control sysTem for Aerial Vehicles) to enable a tethered rotorcraft to perform terrain following, automatic take off and automatic landing. The experimental MAV manoeuvred with 2DoFs: pitch angle and the magnitude of thrust vector. Landing was performed by reducing the forward speed of the MAV (which remained proportional to the MAV's height) by slowly pitching up the MAV. Ruffier and Franceschini [84] further extended their work to demonstrate terrain following and landing over a moving platform.

Since the landing strategy maintains the horizontal velocity of the MAV proportional to its height, it is not possible to independently control the vertical dynamics. Thus, the strategy reduces the flight envelope of certain MAVs, as hovering and pure vertical motion, which are the key advantages of rotorcraft MAVs, become impossible.

Vertical Landing

As discussed in section 3.2, Baird et al. [63] showed that insects maintain the divergence of the image constant while landing on a vertical surface. This is a more general strategy and applies to landings on horizontal surfaces with shallow descent angles, i.e. grazing landings, as well. But now the vertical and horizontal motions become independent of each other and hence this navigation strategy can be applied in rotorcraft MAVs without limiting their flight capabilities.

Herissé et al. [89] demonstrated the application of constant divergence strategy to hover and land a vertical take-off and landing (VTOL) MAV on a moving platform. Ho and de Croon [90] worked on characterization of divergence estimated with a downward facing monocular camera on a MAV during a constant divergence landing manoeuvre. The results showed that as the MAV approaches the landing surface, the controller becomes unstable because of significant oscillations generated in the estimated divergence due to noise and delays. Instead of regarding this as a problem, de Croon [37] showed that for a specific gain, optical flow control becomes unstable at a specific height above the landing surface. And so the author proposed that the MAV can detect oncoming self-induced oscillations and use these for estimating the height. Further, Ho et al. [25] used this theory to demonstrate a constant flow divergence landing control strategy. The strategy starts with increasing the MAV control gain to induce oscillations, thus detecting the height and a suitable starting gain. The MAV then descents while reducing its control gain exponentially, thus achieving smooth landings.

4.4.2. Obstacle Avoidance

Tammero et al. [91] showed that fruit flies turn away from regions with high optical flow, thus avoiding obstacles. Similar bio-inspired strategies have been widely adopted by researchers for obstacle avoidance in MAVs.

Iida [92] implemented this strategy to perform course stabilization and obstacle avoidance in a blimp like flying robot. Images captured through a panoramic vision system were processed on a host computer, to detect the image motion through bio-inspired correlation based detectors, called

the Elementary Motion Detectors (EMDs). The panoramic vision system provides a visual field of $360^o \times 260^o$ and separate two dimensional arrays of EMDs were implemented on the left and right visual fields, to extract motion information, both in horizontal and vertical directions. Obstacles were avoided by turning the MAV away from the side on which the integrated large field EMD registered higher activation, i.e. higher image motion speed. An advantage of using EMDs to extract motion information is that it does not require computationally expensive feature tracking. Green et al. [23] also used EMDs to perform collision avoidance on a 26 grams fixed wing MAV. The authors used a Centeye developed VLSI optic flow sensor, Ladybug, that detects image motion based on EMD circuitry. In the study, the authors assumed the rotational component of optical flow to be small and used the optical flow readings from the sensor as translational optical flow. However, it remains unclear if this was an apt approximation for the experiments considered in the study.

Zufferey and Floreano [26] implemented optical flow based obstacle avoidance in a 30 grams fixed wing MAV. They used two linear cameras to measure frontal and lateral optical flow, and yaw rates from a rate gyroscope were used to eliminate the rotational component of the optical flow. Obstacles were avoided by initiating a turn once the divergence of the detected optical flow exceeded a set threshold and the direction of the turn was decided by taking the difference of the optical flows detected through the left and right cameras. Beyeler et al. [33] presented a flight control system, optiFlow, for autonomous control of a flying wing MAV in cluttered environments. An airflow sensor was used for controlling the flight speed and the effects of rotations on the optical flow measurements were compensated using a rate gyroscope. Further, assuming a constant speed, the authors derived a control strategy that used optical flow measurements to calculate the pitch and roll control commands while accounting for the obstacle proximities in various viewing directions.

The works discussed so far implement a sensory-motor control strategy where obstacles were avoided by directly using the optical flow sensor measurements as the primary input, to derive the control signals, without estimating the metric depth or distance to the obstacles. These methods however, can only be applied in special environments and might fail in unknown cluttered environments. Zingg et al. [93] used an optical flow based approach to obtain a depth map of the surroundings of a quadrotor navigating through an indoor corridor. The computed depth map was then used to maintain the quadrotor at the centre of the corridor, hence avoiding the walls. A depth estimation based obstacle avoidance method might be more viable in complex indoor environments, however, depth can only be estimated from the translational component of optical flow, thus requiring compensation of the rotational effects using IMU data. This makes the approach heavily reliant on the accuracy of the IMU data, as evident from the test results reported by the authors [93].

4.4.3. Velocity Control

Insects have been known to regulate optical flow for flight speed control [19, 60], as was discussed in Section 3.2. Following a similar bio-inspired approach, Serres et al. [94] presented LORA III (Lateral Optic flow Regulation Autopilot, Mark III), which is a dual optical flow regulator consisting of two intertwined feedback loops, controlling a MAV's forward and lateral velocities. The MAV used is a miniature hovercraft, equipped with two EMD optical flow sensors measuring the lateral optical flow at the sides, at an angle of $\pm 90^o$. Lateral thrust (which determines the lateral speed) is controlled by regulating the lateral optical flow, measured on the side closer to the wall, to be equal to a fixed setpoint. This ensures that the distance of the MAV from the nearest wall becomes proportional to the vehicle's forward velocity. The forward velocity is controlled by regulating the sum of the optical flow measurements on the two sides to a fixed set-point. Thus the LORA III autopilot enables the MAV to control its cruise speed and avoid lateral obstacles. Moore et al. [95] implemented an optical flow based approach on a 30 grams helicopter equipped with a 2.6 grams vision system consisting of a ring of eight vision chips. Velocity control was performed by controlling the forward thrust based on the total sum of observed translational optical flow. Further, the authors also uti-

lized optical flow to perform corridor centring and collision avoidance. However, it can be pointed out that though a single camera is capable of detecting motion in three directions, the authors are using eight cameras to detect motion in only two directions, forward and sideways, thus there is further scope of reducing the sensor redundancy and hence the MAV weight.

Apart from sensory-motor approaches to velocity control, some researchers have also studied metric velocity estimation in MAVs using optical flow. Kimberly et al. [27] presented an efficient vision algorithm called Edge-FS (Edge Flow and Edge Stereo) for velocity and depth estimation in a Pocket Drone equipped with a forward facing 4 grams stereo camera board. The authors used an edge histogram matching approach to compute optical flow (Edge Flow) and stereo disparity (Edge Stereo). The stereo disparity estimates depth which was used to scale the velocity estimates computed using Edge Flow and to detect the distance to the nearest object for obstacle avoidance. So, metric velocity estimation requires the estimation of depth which can be done using a stereo vision system as in [27], or a range measurement sensor like a laser range finder. This dependency on an additional sensor is clearly a disadvantage for MAV applications.

The problems of the missing scale factor, for metric velocity estimation using optical flow, and position drift due to error accumulation over time (by integrating the erroneous velocity estimates), were considered by Briod et al. [28], where the authors used optical flow to aid inertial sensors for ego-motion estimation and control of a 46 grams quadcopter. The introduced method used translation induced optical flow's direction (which is independent of depth and hence the environment) to define a constraint on the velocity vector, which the authors call TOFDC (Translation Optic-Flow Direction Constraint). This constraint is used to compensate for inertial navigation velocity drift, thus obtaining velocity estimates with higher confidence.

4.4.4. Attitude Stabilization

Effective attitude stabilization requires accurate attitude estimation. Optical flow, as already discussed, encodes ego-motion information and hence might have the potential to replace or augment inertial measurements for attitude estimation. Omari and Ducard [31] presented a state estimation framework that allows estimation of attitude, full metric velocity and orthogonal distance from a wall, of a MAV equipped with an IMU-camera navigation system. The method uses an UKF (Unscented Kalman Filter) to fuse optical flow measurements, of a single feature observed using a spherical camera, with gyroscope and accelerometer measurements. The full observability of the system states, however, depends on various conditions, like excitation of the platform with accelerations along two independent axes and non alignment of the optical flow feature vector with the body frame velocity vector of the platform. The observability limitations of the approach could be improved by including the vehicle dynamics into the state estimation problem. Verveld et al. [32] studied the observability of vehicle motion states using six orthogonal optical computer mouse sensors. The six sensor configuration was not enough to obtain full observability, and required augmentation using a 3-axis accelerometer. The authors introduced a HKF (Hybrid Kalman Filter) which combines steps of UKF with IEKF (Iterated Extended Kalman Filter). The approach was tested in simulation and experiment where a tethered sensor setup was made to oscillate like a pendulum and its motion states were estimated. The results indicated that the system was capable of estimating the states in favourable lighting conditions and in presence of enough motion. The study reveals various limitations of the approach, first being the diminishing observability with the lack of motion due to low optical flow input and the other being the use of multiple optical sensors. The need of using multiple optical flow sensors arises from the fact that each of these sensors measures optical flow in a very limited FOV, since local optical flow measurements from a single sensor can have the same value for different motion patterns. The use of a sensor with wide FOV could therefore reveal more information with less number of redundant sensors. Zhang et al. [96] demonstrated attitude estimation in a tethered 3-DoF helicopter based only on optical flow measurements using a single

camera. The authors used a gradient descent algorithm to obtain the angular rates from the set of six non linear equations (relating optical flow vectors to the platform angular rates and environment structure) obtained at three image corner points. Then the attitude of the platform was computed by integrating the angular rates. However, to be applied on a free flying MAV, the approach would require integration of inertial sensors as direct integration of the noisy angular rates obtained by solving the optical flow equations might lead to attitude drift.

Various researchers have also attempted to implement reactive sensory-motor control strategies for attitude stabilization using optical flow. The optiPilot [33] (discussed in Section 4.4.2) was demonstrated to be able to effectively reject roll and pitch perturbations and stabilize the flight of a neutrally stable flying wing MAV. Goosen [34] proposed an optical flow based system (Figure 4.6) for flight stabilization and control of flapping wing MAV. The system uses six orthogonal optical computer mouse sensors, facing in $X\pm$, $Y\pm$ and $Z\pm$ directions. Each of these sensors measures a single optical flow vector in two directions, which are used to drive the control actuators in the wings and the main flapping actuator. The concept was tested in simulation and experiment by Selvan [97] and van Vrede[39]. Implementation on a tethered 3-DOF bi-copter [39] revealed that stabilization based on rotational, horizontal and vertical feedback was possible using on-board processing on a simple micro-controller. However, the author reported poor control performance in trajectory tracking, which is reasoned to be due to the use of proportional velocity feedback. The author also concludes that the performance of such an approach on a free flying MAV would significantly depend on the quality of optical flow sensor used. Use of optical mouse sensors is not particularly ideal due to its sensitivity to lighting conditions and limited FoV requiring integration of multiple sensors (as discussed earlier in this section). The performance of the approach on a highly vibrating platform such as a flapping wing MAV is also uncertain and would be interesting to be evaluated.

Despite the works reported in this section, optical flow based attitude estimation and stabilization of a free flying MAV remains to be a research problem that is largely unexplored (as apparent from table 4.1) and hence an interesting topic for the current study.

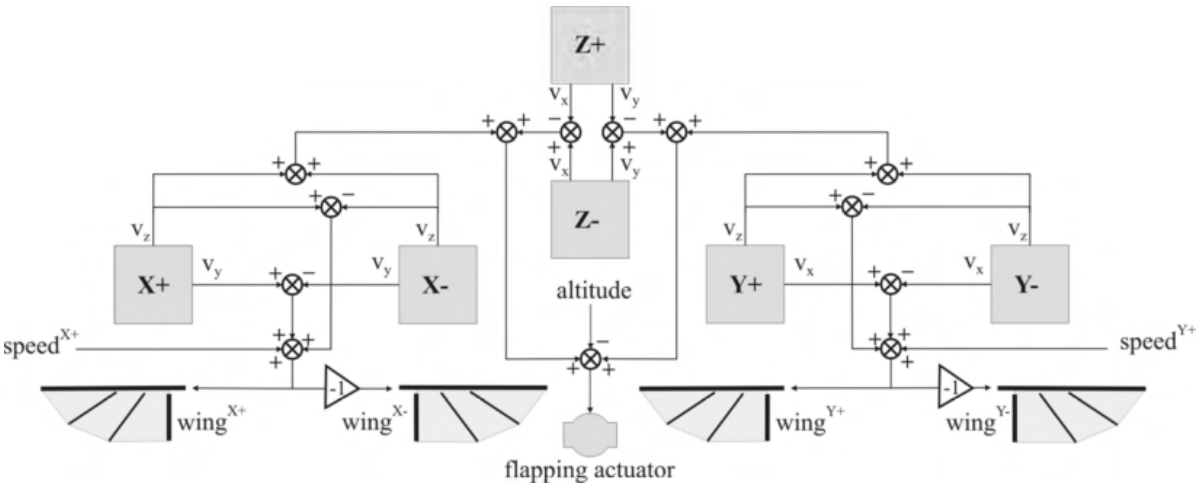

Figure 4.6: Schematic of the optical flow based stability and obstacle avoidance control system proposed by Goosen [34]

4.4.5. Summary

Table 4.1 summarizes the works, studied in this section, on the application of optical flow in MAV navigation. Several researchers have used the IMU measurements to de-rotate the optical flow components and then used the translational optical flow for their navigation strategy. While other researchers have used optical flow to complement the inertial sensors in ego-motion estimation.

Navigation Task	**Optical Flow + Inertial Sensors**	**Purely Optical Flow**	
	Free Flying	Tethered	Free Flying
Landing or Altitude Control	Chahl et al. [62] Herissé et al. [89] Ho et al. [25]	Ruffier & Franceschini [24][84] Franceschini et al. [88] Duhamel et al. [81]	Green et al. [23]
Obstacle Avoidance	Zufferey and Floreano [26] Beyeler et al. [33] Zingg et al. [93]		Iida [92] Green et al. [23]
Velocity Control	Moore et al. [95] Kimberly et al. [27] Briod et al. [28]		Serres et al.[94]
Attitude Stabilization	Omari and Ducard [31] [4] Verveld et al. [32][5] Beyeler et al. [33]	Zhang et al. [96]	

Table 4.1: Summary of optical flow based navigation strategies in MAVs

However, the available literature lacks studies on purely optical flow based methods. To the best knowledge of the author, implementation of purely optical flow based attitude estimation and stabilization strategy, in an inherently unstable MAV platform, has not been reported yet. This makes the the research objective formulated in Chapter 1 an extremely intriguing topic to pursue in this thesis.

[4] Framework only studied in simulations
[5] Framework studied in simulations and experimental investigation was done on a tethered pendulum like sensor setup

5

Flapping Wing Micro Aerial Vehicles

In chapter 2, the extraordinary aerial capabilities of the insects have been described. At present, over a million species of insects and over 13000 warm blooded vertebrate species are capable of flight [7], and all of them use wing flapping as their propulsion mechanism. Therefore, being inspired by these exceptional natural flyers, the fascination of humankind with flight was first focused on flapping wing flying machines. There have been numerous scientific and amateurish attempts of imitating the natural flyers [4, 5], however, most vehicles failed to take off, demonstrated significantly limited performance, or even conveyed their pilots to death [98]. The recent trend of miniaturization of unmanned aerial vehicles (UAVs) towards the micro aerial vehicle (MAV) category, thus requiring the development of small and light aerial vehicles capable of achieving flight in low Reynolds number flows, has inspired the researchers to consider flapping wings as the propulsion and flight control mechanism for these vehicles. In the last two decades, researchers have actively worked towards mimicking the insect flight through flapping wing micro aerial vehicles (FWMAVs). The FWMAVs are expected to fill the gap between fixed wing and rotary wing MAVs. Though the fixed wing platforms demonstrate good forward flight characteristics, they lack the ability to hover and to take-off and land vertically (VTOL). On the other hand, rotary wing platforms have hover and VTOL capability, however, they have lower efficiency and performance, especially in forward flight. FWMAVs bring together the best of both worlds by being able to hover, VTOL, perform complex and agile manoeuvres and demonstrate higher efficiency and performance at low Reynolds number flight conditions. This chapter provides an overview about the state of the art flapping wing aerial robots, followed by a detailed description of the robotic platform, the Delfly Nimble.

5.1. State of the Art

Several flight capable FWMAVs have been developed in the recent years. The FWMAVs can be categorized based on their wing configurations : (1) ones inspired from birds and most insects, having only one pair of wings (monoplane), (2) ones inspired from quad-winged insects, like the dragon fly, with the four wings being in tandem configuration, and (3) ones having the four wings in biplane or X-wing configuration. Further, FWMAVs are also categorized, based on the presence of tail, as tailed and tail-less FWMAVs. Figure 5.1 depicts a few important state of the art FWMAVs, grouped based on their wing configurations and the presence or absence of a tail.

The monoplane configuration of the wings is the most common wing configuration occurring in nature, like in birds, honeybees, fruitflies etc. This mechanism is also widely adopted for the development of FWMAVs [8, 9, 99, 100, 104–106]. It is the most simple and straightforward concept in terms of design and construction, however, the resulting wing motion often leads to considerable oscillations of the body, which are disadvantageous for on-board sensors.

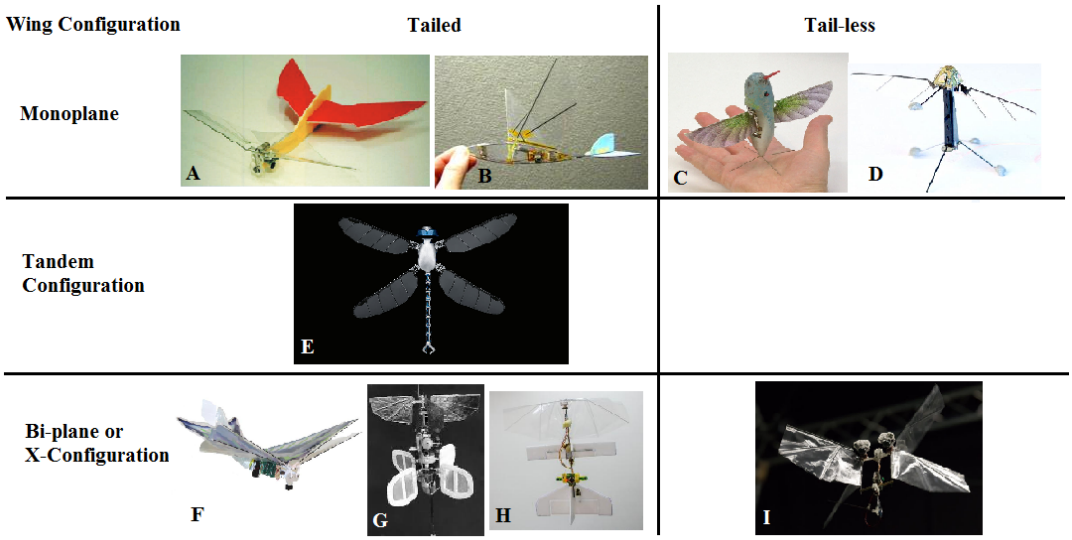

Figure 5.1: State of the art FWMAVs grouped based on their wing configurations and the presence or absence of tails. A) Tamkang University's Golden Snitch [99], B) Caltech's Micro Bat [100], C) AeroVironment's Nano Hummingbird [9], D) Harvard University's Robobee [8], E) Festo's BionicOpter [101](Source : https://www.festo.com/), F) Berkeley University's I-Bird [102], G) University of Toronto's Mentor [103], H) TU Delft's DelFly Explorer [79], I) TU Delft's DelFLy Nimble [11]

Some FWMAVs make use of two pairs of wings, arranged in tandem or biplane configuration. The tandem configuration of the wings is inspired by nature as it occurs in some insects like dragonflies. However, mimicking this configuration in robotic flyers is difficult and hence efforts in this direction are rare[101, 107]. A more widely used alternative of the tandem configuration, is having the wings in a biplane (or X-wing) configuration [10, 102, 103]. Opposite phase of flapping wings reduces the body oscillations, making the platform more suitable for carrying sensors onboard. Moreover, in bi-plane configuration, the wings exploit the mechanism of clap and fling to enhance lift generation [10].

Another important categorization of the FWMAVs is on the basis of tailed and tailless designs. The presence of a tail provides the platform with passive stability [10, 99, 102, 103]. Apart from stabilizing the platforms, the tails also have control surfaces mounted on them that provide the required control moments. Tailless designs, on the other hand, lack inherent stability but are more agile and manoeuvrable [8, 9, 11, 106]. Being tailless, they are also smaller and lighter than their tailed counterparts and hence more closely resemble insects. However, the lack of inherent stability makes an active control system necessary.

5.2. Delfly Nimble

Current work is being pursued as a part of the Delfly project[1] at Delft University of Technology. The project started in 2005, when a group of undergraduate students completed studies by making the first design of a DelFly, named Delfly I. The project since then has followed a top-down approach, which means that the research started with a fully functioning system, through which theoretical insights were gained and the research progressed by creating and studying progressively better systems, while always maintaining a fully functioning platform [10]. The first version of Delfly, named Delfly I (figure 5.2A), was developed with a bi-plane wing configuration and an inverted V tail. Following that study, different Delfly configurations have been created, with different design goals,

[1] http://www.delfly.nl

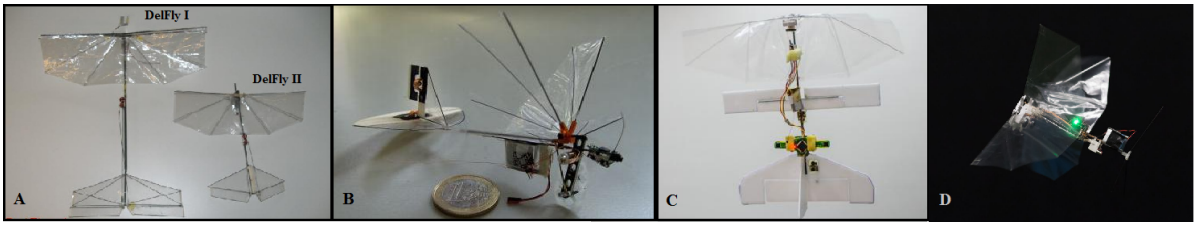

Figure 5.2: Various DelFly versions. A) DelFly I (left) and DelFly II (right) [10], B) DelFly Micro [10], C) DelFly Explorer [79], D) DelFly Nimble [11]

namely Delfly II (figure 5.2A), Delfly Micro[2] [10](figure 5.2B), Delfly Explorer [79](figure 5.2C) and DelFly Nimble (figure 5.2D).

In 2018, Karásek et al. [11] presented the first tailless version of Delfly, the Delfly Nimble (figure 5.3A). The robot weighs 28.2 grams and has a wing span of 33 cm, with its 14 cm long wings flapping at a frequency of 17 Hz during hover. As discussed in the previous section, Nimble, being tailless, is inherently unstable and hence it requires active attitude stabilization. To do this it carries a miniature 2.8 grams autopilot, Lisa/S [109], equipped with a 72MHz ARM Cortex-M3 microcomputer and an MPU6000 6 axis MEMS IMU (consisting of a 3 axis gyroscope and accelerometer) among other sensors. Attitude is estimated by fusing the accelerometer and gyroscope measurements using a complementary filter. In future studies, the optical flow based strategy being developed as a part of this thesis project will be implemented for ego-motion estimation and flight stabilization of the Nimble. Unlike tailed FWMAVs, Nimble does not have control surfaces to produce control moments and hence it adjusts its wing actuation system to stabilize and control its flight. The following section (Section 5.2.1) describes the mechanisms used by the Nimble to control its position and orientation during flight, which is followed by a description of its flight dynamics in section 5.2.2.

5.2.1. Flight Control Mechanisms

The Nimble can actuate its flapping mechanism to control four degrees of freedom (DoFs): thrust, pitch, roll and yaw. The helicopter model is employed to allow motion in 6-DoF space. The forward/backward flight is controlled by body pitch (figure 5.3C) and lateral flight is achieved by body roll (figure 5.3D). To control its orientation, the robot produces pitch, roll and yaw torques by adjusting its wing-beat pattern. The wing root servo facilitates yaw control by changing the wing root angle such that the flapping cycle averaged thrust vectors of the left and right wings are tilted in opposite directions (figures 5.3E and H). Pitch moment is generated by adjusting the dihedral angle, which shifts the flapping cycle averaged thrust vector relative to the CoG (figure 5.3F and I). To change the dihedral angle, a servo driven mechanism, between the two flapping mechanisms, is utilized. Unlike other members of the DelFly family, which have a single flapping mechanism, the Nimble has two separate flapping mechanisms, independently driving its left and right wing pairs. Individual thrust modulation of each flapping mechanism allows for roll control (figure: 5.3G and J). Finally, the thrust is modulated by symmetric actuation of the flapping mechanisms. The resulting control torques and thrust have high magnitude, high bandwidth, very little coupling and are minimally sensitive to the vertical location of the centre of mass (CoG) [11].

5.2.2. Flight Dynamics Model

As already discussed, an active feedback control system is crucial for the Nimble to maintain its stability. Now to design an efficient control system for the Nimble, a model of its flight dynamics

[2] In 2008 Delfly Micro was included in the Guinness book of records for being the smallest ornithopter carrying a camera [108].

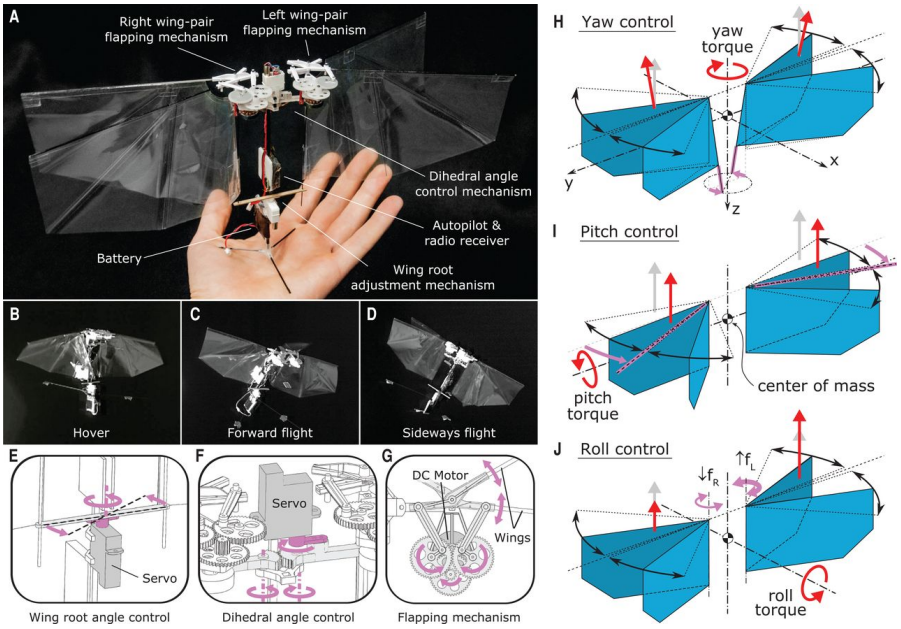

Figure 5.3: The DelFly Nimble. A) Nimble and its various components. (B-D): Hover (B), forward flight (C), and lateral flight (D). (E-G): Control mechanism design details, (E) the wing root deflection mechanism for controlling the yaw moment, (F) the dihedral deflection mechanism for controlling the pitch moment, and (G) the flapping mechanism, used for controlling the thrust and roll moment. (H-J): Wing actuation and aerodynamic forces and torques during yaw control (H), pitch control (I), and roll control (J). Magenta arrows represent actuation, gray arrows represent the nominal flapping cycle average aerodynamic thrust vectors, and red arrows represent flapping cycle average thrust and torques after control actuation. Source: [11]

is necessary. This section describes a minimal longitudinal dynamic model of the Delfly Nimble as presented by Kajak et al [110].

Considering the Nimble to be a rigid body with its movable parts mass less, the standard rigid body equations of motion are utilized. The longitudinal equations of motion of the Nimble, assuming perfect symmetry of the robot, no wind and flapping cycle averaged forces and moments, can be formulated as:

$$m\dot{u} = -\dot{\theta}w - mgsin\theta + X \tag{5.1}$$

$$m\dot{w} = \dot{\theta}u + mgcos\theta + Z \tag{5.2}$$

$$I_{yy}\ddot{\theta} = M \tag{5.3}$$

Where, m is mass of the robot, u and w denote its velocities in longitudinal and vertical directions (body reference frame), θ denotes its pitch angle, M is the pitch torque, I_{yy} is its moment of inertia about the body lateral axis and X and Z respectively denote the longitudinal and vertical body forces.

Figure 5.4 depicts the force body diagram of the robot. It is assumed that the wings are the source of all aerodynamic forces and the body drag is neglected. The wings generate a thrust force T and the body motion induces a drag D, both acting at the flapping cycle average centre of pressure (CoP). The dihedral angle of the robot is represented by the adjustable longitudinal position of the CoP with respect to the CoG. The drag force has the following components respectively in the body x and z direction :

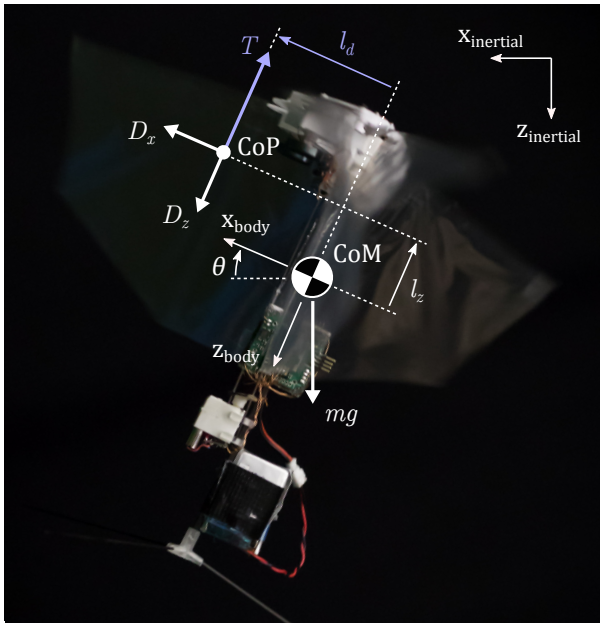

Figure 5.4: 2D longitudinal free body diagram of DelFly Nimble. CoP represents the mean centre of pressure, CoM represents the centre of mass. The control variables have been depicted in blue colour. Source: [110]

$$D_x = -b_x f u_{CoP} \tag{5.4}$$

$$D_z = -b_z f w_{CoP} \tag{5.5}$$

Here, f represents the flapping frequency, b_x and b_z represent the drag coefficients along x and z axes respectively. u_{CoP} and w_{CoP} respectively represent the longitudinal and vertical components of the velocity of the CoP (as it is adjustable). These velocities further can be formulated as :

$$u_{CoP} = u - l_z\dot{\theta} + \dot{l_d} \tag{5.6}$$

$$w_{CoP} = w - l_d\dot{\theta} \tag{5.7}$$

Where, l_d and l_z respectively represent the longitudinal and vertical positions of the CoP. It should be noted that among these, l_d is adjustable by adjusting the dihedral angle but l_z is fixed. Following the described free body diagram in figure 5.4, the body forces and moments can be written as :

$$X = D_x = -b_x f(u - l_z\dot{\theta} + \dot{l_d}) \tag{5.8}$$

$$Z = D_z - T = -b_z f(w - l_d\dot{\theta}) - T(f) \tag{5.9}$$

$$M = D_x l_z + (D_z - T)l_d = -b_x f l_z(u - l_z\dot{\theta} + \dot{l_d}) + b_z f l_d(w - l_d\dot{\theta}) - T(f)l_d \tag{5.10}$$

Here, thrust, T, is assumed to be a linear function of the flapping frequency f. Experimentally gathered data is linearly fit to estimate the thrust model.

$$T = 2(c_1 f + c_2) \tag{5.11}$$

where, c_1 and c_2 are the fitted coefficients [110].

Finally inserting equations 5.8-5.14 into equations 5.1-5.3, the complete set of longitudinal flight dynamic equations are derived :

$$m\dot{u} = -m\dot{\theta}w - mgsin\theta - b_x f(u - l_z\dot{\theta} + \dot{l_d}) \tag{5.12}$$

$$m\dot{w} = m\dot{\theta}u + mgcos\theta - T(f) - b_z f l_d(w - l_d\dot{\theta}) \tag{5.13}$$

$$I_{yy}\ddot{\theta} = -b_x f l_z(u - l_z\dot{\theta} + \dot{l_d}) + b_z f l_d(w - l_d\dot{\theta}) - T(f)l_d \tag{5.14}$$

Parameter	Value	Unit
m	29.4	g
I_{yy}	1.26×10^{-4}	kgm^2
b_x	4.21×10^{-3}	Ns^2m^{-1}
b_z	9.16×10^{-4}	Ns^2m^{-1}
l_z	27.1	mm
c_1	0.0114	$4NHz^{-1}$
c_2	-0.0449	N

Table 5.1: Optimized longitudinal model parameters for a DelFly Nimble

Note that the model has two adjustable inputs (CoP location l_d and the flapping frequency f) and only five parameters to be estimated (mass m, moment of inertia I_{yy}, vertical location of CoP l_z and drag coefficients b_x and b_z). Based on appropriate assumptions, the starting estimates of each of these parameters were obtained : The mass was measured by a precision scale. The moment of inertia was analytically estimated from locations and masses of its individual components. The drag coefficients were estimated by performing ordinary least squares regression on experimentally gathered data of steady level flight of the robot at various flight speeds in a wind tunnel. It was assumed that the CoP lies at quarter chord distance from the wing leading edge, and thus a starting estimate of l_z was obtained. Further open loop validation of the model with the above stated parameter values was performed after which the parameter values were optimized to obtain the best match between simulation and flight data. The obtained parameter values are listed in table 5.1.

The authors demonstrate that the model very well captures the effects of varying some properties, like the centre of mass position or controller parameters. Further, following a similar approach the lateral dynamics of the robot can also be derived.

This concludes the description of the FWMAV DelFly Nimble, which in future studies will be used as a platform to implement the attitude estimation approach being developed in this investigation.

6

Literature Consolidation

As a preliminary part of this thesis, an in depth literature study has been conducted which has been presented in Part **II** of this report. This section intends to conclude the literature study by summarizing its key findings.

Conventionally, IMUs, comprising of accelerometers, gyroscopes and sometimes magnetometers, are used for motion sensing and attitude estimation in MAVs. MEMS IMUs, owing to being small and light weight, are popular choices for MAV applications [13]. However, as the size of these IMUs reduce, their noise increases and sensitivity decreases. The noise and inherent drift lead to quickly diverging attitude estimates when angular rate measurements from the gyroscope are directly integrated [41]. Hence, sensor fusion algorithms like the Kalman filters [45–47] and complementary filters [48, 49] are used to increase the estimation accuracy. However, these algorithms increase the computational burden on the on-board processor, which is highly undesirable.

Many important inspirations can be drawn from the motion perception and navigation strategies used by the insects for effective stabilization and control of MAVs. Insects use rich sensory feedback for flight stabilization and control, drawing ego motion information from sensory organs like halteres, ocelli and the compound eyes. Visual sensing plays a prominent role in the insect's ego-motion inference. Most insects are equipped with a sophisticated imaging system known as the compound eyes [7]. The compound eyes, apart from enabling panoramic imagery, also encodes information about motion and direction in the form of optical flow fields [15, 56]. Optical flow sensing is critical to various insect flight behaviours like obstacle avoidance and navigation through small gaps [18], flight speed regulation [19, 20], altitude control [21], and performing smooth landings [22]. Though attitude estimation and stabilization in insects is yet to be completely understood, there is enough evidence to prove that optical flow sensing is critical to effective attitude stabilization in insects [29].

The concept of optical flow can be defined as a means to quantify the relative motion between the objects in a static scene and a moving observer [15]. In essence, optical flow measures the ratio of movement velocity to the distance of surrounding objects. Two commonly used mathematical formulations of optical flow have been described in the report: formulation using perspective projection method [17] and formulation using spherical projection method [16]. Further, two classes of widely used optical flow computation algorithms have been described in the report: gradient based methods [65, 71, 73] and correlation based methods [76–78].

Various optical flow sensors have been used in literature for optical flow based MAV navigation applications: like small conventional cameras[27, 79], dedicated optical flow sensors used in computer mice [86, 87] and Elementary Motion Detector (EMD) based sensors [83]. The bio-inspired

artificial compound eye CURVACE [85] can be considered to be one of the most promising optical flow sensors. Weighing just 1.75 grams, CURVACE is capable of streaming images with $180^o \times 60^o$ Field of View (FoV) at frame rates as high as 1950 Hz. However, applications of CURVACE in MAV navigation have not been extensively investigated yet.

Drawing inspirations from insects, researchers have investigated the applications of optical flow based navigation strategies for landing [23–25], obstacle avoidance [23, 26] and velocity control [27, 28] of MAVs. However, works in the field of optical flow based attitude estimation and stabilization remains obscure.

The literature study is concluded by reviewing state of the art in FWMAVs. Various recently developed tiny FWMAVs like the Robobee [8], Nano Hummingbird [9], and Delfly [10, 11] have been reviewed and their characteristics described. This is followed by a detailed description of flight control mechanisms and dynamics model of the DelFly Nimble[11] which, in future studies, will be used as a MAV platform for the application of the attitude estimation approach being developed in this study.

The lack of understanding of the strategies used by insects for estimating and stabilizing their attitude and the deficiency of literature concerning optical flow based attitude estimation methods for MAVs, motivated the objective of the current study: “Feasibility investigation and development of an optical flow based approach for attitude estimation of a flying robot".

Thesis Conclusions

Based on a comprehensive literature survey, on the topic of optical flow based attitude estimation and stabilization of Micro Aerial Vehicles (MAVs), it was found that the techniques used by insects for estimating their absolute attitude and stabilizing their flight are still not completely understood. However, there are evidences which indicate that insects prominently make use of optical flow fields for ego-motion estimation. The feasibility of estimating absolute values of attitude from optical flow fields would mean that a camera can be effectively used to complement or even replace the inertial measurement units (IMUs) for flight stabilization of MAVs. Thus, to test this hypothesis the objective of this thesis was decided as: “Feasibility investigation and development of an optical flow based approach for attitude estimation of a flying robot".

In this thesis, through non linear observability analysis it has been proven that it is indeed possible to estimate the attitude of a MAV using optical flow measurements and the knowledge of control efference copies. Based on the findings of the observability analysis, an extended Kalman filter (EKF) state estimator has been designed and its performance has been verified in simulations and on flight data obtained from a real flying robot. The estimator only uses ventral flow and divergence measurements obtained from a downward looking monocular camera, along with the knowledge of control inputs to estimate: pitch angle, pitch rate, horizontal and vertical components of velocity and height, of a MAV constrained to move with 3 degrees of freedom. In simulations, the state estimates obtained from the estimator have been used in a closed loop to control the attitude and altitude of a MAV, thus establishing the feasibility of using the approach in attitude stabilization of an inherently unstable MAV.

To the best of the author’s knowledge, the approach introduced in this study is the first attitude estimation algorithm that utilizes optical flow as the only sensory information. Thus, through the investigations performed and results obtained during the course of this thesis project, the set research objective has been met and the research questions have been satisfactorily answered.

In future investigations, a more effective approach of modelling the moment efference inputs based on the MAV’s rotor velocities will be devised and incorporated. Further, the estimator will be implemented on-board a tailless flapping wing MAV: DelFly Nimble, and attitude stabilization of the platform will be performed.

The findings of this thesis propose a very attractive solution for miniaturization of MAVs. Further, the findings also form a novel hypothesis about how some flying insects can estimate their states, including attitude, utilizing optical flow as the prominent sensory information. Thus the work performed in this thesis brings us a small step closer to making MAVs as nimble as the insects.

Bibliography

[1] Mestral George De. Separable fastening device, November 21 1961. US Patent 3,009,235.

[2] Laurent Wahl, Stefan Maas, Danièle Waldmann, Arno Zürbes, and Patrick Frères. Shear stresses in honeycomb sandwich plates: Analytical solution, finite element method and experimental verification. *Journal of Sandwich Structures & Materials*, 14(4):449–468, 2012.

[3] Josh Bongard. Biologically inspired computing. *IEEE computer*, 42(4):95–98, 2009.

[4] da L. Vinci. Manuscript b. 1488-1490.

[5] Alexander M Lippisch. Man powered flight in 1929. *The Aeronautical Journal*, 64(595):395–398, 1960.

[6] Carroll F Gray. " the first five flights, the slope and winds of big kill devil hill–the first flight reconsidered. *WW1 AERO-The Journal of the Early Aeroplane (177)*, pages 26–39, 2002.

[7] Wei Shyy, Chang-kwon Kang, Pakpong Chirarattananon, Sridhar Ravi, and Hao Liu. Aerodynamics, sensing and control of insect-scale flapping-wing flight. *Proceedings of the Royal Society A: Mathematical, Physical and Engineering Sciences*, 472(2186):20150712, 2016.

[8] Kevin Y Ma, Pakpong Chirarattananon, Sawyer B Fuller, and Robert J Wood. Controlled flight of a biologically inspired, insect-scale robot. *Science*, 340(6132):603–607, 2013.

[9] Matthew Keennon, Karl Klingebiel, and Henry Won. Development of the nano hummingbird: A tailless flapping wing micro air vehicle. In *50th AIAA aerospace sciences meeting including the new horizons forum and aerospace exposition*, page 588, 2012.

[10] GCHE De Croon, KME De Clercq, Remes Ruijsink, Bart Remes, and Christophe De Wagter. Design, aerodynamics, and vision-based control of the DelFly. *International Journal of Micro Air Vehicles*, 1(2):71–97, 2009.

[11] Matěj Karásek, Florian T Muijres, Christophe De Wagter, Bart DW Remes, and Guido CHE de Croon. A tailless aerial robotic flapper reveals that flies use torque coupling in rapid banked turns. *Science*, 361(6407):1089–1094, 2018.

[12] JL Verboom, Sjoerd Tijmons, C De Wagter, B Remes, Robert Babuska, and Guido CHE de Croon. Attitude and altitude estimation and control on board a flapping wing micro air vehicle. In *Robotics and Automation (ICRA), 2015 IEEE International Conference on*, pages 5846–5851. IEEE, 2015.

[13] Neil M Barbour. Inertial navigation sensors. Technical report, Charles Stark Draper Lab Inc Cambridge Ma, 2010.

[14] Graham K Taylor and Holger G Krapp. Sensory systems and flight stability: what do insects measure and why? *Advances in insect physiology*, 34:231–316, 2007.

[15] James J Gibson. The perception of the visual world. 1950.

[16] Jan J Koenderink and Andrea J van Doorn. Facts on optic flow. *Biological cybernetics*, 56(4): 247–254, 1987.

[17] Hugh Christopher Longuet-Higgins, Kvetoslav Prazdny, et al. The interpretation of a moving retinal image. *Proc. R. Soc. Lond. B*, 208(1173):385–397, 1980.

[18] WH Kirchner and MV Srinivasan. Freely flying honeybees use image motion to estimate object distance. *Naturwissenschaften*, 76(6):281–282, 1989.

[19] Charles T David. Compensation for height in the control of groundspeed bydrosophila in a new,'barber's pole'wind tunnel. *Journal of Comparative Physiology A: Neuroethology, Sensory, Neural, and Behavioral Physiology*, 147(4):485–493, 1982.

[20] Geoffrey Portelli, Franck Ruffier, Frédéric L Roubieu, and Nicolas Franceschini. Honeybees' speed depends on dorsal as well as lateral, ventral and frontal optic flows. *PloS one*, 6(5): e19486, 2011.

[21] Geoffrey Portelli, Julien R Serres, and Franck Ruffier. Altitude control in honeybees: joint vision-based learning and guidance. *Scientific reports*, 7(1):9231, 2017.

[22] Mandyam V Srinivasan. Honeybees as a model for the study of visually guided flight, navigation, and biologically inspired robotics. *Physiological reviews*, 91(2):413–460, 2011.

[23] William E Green, Paul Y Oh, and Geoffrey Barrows. Flying insect inspired vision for autonomous aerial robot maneuvers in near-earth environments. In *IEEE International Conference on Robotics and Automation, 2004. Proceedings. ICRA'04. 2004*, volume 3, pages 2347–2352. IEEE, 2004.

[24] Franck Ruffier and Nicolas Franceschini. Optic flow regulation: the key to aircraft automatic guidance. *Robotics and Autonomous Systems*, 50(4):177–194, 2005.

[25] HW Ho, GCHE de Croon, E Van Kampen, QP Chu, and Max Mulder. Adaptive control strategy for constant optical flow divergence landing. *arXiv preprint arXiv:1609.06767*, 2016.

[26] J-C Zufferey and Dario Floreano. Fly-inspired visual steering of an ultralight indoor aircraft. *IEEE Transactions on Robotics*, 22(1):137–146, 2006.

[27] Kimberly McGuire, Guido de Croon, Christophe De Wagter, Karl Tuyls, and Hilbert J Kappen. Efficient optical flow and stereo vision for velocity estimation and obstacle avoidance on an autonomous pocket drone. *IEEE Robotics and Automation Letters*, 2(2):1070–1076, 2017.

[28] Adrien Briod, Jean-Christophe Zufferey, and Dario Floreano. Optic-flow based control of a 46g quadrotor. In *Workshop on Vision-based Closed-Loop Control and Navigation of Micro Helicopters in GPS-denied Environments, IROS*, volume 13, 2013.

[29] Roman Goulard, Jean-Louis Vercher, and Stéphane Viollet. To crash or not to crash: how do hoverflies cope with free-fall situations and weightlessness? *Journal of Experimental Biology*, 219(16):2497–2503, 2016.

[30] Michael H Dickinson. Haltere–mediated equilibrium reflexes of the fruit fly, drosophila melanogaster. *Philosophical Transactions of the Royal Society of London B: Biological Sciences*, 354(1385):903–916, 1999.

[31] Sammy Omari and Guillaume Ducard. Metric visual-inertial navigation system using single optical flow feature. In *2013 European Control Conference (ECC)*, pages 1310–1316. IEEE, 2013.

[32] Mark Verveld, Qi-Ping Chu, Christophe De Wagter, and JA Mulder. Optic flow based state estimation for an indoor micro air vehicle. In *AIAA Guidance, Navigation, and Control Conference*, page 8209, 2010.

[33] Antoine Beyeler, Jean-Christophe Zufferey, and Dario Floreano. Vision-based control of near-obstacle flight. *Autonomous robots*, 27(3):201, 2009.

[34] JFL Goosen. Design aspects of a bio-inspired flying sensor node. In *SENSORS, 2012 IEEE*, pages 1–4. IEEE, 2012.

[35] Floris Van Breugel, Kristi Morgansen, and Michael H Dickinson. Monocular distance estimation from optic flow during active landing maneuvers. *Bioinspiration & biomimetics*, 9(2): 025002, 2014.

[36] Roman Goulard, Jean-Louis Vercher, and Stéphane Viollet. Modeling visual-based pitch, lift and speed control strategies in hoverflies. *PLoS computational biology*, 14(1):e1005894, 2018.

[37] Guido CHE de Croon. Monocular distance estimation with optical flow maneuvers and efference copies: a stability-based strategy. *Bioinspiration & biomimetics*, 11(1):016004, 2016.

[38] Hann Woei Ho, Guido CHE de Croon, and Qiping Chu. Distance and velocity estimation using optical flow from a monocular camera. *International Journal of Micro Air Vehicles*, 9(3):198–208, 2017.

[39] Daan van Vrede. Flight control and collision avoidance for quadcopter and flapping wing MAVs using only optical flow: Theory, simulation and experiment. 2018.

[40] Clark Borst. Inertial navigation. Lecture Notes, Avionics and Operations (AE4302), Faculty of Aerospace Engineering, TU Delft, November 2017.

[41] Manon Kok, Jeroen D Hol, and Thomas B Schön. Using inertial sensors for position and orientation estimation. *arXiv preprint arXiv:1704.06053*, 2017.

[42] Clark Borst. Gyroscopes. Lecture Notes, Avionics and Operations (AE4302), Faculty of Aerospace Engineering, TU Delft, November 2017.

[43] Rudolph Emil Kalman. A new approach to linear filtering and prediction problems. *Transactions of the ASME–Journal of Basic Engineering*, 82(Series D):35–45, 1960.

[44] Greg Welch, Gary Bishop, et al. An introduction to the Kalman filter. 1995.

[45] Stanley F Schmidt. The Kalman filter-its recognition and development for aerospace applications. *Journal of Guidance, Control, and Dynamics*, 4(1):4–7, 1981.

[46] Martin A Skoglund, Gustaf Hendeby, and Daniel Axehill. Extended Kalman filter modifications based on an optimization view point. In *2015 18th International Conference on Information Fusion (Fusion)*, pages 1856–1861. IEEE, 2015.

[47] Simon J Julier and Jeffrey K Uhlmann. New extension of the Kalman filter to nonlinear systems. In *Signal processing, sensor fusion, and target recognition VI*, volume 3068, pages 182–194. International Society for Optics and Photonics, 1997.

[48] A-J Baerveldt and Robert Klang. A low-cost and low-weight attitude estimation system for an autonomous helicopter. In *Proceedings of IEEE International Conference on Intelligent Engineering Systems*, pages 391–395. IEEE, 1997.

[49] Robert Mahony, Tarek Hamel, and J-M Pflimlin. Complementary filter design on the special orthogonal group so (3). In *Proceedings of the 44th IEEE Conference on Decision and Control*, pages 1477–1484. IEEE, 2005.

[50] Tariqul Islam, Md Saiful Islam, Md Shajid-Ul-Mahmud, and Md Hossam-E-Haider. Comparison of complementary and Kalman filter based data fusion for attitude heading reference system. In *AIP Conference Proceedings*, volume 1919, page 020002. AIP Publishing, 2017.

[51] M Gewecke. The antennae of insects as air-current sense organs and their relationship to the control of flight. In *Experimental analysis of insect behaviour*, pages 100–113. Springer, 1974.

[52] Stefan Schütz, Bernhard Weissbecker, Hans E Hummel, Karl-Heinz Apel, Helmut Schmitz, and Horst Bleckmann. Insect antenna as a smoke detector. *Nature*, 398(6725):298, 1999.

[53] Sanjay P Sane, Alexandre Dieudonné, Mark A Willis, and Thomas L Daniel. Antennal mechanosensors mediate flight control in moths. *science*, 315(5813):863–866, 2007.

[54] John A Bender and Mark A Frye. Invertebrate solutions for sensing gravity. *Current Biology*, 19(5):R186–R190, 2009.

[55] Holger G Krapp. Ocelli. *Current Biology*, 19(11):R435–R437, 2009.

[56] V Hassenstein and W Reichardt. System theoretical analysis of time, sequence and sign analysis of the motion perception of the snout-beetle chlorophanus. *Z Naturforsch B*, 11:513–524, 1956.

[57] Holger G Krapp, Barbel Hengstenberg, and Roland Hengstenberg. Dendritic structure and receptive-field organization of optic flow processing interneurons in the fly. *Journal of Neurophysiology*, 79(4):1902–1917, 1998.

[58] Anna Honkanen. *Insect optomotor experiments in the dark using virtual reality*. PhD thesis, 12 2014.

[59] Werner Reichardt. Movement perception in insects. *Processing of optical data by organisms and by machines*, pages 465–493, 1969.

[60] M Srinivasan, Shaowu Zhang, M Lehrer, and T Collett. Honeybee navigation en route to the goal: visual flight control and odometry. *Journal of Experimental Biology*, 199(1):237–244, 1996.

[61] Mandyam V Srinivasan, Shao-Wu Zhang, Javaan S Chahl, Erhardt Barth, and Svetha Venkatesh. How honeybees make grazing landings on flat surfaces. *Biological cybernetics*, 83(3):171–183, 2000.

[62] Javaan S Chahl, Mandyam V Srinivasan, and Shao-Wu Zhang. Landing strategies in honeybees and applications to uninhabited airborne vehicles. *The International Journal of Robotics Research*, 23(2):101–110, 2004.

[63] Emily Baird, Norbert Boeddeker, Michael R Ibbotson, and Mandyam V Srinivasan. A universal strategy for visually guided landing. *Proceedings of the National Academy of Sciences*, 110(46): 18686–18691, 2013.

[64] Rico Möckel. *Bio-inspired optical flow vision sensors for visual guidance of autonomous robots*. PhD thesis, ETH Zurich, 2012.

[65] Berthold KP Horn and Brian G Schunck. Determining optical flow. *Artificial intelligence*, 17 (1-3):185–203, 1981.

[66] Shimon Ullman. *The interpretation of visual motion.* Massachusetts Inst of Technology Pr, 1979.

[67] Steven S. Beauchemin and John L. Barron. The computation of optical flow. *ACM computing surveys (CSUR)*, 27(3):433–466, 1995.

[68] Chris Harris and Mike Stephens. A combined corner and edge detector. In *Alvey vision conference*, volume 15, pages 10–5244. Citeseer, 1988.

[69] Edward Rosten, Reid Porter, and Tom Drummond. Faster and better: A machine learning approach to corner detection. *IEEE transactions on pattern analysis and machine intelligence*, 32(1):105–119, 2010.

[70] Sean Borman and Robert Stevenson. Image sequence processing. *Department, Ed. Marcel Dekker, New York*, pages 840–879, 2003.

[71] Bruce D Lucas, Takeo Kanade, et al. An iterative image registration technique with an application to stereo vision. 1981.

[72] Ee Ping Ong and Michael Spann. Robust optical flow computation based on least-median-of-squares regression. *International Journal of Computer Vision*, 31(1):51–82, 1999.

[73] Eero P Simoncelli, Edward H Adelson, and David J Heeger. Probability distributions of optical flow. In *Computer Vision and Pattern Recognition, 1991. Proceedings CVPR'91., IEEE Computer Society Conference on*, pages 310–315. IEEE, 1991.

[74] Hans-Hellmut Nagel. Extending the 'oriented smoothness constraint'into the temporal domain and the estimation of derivatives of optical flow. In *European Conference on Computer Vision*, pages 139–148. Springer, 1990.

[75] David Fleet and Yair Weiss. Optical flow estimation. In *Handbook of mathematical models in computer vision*, pages 237–257. Springer, 2006.

[76] MA Sutton, WJ Wolters, WH Peters, WF Ranson, and SR McNeill. Determination of displacements using an improved digital correlation method. *Image and vision computing*, 1(3):133–139, 1983.

[77] Padmanabhan Anandan. A computational framework and an algorithm for the measurement of visual motion. *International Journal of Computer Vision*, 2(3):283–310, 1989.

[78] Ted Camus. Real-time quantized optical flow. *Real-Time Imaging*, 3(2):71–86, 1997.

[79] Christophe De Wagter, Sjoerd Tijmons, Bart DW Remes, and Guido CHE de Croon. Autonomous flight of a 20-gram flapping wing MAV with a 4-gram onboard stereo vision system. In *Robotics and Automation (ICRA), 2014 IEEE International Conference on*, pages 4982–4987. IEEE, 2014.

[80] Kimberly McGuire, Guido de Croon, Christophe De Wagter, Bart Remes, Karl Tuyls, and Hilbert Kappen. Local histogram matching for efficient optical flow computation applied to velocity estimation on pocket drones. In *Robotics and Automation (ICRA), 2016 IEEE International Conference on*, pages 3255–3260. IEEE, 2016.

[81] Pierre-Emile J Duhamel, Néstor O Pérez-Arancibia, Geoffrey L Barrows, and Robert J Wood. Altitude feedback control of a flapping-wing microrobot using an on-board biologically inspired optical flow sensor. In *Robotics and Automation (ICRA), 2012 IEEE International Conference on*, pages 4228–4235. IEEE, 2012.

[82] Patrick Lichtsteiner, Christoph Posch, and Tobi Delbruck. A 128×128 $120db$ $15\mu s$ latency asynchronous temporal contrast vision sensor. *IEEE journal of solid-state circuits*, 43(2):566–576, 2008.

[83] N Franceschini, C Blanes, and L Oufar. Passive, non-contact optical velocity sensor. *Dossier technique ANVAR/DVAR*, 51549, 1986.

[84] Franck Ruffier and Nicolas Franceschini. Optic flow regulation in unsteady environments: A tethered MAV achieves terrain following and targeted landing over a moving platform. *Journal of Intelligent & Robotic Systems*, 79(2):275–293, 2015.

[85] Stéphane Viollet, Stéphanie Godiot, Robert Leitel, Wolfgang Buss, Patrick Breugnon, Mohsine Menouni, Raphaël Juston, Fabien Expert, Fabien Colonnier, Géraud L'Eplattenier, et al. Hardware architecture and cutting-edge assembly process of a tiny curved compound eye. *Sensors*, 14(11):21702–21721, 2014.

[86] Stephen Griffiths, Jeff Saunders, Andrew Curtis, Blake Barber, Tim Mclain, and Randy Beard. Maximizing miniature aerial vehicles. *IEEE Robotics & Automation Magazine*, 13(3):34–43, 2006.

[87] Nils Gageik, Michael Strohmeier, and Sergio Montenegro. An autonomous UAV with an optical flow sensor for positioning and navigation. *International Journal of Advanced Robotic Systems*, 10(10):341, 2013.

[88] Nicolas Franceschini, Franck Ruffier, and Julien Serres. A bio-inspired flying robot sheds light on insect piloting abilities. *Current Biology*, 17(4):329–335, 2007.

[89] Bruno Herissé, Tarek Hamel, Robert Mahony, and François-Xavier Russotto. Landing a VTOL unmanned aerial vehicle on a moving platform using optical flow. *IEEE Transactions on robotics*, 28(1):77–89, 2012.

[90] Hann Woei Ho and Guido C de Croon. Characterization of flow field divergence for mavs vertical control landing. In *AIAA Guidance, Navigation, and Control Conference*, page 0106, 2016.

[91] Lance F Tammero and Michael H Dickinson. The influence of visual landscape on the free flight behavior of the fruit fly drosophila melanogaster. *Journal of Experimental Biology*, 205 (3):327–343, 2002.

[92] Fumiya Iida. Goal-directed navigation of an autonomous flying robot using biologically inspired cheap vision. In *Proceedings of the 32nd ISR (International Symposium on Robotics)*, volume 19, pages 21–27, 2001.

[93] Simon Zingg, Davide Scaramuzza, Stephan Weiss, and Roland Siegwart. MAV navigation through indoor corridors using optical flow. In *2010 IEEE International Conference on Robotics and Automation*, pages 3361–3368. IEEE, 2010.

[94] Julien Serres, D Dray, Franck Ruffier, and N Franceschini. A vision-based autopilot for a miniature air vehicle: joint speed control and lateral obstacle avoidance. *Autonomous robots*, 25 (1-2):103–122, 2008.

[95] Richard JD Moore, Karthik Dantu, Geoffrey L Barrows, and Radhika Nagpal. Autonomous MAV guidance with a lightweight omnidirectional vision sensor. In *2014 IEEE International Conference on Robotics and Automation (ICRA)*, pages 3856–3861. IEEE, 2014.

[96] Lianhua Zhang, Zongying Shi, and Yisheng Zhong. Attitude estimation of 3-DOF lab helicopter based on optical flow. In *Proceedings of the 33rd Chinese Control Conference*, pages 8536–8541. IEEE, 2014.

[97] Abhimanyu Selvan. Simulation of optic flow based flight control for a flapping wing micro aerial vehicle. 2014.

[98] Albino Lapa. *Aviação portuguesa*. 1928.

[99] Fu-Yuen Hsiao, TM Yang, and WC Lu. Dynamics of flapping-wing mavs: application to the tamkang golden snitch. 15(3):227–238, 2012.

[100] T Nick Pornsin-Sirirak, Yu-Chong Tai, Chih-Ming Ho, and Matt Keennon. Microbat: A palm-sized electrically powered ornithopter. In *Proceedings of NASA/JPL Workshop on Biomorphic Robotics*, pages 14–17, 2001.

[101] Nina Gaissert, Rainer Mugrauer, Günter Mugrauer, Agalya Jebens, Kristof Jebens, and Elias Maria Knubben. Inventing a micro aerial vehicle inspired by the mechanics of dragonfly flight. In *Conference Towards Autonomous Robotic Systems*, pages 90–100. Springer, 2013.

[102] Stanley S Baek and Ronald S Fearing. Flight forces and altitude regulation of 12 gram i-bird. In *Biomedical Robotics and Biomechatronics (BioRob), 2010 3rd IEEE RAS and EMBS International Conference on*, pages 454–460. IEEE, 2010.

[103] Patrick Zdunich, Derek Bilyk, Marc MacMaster, David Loewen, James DeLaurier, Roy Kornbluh, Tom Low, Scott Stanford, and Dennis Holeman. Development and testing of the mentor flapping-wing micro air vehicle. *Journal of Aircraft*, 44(5):1701–1711, 2007.

[104] Lindsey Hines, Domenico Campolo, and Metin Sitti. Liftoff of a motor-driven, flapping-wing microaerial vehicle capable of resonance. *IEEE Transactions on Robotics*, 30(1):220–232, 2014.

[105] Ryan Randall, Rajeev Kumar, and Sergey Shkarayev. Bio-inspired design of micro ornithopters with emphasis on locust hindwings. In *International Micro Air Vehicle Conference and Flight Competition (IMAV 2012)*, 2012.

[106] A Roshanbin, H Altartouri, M Karásek, and André Preumont. Colibri: A hovering flapping twin-wing robot. *International Journal of Micro Air Vehicles*, 9(4):270–282, 2017.

[107] Jia Ming Kok and Javaan Chahl. Design and manufacture of a self-learning flapping wing-actuation system for a dragonfly-inspired MAV. In *54th aiaa aerospace sciences meeting*, page 1744, 2016.

[108] Guinness Book of Records. Smallest camera plane. `http://www.guinnessworldrecords.com/world-records/smallest-camera-plane`, 2008. Accessed: 2019-02-3.

[109] BDW Remes, P Esden-Tempski, F Van Tienen, E Smeur, C De Wagter, and GCHE De Croon. Lisa-S 2.8 g autopilot for GPS-based flight of MAVs. In *International Micro Air Vehicle conference and competitions (IMAV 2014)*, 2014.

[110] K.M. Kajak, Matěj Karásek, Q.P. Chu, and Guido CHE de Croon. A minimal longitudinal dynamic model of a tailless flapping wing robot for control design. In *50th AIAA aerospace sciences meeting including the new horizons forum and aerospace exposition*, page 588, 2012.

Look at the sky. We are not alone. The whole universe is friendly to us, and conspires only to give the best to those who dream and work.

Dr. A.P.J. Abdul Kalam